Title
Topology and electronic properties of low-dimensional carbon materials

Author
Jiang, Jingwei

Publication Date
2023

Peer reviewed|Thesis/dissertation

Topology and electronic properties of low-dimensional carbon materials

by

Jingwei Jiang

A dissertation submitted in partial satisfaction of the

requirements for the degree of

Doctor of Philosophy

in

Physics

in the

Graduate Division

of the

University of California, Berkeley

Committee in charge:

Professor Steven G. Louie, Chair
Professor Michael F. Crommie
Professor Felix R. Fischer

Spring 2023

Topology and electronic properties of low-dimensional carbon materials

Abstract

Topology and electronic properties of low-dimensional carbon materials

by

Jingwei Jiang

Doctor of Philosophy in Physics

University of California, Berkeley

Professor Steven G. Louie, Chair

In recent times, there has been a significant interest in low-dimensional materials due to their unique electronic, optical, magnetic, and topological properties that differ from 3D bulk materials. This dissertation focuses on a specific class of 1D carbon structures known as graphene nanoribbons (GNRs), which can be synthesized atomically with precision through a bottom-up method. The theoretical tools employed in this study are primarily topological theory and quantum many-body first-principles calculations.

Chapter 1 introduces some basics about density functional theory, GW many-body perturbation theory and the Belthe-Salpeter equation. Chapter 2 of this dissertation delves into the topology of GNRs when chiral symmetry is approximately maintained. Building on this theory and in collaboration with experimentalists, Chapter 3 explores a metallic 1D nanowire known as saw-tooth GNRs, while Chapter 4 investigates various quantum dot systems with unique bonding and anti-bonding characters. In Chapter 5, a different type of metallic GNRs is studied using zero-mode (topologically protected in-gap electronic states) engineering. Chapter 6 takes the study beyond the Hermitian Hamiltonian and introduces the non-Hermitian skin effect. When 1D or 0D structures are interconnected, nanoporous graphene is formed. Its electronic properties are studied in Chapter 8. Furthermore, Chapter 9 examines a carbon kagome lattice's excitonic properties. The content of each Chapter is elaborated as the following:

- Chapter 1 provides a foundational understanding of density functional theory (DFT) for ground state properties by introducing the Kohn-Sham equation and different functionals. We also discuss the GW perturbation theory, which allows us to incorporate many-body effects into our calculations of excited-state properties. Specifically, we explore how the GW method can be utilized to calculate quasi-particle excitations. To study the two-particle excitation problem for optical properties, we introduce the Bethe-Salpeter equation (BSE) method. This equation provides a framework for calculating the interaction between an excited electron and the hole it leaves behind, which is crucial for understanding optical properties such as absorption and emission spectra.

- In Chapter 2, we examine GNR structures under the first nearest neighbor tight-binding model, assuming chiral symmetry holds. In this scenario, we utilize the first Chern number to obtain a Z index for general 1D materials. From the general Z index formula, we derive the Chiral phase index in vector form, which enables us to obtain the analytic Z index formula for all types of unit cells in GNRs. Finally, we explore a spin-chain formed by topological junction states that exhibit strong spin-spin interactions.[1]

- Chapter 3 builds on the chiral classification theory introduced in Chapter 2 by utilizing the topological junction states as building blocks and connecting them in a symmetric manner to form a 1D metallic nanowire. We use first-principles DFT calculations to study the electronic bandstructure, local density of states (LDOS), and mapping of wavefunctions. Our results are then compared with experimental STM measurements, and we achieve good agreement. In addition, we also investigate the topological properties of asymmetrically connected structures, and the predicted junction/end state matches well the corresponding experimental evidence.[2]

- In Chapter 4, we employed the topological junction states that arise from the connection between 7-armchair graphene nanoribbons (7AGNR) and 9-armchair graphene nanoribbons (9AGNR) to construct topological quantum dots. We investigated two distinct types of quantum dots by means of DFT calculations, with the aim of studying their electronic properties, such as the bonding and anti-bonding traits of their valence and conduction states. In addition, we devised a tight-binding theory to elucidate the underlying factors contributing to the characteristics of the wavefunctions.[3]

- In Chapter 5, we focus on a different variety of metallic graphene nanoribbon (GNR) called Olympicene GNRs that does not exhibit the Stoner instability, which was observed in the sawtooth GNRs presented in Chapter 3. This new GNR features cove-shaped edges, and its low-energy behavior is governed by zero modes. The most notable distinction between this GNR and the sawtooth GNR is that the nearest zero modes localize on different sublattices, leading to a significant increase in electron hopping and precluding any magnetic instability. To verify this, we conduct DFT calculations and compare our findings with experimental observations.

- In Chapter 6, we explore the topology of 1D non-Hermitian systems, extending our analysis beyond Hermitian topological classification. Specifically, we investigate a 1D non-Hermitian system with no symmetry constraints, and use a Z index that can be employed to classify such systems. We examine the well-known skin effect for non-trivial non-Hermitian topological models and identify a promising GNR material, Co-4AGNR, which could potentially be realized in experiments. By conducting first-principles DFT and full-frequency GW calculations, we establish that the material exhibits non-trivial topology. Lastly, we present evidence of the asymmetric transport properties in this material by calculating the Green's function for a finite segment of this system.

- In Chapter 7, we examine the 2D carbon structure that results from linking 1D metallic GNRs. To accomplish this, we created a theoretical model with low energy states

using modes that are found in the pentagons located at the edge of GNRs as the bases. This effective tight-binding model provides a description of a unique, distorted super-graphene. We also conducted DFT calculations and compared our findings with experimental results provided by our colleagues.[4]

- Chapter 8 focuses on the examination of a kagome lattice that is formed by linking triangulene building blocks. This unique structure was predicted to exhibit excitonic insulator (EI) behavior. In partnership with experimentalists, we conducted an investigation of the electronic properties of this structure using multiple levels of theory, such as DFT, GW-BSE, and Bardeen-Cooper-Schrieffer (BCS) theory. Our research revealed that DFT based single-particle theory was insufficient for accurately capturing the features of the LDOS map observed in STM measurements. By incorporating a BCS-like theory for condensation of excitons, we were able to provide an explanation for the experimental observations.[5]

In addition to the projects above, I was also involved in 3 other projects, including one studying the color center in twisted BN [6], one studying the kondo effect in magnetic N-doped chevronGNR [7], one studying the pseodo-atomic orbitals in graphene nanoribbons [8]. These research projects are also very interesting, but beyond the scope of this dissertation.

To my parents

Contents

List of Figures

Acknowledgments

First and foremost, I would like to express my deep gratitude to my Ph.D. advisor, Professor Steven G. Louie. I consider myself extremely fortunate, grateful, and honored to have completed my doctoral studies under your expert guidance. Your exceptional insights and erudite knowledge of condensed matter physics made my Ph.D. journey an unforgettable and joyous experience. Collaborating with you, brainstorming ideas, and working tirelessly to find solutions around the corner of your office table has been both inspiring and invigorating. Your rigorous, critical, and collaborative approach to research has had an immeasurable impact on me, and I have learned invaluable lessons from you that have helped me think critically and creatively. Moreover, I am deeply grateful for the unparalleled freedom you have given me to learn and conduct research. Your unwavering patience, support, and care for me have been invaluable, and I consider them a fortune. I would like to extend my gratitude to Mrs. Jane Louie for her kindness in preparing the annual Thanksgiving feast, spring festival feast and for her warm care and support for me. We feel truly blessed to have you both in my lives.

I would like to express my sincere thanks to the members of the Louie group, who have played an important role in my Ph.D. journey. Firstly I would like to thank Felipe and Diana, senior students in the group. You both have been a great source of guidance and have set an excellent example for me to learn from. I am grateful for the insightful discussions. I would like to thank Ting for your invaluable support during my first project in my Ph.D. program. Thank you for your patience and guidance that help me navigate through the challenges. I am also deeply impressed by your talent and work ethic, which have served as an inspiration for me throughout my time in the program. I would like to thank Meng, Zhenglu and Fangzhou with whom I have spent a significant amount of time not only working on scientific ideas but also exploring the vibrant life of Berkeley. It has been a pleasure to share new experiences and discoveries with you. The moments we spent together will be an invaluable treasure for me. Chin-Shen, I appreciate your constant support and willingness to discuss any topic both in science and in life. Our conversations have been joyful and enlightening. I would like to express my appreciation to Mit, Jiawei and Chen for the joyful time we spent I look forward to continuing our friendship beyond our time in the Louie group. Woochang and Weichen, Thank you for the fruitful discussion on the whiteboard of our office. I would also like to thank Yang-hao, Gabriel, Andrea, Yea-Lee, Brad, Fang, Omar, James and Jack. I have learned so much from each of you, and our time together has been full of insights and sweetness.

I would like to express my gratitude to my experimental collaborators, Prof. Michael F. Crommie and his students Daniel J. Rizzo, Peter Jacobse, and Ziyi Wang, as well as Prof. Felix R. Fischer and his students Gregory Veber, Ryan McCurdy, Ethan Chi Ho Wen, Aidan Delgado, Boyu Qie, and Prof. Cong Su. Our collaborations have been truly enlightening, deepening and widening my understanding of science significantly. I am grateful for the opportunity to work with such talented individuals, and for the valuable knowledge and experience I have gained through our collaborations.

I would like to extend my heartfelt thanks to my dissertation and qualifying exam committee members: Prof. Alex Zettl, Prof. Michael F. Crommie, and Prof. Felix R. Fischer.

Thank you for your kindness and patience in my qualification. I am truly grateful for the feedback and guidance throughout the process.

I would like to extend my thanks to Donna, Katherine, Joelle, Arica, and Maria for their professional support that make my Ph.D. such a smooth and pleasant experience.

Last but not least, I would like to express my gratitude to my parents for their endless and unconditional support throughout my life. Their unwavering love and encouragement have been a constant source of strength and inspiration for me. I am truly blessed to have them in my life, and I could not have achieved what I have without their guidance and support.

Chapter 1

Introduction

1.1 Density Functional Theory

Kohn-Sham Equation

The Hohenberg-Kohn theorem forms the basis of the density-functional theory (DFT), which asserts that the electron density of a ground-state system determines its ground-state wavefunction and the expectation value of any observable physical quantity. The minimum value of the total energy functional of the density corresponds to the true ground-state density. However, this theorem only establishes the existence of such an energy functional, without providing any information about its actual form. Different approximations have been made to address this issue. The Kohn-Sham approach furthers the practicality of the approach by utilizing a single-particle potential $V_{KS}(r)$ that can be tailored to generate the same ground-state electron density for an effective one-body problem[9]. This allows for the creation of a self-consistent procedure to determine the ground-state energy and density.

A single-particle Schrödinger equation [10][11] can be used to describe a noninteracting auxiliary problem, expressed as

$$[-\frac{\hbar^2}{2m_e}\nabla^2 + V_{KS}(r)]\psi_i(r) = \epsilon_i\psi_i(r) \tag{1.1}$$

where m_e represents the electron mass. This auxiliary problem is associated with an electron density given by

$$n_e(r) = \sum_i^{occ} |\psi_i(r)|^2 \tag{1.2}$$

where the summation is taken over all the occupied states. The many-body wavefunction for this noninteracting system is a Slater determinant formed by all the single-particle wavefunctions ψ_i. The exchange-correlation energy $E_{xc}[n_e(r)]$ is introduced as a functional of n_e, which accounts for all the corrections beyond the Hartree approximation to the many-body problem. The exchange-correlation potential is defined as the derivative of E_{xc} with respect to the variation of electron density, i.e., $V_{xc}[n_e(r)] = \frac{\delta E_{xc}}{\delta n_e(r)}$.

Taking external field and Hartree potential into account, we can derive the well-known Kohn-Sham equation

$$[-\frac{\hbar^2}{2m_e}\nabla^2 + V_H(r) + V_{xc}[n_e(r)]]\psi_i(r) = \epsilon_i\psi_i(r) \tag{1.3}$$

where $V_H(r) = \int \frac{n(r')e^2}{4\pi\epsilon_0|r-r'|}dr'$ represents the Hartree potential and V_{ext} is the external potential [10]. With knowledge of the form of $V_{ext}(r)$, such as ionic potentials or external electromagnetic fields, and the exchange-correlation potential, we can self-consistently calculate the ground-state density and energy using Eq. 1.2 and Eq. 1.3. This procedure is theoretically exact when we acquire the exact V_{xc}. In reality, an approximate $V_{xc}[n_e(r)]$ is required to begin with. In the local-density approximation (LDA), we assume that the exchange-correlation potential V_{xc}^{LDA} can be approximated as a function of only the local electron density, leading to the exchange potential with the form:

$$V_x^{LDA}(r) = -q_e^2(\frac{3}{\pi})^{1/3}n_e^{1/3}(r) \tag{1.4}$$

for slowly varying $n_e(r)$ [12]. Various parameterized analytical forms have been used for the correlation part, such as the Ceperley-Alder data with Perdew-Zunger parametrization [13][14]. In the generalized gradient approximation (GGA), the exchange-correlation energy is written as a function of both the density and the gradient of the density [14][15][16]. So far, we have only considered non-magnetic systems, where the density of spin-up and spin-down states are degenerate. In magnetic systems, both the densities of spin-up and spin-down are required to evaluate Kohn Sham equation. Under local spin approximation (LSDA), the Kohn-Sham equation could be written as:

$$[-\frac{\hbar^2}{2m_e}\nabla^2 + V_H + V_{xc}[n_\uparrow(r), n_\downarrow(r)] - \frac{1}{2}g_e\mu_B\sigma B]\psi_i\sigma(r) = \epsilon_i\sigma\psi_i\sigma(r) \tag{1.5}$$

Under this case, both the energies and the wavefunctions can be different for each spin. These features are all implemented in Quantum ESPRESSO package [17][18] which we will use to perform DFT calculations introduced in later chapters.

1.2 Many-Body Problem

The electronic structure in solids is a complex problem that involves a vast number of electrons, ions, and interactions with external environment. Due to the form of Coulomb interaction, it is a many-body problem, with the number of particles involved being around the Avogadro's constant. To address this problem, quantum field theory and many-body perturbation theory (MBPT) are used, which are based on the Green's function method. The GW and GW-BSE methods are derived from MBPT, and they are considered powerful and versatile formalisms in physics. This section presents essential concepts and conclusions relevant to the development of these methods, focusing only on the Green's function formalism for electrons. More information and other topics related to MBPT can be found in various textbooks and reviews[10][19][20]. The starting point is a general Hamiltonian H_{exact}

under second quantization that describes a system of interacting electrons under an external potential ($V_{ext}(r)$).

$$\hat{H}_{exact} = \int c_r^\dagger [-\frac{\hbar^2}{2m_e}\nabla^2 + V_{ext}(r)] c_r dr + \int V_{coul}(r,r') c_r^\dagger c_{r'}^\dagger c_r c_{r'} dr dr' \tag{1.6}$$

where $V_{coul}(r,r') = \frac{e^2}{4\pi\epsilon_0|r-r'|^2}$ is the Coulomb interaction. c_r and $c_r^\dagger$ are the field operator annilating and creating an electron at position r, respectively. The second term in Eq. 1.6 is a two-body operator. This triggers the difficulties of solving the eigenstate and eigen energies of this Hamiltonian, as the bases size grows with the system size as power law ($\sim 2^N$ where N is the number of electrons). Most of the time, people are interested in the excitation properties, but not the ground state properties. However, DFT is a ground state theory and does not describe the excited state accurately. To touch the excited state properties, a new tool has to be used here, which is the many body Green's function theory.

The time-ordered Green's function at zero-temperature is defined as

$$G(rt, r't') = -i\langle 0|T[c_r(t)c_{r'}^\dagger(t')]|0\rangle \tag{1.7}$$

Here, T is the time-ordered operator. $c_r(t)$ and $c_{r'}^\dagger(t')$ are the field operators in Heisenberg picture. and $|0\rangle$ is the ground state of the system. To expand the Green's function explicitly:

$$G(rt, r't') = -i\langle 0|c_r(t)c_{r'}^\dagger(t')|G\rangle\theta(t-t') + i\langle G|c_{r'}^\dagger(t')c_r(t)|0\rangle\theta(t'-t) \tag{1.8}$$

On the other hand, the Green's function that directly connects with the experimental measurment if the retarded Green's function:

$$G(rt, r't') = -i\langle G|c_r(t)c_{r'}^\dagger(t') + c_{r'}^\dagger(t')c_r(t)|G\rangle\theta(t-t') \tag{1.9}$$

Next, we will derive the Dyson's equation using functional derivatives. By adding an external time-dependent perburbation to Eq. 1.6:

$$H = \hat{H}_{exact} + H'(t) \tag{1.10}$$

where

$$\hat{H}' = \int c_r^\dagger \varphi(r,t) c_r dr \tag{1.11}$$

Note that H' depends on t even in the Schrödinger picture. From now on, we combine the position and time index into one uniform index: $1 \to \{r_1, t_1\}$. By definition, the susceptibility is the density response to the external potential, defined as:

$$\chi(1,2) = \frac{\langle \delta n(1)\rangle}{\varphi(2)} \tag{1.12}$$

and the inverse dielectric function is the change of total classical potential with respect to the external field:

$$\epsilon^{-1}(12) = \frac{\delta V_{tot}(1)}{\delta\varphi(2)} = \frac{\delta(\varphi(1) + V_H(1))}{\delta\varphi(2)} = \delta(12) + \int V_{coul}(13)\chi(32)d3 \tag{1.13}$$

The screened Coulomb interaction $W(12)$ could be written as:

$$W(12) = \int \epsilon^{-1}(13) V_{coul}(32) d3 \tag{1.14}$$

If we define irreducible susceptibility as

$$\chi^*(12) = \frac{\langle \delta n(1) \rangle}{V_{tot}(2)} \tag{1.15}$$

$W(12)$ could be rewritten as

$$W(12) = V_{coul}(12) + \int V_{coul}(13) \chi^*(34) W(42) d34 \tag{1.16}$$

Until this point, we haven't seen any connection between the quantities we defined above and the Green's function. From the equation of motion, we could derive that the Green's function satisfies:

$$(i\hbar \frac{\partial}{\partial t_1} + \frac{\hbar^2}{2m_e} \nabla_1^2) G(12) - \int \Sigma(13) G(32) d3 = \delta(12) \tag{1.17}$$

where the self-energy $\Sigma(12)$ is defined as

$$\Sigma(12) = \Sigma_H(12) + M(12) \tag{1.18a}$$

$$\Sigma_H(12) = \delta(12) \int V_{coul}(12) \langle n(2) \rangle d2 \tag{1.18b}$$

$$M(12) = i\hbar \int V_{coul}(13) \frac{\delta G(14)}{\delta \varphi(3)} G^{-1}(42) \tag{1.18c}$$

With the help of non-interacting Green's function $G_0(12)$ corresponding to Hamiltonian without the Coulomb interaction.

$$G(12) = G_0(12) + \int G_0(13) \Sigma(34) G(42) d34 \tag{1.19}$$

To evaluate self-energy $\Sigma(12)$, we define irreducible vertex function as

$$\Gamma^*(123) = -\frac{\delta G^{-1}(12)}{\delta V_{tot}(3)} = \delta(12)\delta(23) + \int \frac{\delta M(12)}{\delta G(45)} G(46) G(75) \Gamma^*(673) d4567 \tag{1.20}$$

This helps us to rewrite $M(12)$ as

$$M(12) = i\hbar \int G(13) W(41) \Gamma^*(324) d34 \tag{1.21}$$

The irreducible susceptibility χ^* is also related to the irreducible vertex function Γ^* by

$$\chi^*(12) = -i\hbar \int G(13) G(41) \Gamma^*(342) d34 \tag{1.22}$$

Combining the above equation, we have 5 variables: G, W, χ^*, Γ^*, M and 5 equations:

$$G(12) = G_0(12) + \int G_0(13)(\Sigma_H(34) + M(34))G(42)d34 \tag{1.23a}$$

$$W(12) = V_{coul}(12) + \int V_{coul}(13)\chi^*(34)W(42)d34 \tag{1.23b}$$

$$\chi^*(12) = -i\hbar \int G(13)G(41)\Gamma^*(342)d34 \tag{1.23c}$$

$$\Gamma^*(123) = \delta(12)\delta(23) + \int \frac{\delta M(12)}{\delta G(45)} G(46)G(75)\Gamma^*(673)d4567 \tag{1.23d}$$

$$M(12) = i\hbar \int G(13)W(41)\Gamma^*(324)d34 \tag{1.23e}$$

This series of equations are called Hedin's equations.[19][21]

1.3 GW Approximation

The 5 Hedin's equations shown in the last section could be used to solve Green's function, self-energy, screened Coulomb interaction and so on self-consistently. But require challenging computational power. A common approximation used is to take the first order of the vertex function, namely:

$$\Gamma^*(123) = \delta(12)\delta(13) \tag{1.24}$$

This reduces the Hedin's equations to 4 self-consistent equations:

$$G(12) = G_0(12) + \int G_0(13)(\Sigma_H(34) + M(34))G(42)d34 \tag{1.25a}$$

$$W(12) = V_{coul}(12) + \int V_{coul}(13)\chi^*(34)W(42)d34 \tag{1.25b}$$

$$\chi^*(12) = -i\hbar G(12)G(21) \tag{1.25c}$$

$$M(12) = i\hbar G(12)W(21) \tag{1.25d}$$

This is called GW approximation because of the form of the self-energy $M(12)$.

In practice, we start with Green's function from DFT level:

$$G_0(r_1, r_2; \omega) = lim_{\eta \to 0} \sum_{nk} \frac{\psi_{nk}^{DFT}(r)\psi_{nk}^{DFT*}(r')}{\omega - \epsilon_{nk}^{DFT} + i\eta * sgn(\epsilon_{nk}^{DFT} - \epsilon_F)} \tag{1.26}$$

We use Eq. 1.25c to evaluate χ^*. The dielectric function could be calculated as

$$\epsilon(12) = \delta(12) - \int V_{coul}(13)\chi^*(32)d3 \tag{1.27}$$

inverse the dielectric function, we obtain screened Coulomb interaction:

$$W(12) = \int \epsilon^{-1}(13) V_{coul}(32) d3 \tag{1.28}$$

Using Eq. 1.25d, we get the self-energy $M(12)$, substitute into Eq. 1.25a, we complete the self-consistent cycle and obtain the Green's function for the next iteration($G_1(12)$). When the self-consistent evaluation is converged, we obtain the final Green's function, inversing it gives us the quasi-particle Hamiltonian.

This quasiparticle Hamiltonian corresponds to the effective Hamiltonian of single-particle excitations. It can be directly linked to experiments such as scanning tunneling microscope measurements (STM), angle-resolved photoemission spectroscopy (ARPES), and others. All of these measurements involve tunneling or extracting single electrons/holes from the system, which is precisely the phenomenon that the above theory is designed to be applied to.

In reality, instead of doing fully self-consistent calculation, the most common practice is to do a one-shot G_0W_0 calculation. That is to stop the evaluation after we obtain $G_1(12)$. The GW method we will use in the later chapter is calculated via BerkeleyGW package [22][23]. For convenience, the package calculates each quantity in the reciprocal and frequency domain.

1.4 Bethe-Salpeter Equation

In the last section, we discussed about GW approximation to calculate quasi-particle excitation which is inferred from single particle Green's function. The result is generally used to compare with experiment such STM and ARPES. Other experimental measurements such as optical absorption introduce two particle excitation to the system. Namely, the electron of the system absorbs the light and is excited to a higher energy state, leaving a hole behind. The electron-hole interaction binds them together and an exciton is formed. The light excited the system, creating a hole and an electron at the same time. This phenomenon is related to two-particle correlation function:

$$L(1234) = -G_2(1234) + G(12)G(34) \tag{1.29}$$

where $G(1234)$ is the two-particle Green's function defined as

$$G_2(1234) = (\frac{-i}{\hbar})^2 \langle 0|T[c_{r_1}(t_1)c_{r_2}(t_2)c^\dagger_{r_3}(t_3)c^\dagger_{r_4}(t_4)]0\rangle \tag{1.30}$$

Using the $L_0 = G_0(14)G_0(32)$ for non-interacting system:

$$L(1234) = L_0(1234) + \int L_0(1265)K(5678)L(8734)d5678 \tag{1.31}$$

where the kernel function K is defined as:

$$K(5678) = \frac{\delta\Sigma(56)}{\delta G(87)} = \frac{\delta(\Sigma_H(56) + M(56))}{\delta G(87)} \tag{1.32}$$

Under GW approximation, and ignoring $\delta W/\delta G$:

$$K(5678) = i\hbar\frac{\delta(\Sigma_H(56) + G(56)W(65))}{\delta G(87)} = -i\hbar\delta(56)\delta(78)V_{coul}(58) + i\hbar\delta(58)\delta(67)W(65) \tag{1.33}$$

The kernel function could be constructed after the GW calculation, with screened Coulomb interaction. To obtain the excitonic wavefunction and excitonic level, We expand L by [24]:

$$L(121'2';\omega) = i\sum_S \frac{\chi_S(r_1, r_1')\chi_S^*(r_2', r_2)}{\omega - \Omega^S} - \frac{\chi_S(r_2, r_2')\chi_S^*(r_1', r_1)}{\omega + \Omega^S} \tag{1.34}$$

where

$$\chi_S(r, r') = -\langle 0|c_{r'}^\dagger c_r|S\rangle \tag{1.35}$$

$|S\rangle$ is the two-particle excited state and Ω^S denotes the excitonic energy level. If we assume the ground state is single-particle DFT ground state, then $\chi_S(r, r')$ could be expanded by single particle eigenstate from DFT calculation:

$$\chi_S(r, r') = \sum_v^{occ}\sum_c^{unocc} A_{vc}^S\psi_c(r)\psi_v^*(r') \tag{1.36}$$

We call A_{vc}^S as the envelop function of the excitonic state. Using Tamm-Dancoff approximation (TDA) [25]-[26], the BSE equation using DFT results could be written as:

$$(\epsilon_{ck}^{DFT} - \epsilon_{vk}^{DFT})A_{vck}^S + \sum_{v'c'} K_{vck,v'c'k'}A_{v'c'k'}^S = \Omega^S A_{vck}^S \tag{1.37}$$

This equation is also implemented in BerkeleyGW package [24].

Chapter 2

Topology Classification using Chiral Symmetry and Spin Correlations in Graphene Nanoribbons

In this chapter, we apply the topological classification theory using chiral symmetry to graphene nanoribbons (GNRs). This approach eliminates the requirement of time-reversal and spatial symmetry in previous Z_2 topology theory, resulting in a Z classification with the conventional Z index in a new vector-formed expression called "chiral phase index" (CPI). Our approach is applicable to GNRs of arbitrary terminations and any quasi-one-dimensional chiral structures, including magnetism. It naturally solves a recent experimental puzzle of junction states at a class of asymmetric GNR junctions. We moreover derive a simple analytic formula for the CPI of armchair GNRs. Since this approach enables access to electron spin behavior, based on the CPI, we design a novel GNR with periodic localized moments and strong spin-spin exchange coupling.

2.1 Introduction

Topology classification theory has broadly been applied to explain many physical phenomena such as quantum Hall insulators,[27]-[28] quantum spin Hall insulators,[29],[30] topological insulators, and superconductors.[31]-[32] However, the power of topology theory has not been as widely used in quasi one-dimensional (1D) systems. The recently developed bottom-up molecular precursors technique enables the synthesis of atomically precise graphene nanoribbons (GNRs).[33]-[34] These structurally precise 1D materials, with different structures, have been predicted to possess band gaps due to quantum confinement and interaction effects,[35],[36] while graphene is a semimetal. Since the discovery of distinct topological phases in GNRs,[37] topology classification in GNRs has proven to be highly successful in predicting the emergence of topological in-gap states localized at the boundaries and junctions of such GNRs.[37]-[38] However, for example, the topological origin of the observed robust junction states between a bearded termination of armchair GNRs[39] (AGNRs) and of the formation of a metallic 5-sawtooth-GNRs (5-sGNRs) based on in-gap states[2] between segments of AGNRs is still unclear. In the former kind of junctions [Fig.

2.3(c)], as spatial symmetry in the commensurate unit cell on both sides of the junction does not exist, the previous Z_2 topology theory based on spatial symmetry[37] loses its predictive power. To overcome this conceptual issue, we utilize the topology classification theory using chiral symmetry[40],[32],[41],[42] and apply this approach to GNRs.

2.2 Chiral Symmetry Topology Classification

Chiral symmetry generally exists in a honeycomb structure of similar atoms if the second-nearest-neighbor interaction can be neglected. As discussed below, we note that spatial and time-reversal symmetries can exist exactly in many 1D structures (even with a strong second-nearest-neighbor interaction); however, chiral symmetry can be used as an excellent approximate symmetry for GNR structures, especially when other symmetries do not exist. Mathematically, chiral symmetry for a system with Hamiltonian H refers to having an operation Γ satisfying[40]

$$H = -\Gamma H \Gamma^{-1}, \Gamma\Gamma^{\dagger} = 1, \Gamma^2 = 1 \tag{2.1}$$

The operation Γ does not depend on any specific spatial coordinates, and thus it can easily be preserved when a crystal system is terminated at a boundary. Chiral symmetry exists in bipartite lattices, in which the system can be divided into two sublattices, A and B, such that after an appropriate energy shift there are only nonzero interaction matrix elements between basis functions on the different sublattices. For such a system, Eq. (2.1) is satisfied by using an atomic-site orbital basis and setting Γ to a diagonal matrix with matrix elements equal to 1 for the A sublattice part and -1 for the B sublattice part. Graphene is a bipartite lattice system within a tight-binding formalism, with only first-nearest-neighbor hopping included. Within this spirit, we may analyze the electron topological properties of GNRs or any other approximate bipartite 1D structures, using chiral symmetry, and treat subsequently small second-nearest-neighbor or other chiral-symmetry-breaking effects perturbatively. To derive the bulk index for the GNRs and other bipartite quasi-1D systems, we use a first-nearest-neighbor tight-binding model and follow the standard Fermion-projector method.[40],[32] The Fermion projector is a Hermitian operator defined as

$$Q_k = \sum_{n}^{N_{unocc}} |\psi_{nk}\rangle\langle\psi_{nk}| - \sum_{n}^{Nocc} |\psi_{nk}\rangle\langle\psi_{nk}| \tag{2.2}$$

where $|\psi_{nk}\rangle$ stands for Bloch states of band n and wavevector k. N_{unocc} is the number of unoccupied bands, and $N_{occ} = N_{unocc}$ is the number of occupied bands. Q_k can be understood as a continuous deformation of the original Hamiltonian in k-space H_k, which has a gapped spectrum around the charge-neutrality energy, by moving energies of the occupied bands to -1 and unoccupied ones to 1, while keeping the eigenvectors unchanged. Under chiral symmetry, Q_k could be brought into an off-diagonal form using localized site basis. In the case of GNRs, we use the π orbitals of the carbon atoms. Under such basis, Q_k could be written in the matrix form

$$Q_k = \begin{bmatrix} 0 & U_k \\ U_k^{\dagger} & 0 \end{bmatrix} \tag{2.3}$$

Combined with the above properties, it was proved that U_k belongs to a unitary group $U(N_{occ})$; the classification is given by the homotopy group $\pi_1(U(N_{occ})) = Z$, and the bulk index is the first odd Chern number written as [38], [42]

$$Ch_1(U) = \frac{-i}{2\pi}\int_{1DBZ} Tr(U_k^\dagger \partial_k U_k)\mathrm{d}k \tag{2.4}$$

2.3 Chiral Phase Index

Although Eq. 2.4 has been broadly used in mathematics, it is inconvenient to use the matrix form to evaluate physical quantities. Here, we use the properties of the wave functions under chiral symmetry to bring the bulk index given in Eq. 2.4 equivalently into a vector form, which we shall call such bulk index for reasons below as a chiral phase index (CPI).

From Eq. 2.1, We know that Hamiltonian H_k anti-commute with the chiral operator Γ, that is $H_k\Gamma = -\Gamma H_k$. This gives us the following properties in the eigen-wavefunctions

$$H_k\Gamma|\psi_{nk}\rangle = -\Gamma H_k|\psi_{nk}\rangle = -E_{nk}\Gamma|\psi_{nk}\rangle \tag{2.5}$$

Written in the atomic base, we have

$$\Gamma\begin{pmatrix}\alpha_{nk}\\ \beta_{nk}\end{pmatrix} = \begin{pmatrix}\alpha_{nk}\\ -\beta_{nk}\end{pmatrix} = \begin{pmatrix}\alpha_{mk}\\ \beta_{mk}\end{pmatrix} \tag{2.6}$$

where the eigen-energy E_m and E_n satisfy $E_m = -E_n$. α_{nk} and β_{nk} are vectors representing the A sublattice components and the B sublattice components, respectively. I will show in the following that Eq. (2.4) could be brought into vector form

$$Z = \frac{-i}{\pi}\sum_{n\in occ} inter(\int_{1DBZ}\langle u_{nk}|\Gamma\partial_k|u_{nk}\rangle \mathrm{d}k) \tag{2.7}$$

Here *inter* means taking only the intercell part of the above expression.[43] u_{nk} is the periodic part of the Bloch states. Using expression in Eq. (2.6), We could rewrite the matrix U_k as

$$U_k = \sum_n^{N_{unocc}} \alpha_{nk}\otimes\beta_{nk}^\dagger - \sum_m^{Nocc}\alpha_{mk}\otimes\beta_{mk}^\dagger = -2\sum_n^{N_{occ}}\alpha_{nk}\otimes\beta_{nk}^\dagger \tag{2.8}$$

For convenience, we define the band index to start with -N_{occ} and end at N_{unocc}. Now the positive index denotes the unoccupied bands and the negative index denotes the occupied bands. With this labeling, we could rewrite the relation in Eq. (2.6) as Γu_{nk}. Before deriving Eq. (2.7), We need some useful identities. Noting that the wavefunctions from different bands can be made orthogonal at the same k points, u_{nk} is orthogonal to u_{mk} and u_{-mk} if $n \neq m$. This yields:

$$\sum_i \alpha_{nk}^{i*}\alpha_{mk}^i + \beta_{nk}^{i*}\beta_{mk}^i = 0 \quad (for\ n \neq m) \tag{2.9a}$$

$$\sum_i \alpha_{nk}^{i*}\alpha_{nk}^i + \beta_{nk}^{i*}\beta_{nk}^i = 1 \tag{2.9b}$$

$$\sum_i \alpha_{nk}^{i*}\alpha_{mk}^{i} - \beta_{nk}^{i*}\beta_{mk}^{i} = 0 \tag{2.9c}$$

where i labels the basis index in the unit cell, and subsequently we have:

$$\sum_i \alpha_{nk}^{i*}\alpha_{mk}^{i} = 0 \quad (for\ n \neq m) \tag{2.10a}$$

$$\sum_i \alpha_{nk}^{i*}\alpha_{nk}^{i} = \frac{1}{2} \tag{2.10b}$$

$$\sum_i \beta_{nk}^{i*}\beta_{mk}^{i} = 0 \quad (for\ n \neq m) \tag{2.10c}$$

$$\sum_i \beta_{nk}^{i*}\beta_{nk}^{i} = \frac{1}{2} \tag{2.10d}$$

Substitute Eq. (2.8) into Eq. (2.4) and use the relations in Eq. (2.10), we have:

$$Ch_1(U) = \frac{-i}{2\pi}\int_{1D\ BZ} Tr\left(U_k^{\dagger}\partial_k U_k\right)\mathrm{d}k \tag{2.11a}$$

$$= \frac{-i}{2\pi}\int_{1D\ BZ}\sum_{i,j}\sum_{n,n'}^{N_{occ}} 4\left(\alpha_{nk}^{j}\beta_{nk}^{i*}\right)^{*}\partial_k\left(\alpha_{n'k}^{j}\beta_{n'k}^{i*}\right)dk \tag{2.11b}$$

$$= \frac{-i}{2\pi}\int_{1D\ BZ} dk\ 4\sum_{i,j}\sum_{n,n'}^{N_{occ}} \alpha_{nk}^{j*}\beta_{nk}^{i}\partial_k(\alpha_{n'k}^{j})\beta_{n'k}^{i*} + \alpha_{nk}^{j*}\beta_{nk}^{i}\partial_k\left(\beta_{n'k}^{i*}\right)\alpha_{n'k}^{j} \tag{2.11c}$$

$$= \frac{-i}{2\pi}\int_{1D\ BZ} dk\ 2\sum_{i}\sum_{n}^{N_{occ}} \alpha_{nk}^{i*}\partial_k(\alpha_{nk}^{i}) + \beta_{nk}^{i}\partial_k\left(\beta_{nk}^{i*}\right) \tag{2.11d}$$

$$= \frac{-i}{2\pi}\int_{1D\ BZ} dk\ 2\sum_{i}\sum_{n}^{N_{occ}} \alpha_{nk}^{i*}\partial_k(\alpha_{nk}^{i}) - \beta_{nk}^{i*}\partial_k\left(\beta_{nk}^{i}\right) \tag{2.11e}$$

Eq. (2.11e) can be derived using relation $\sum_i \partial_k\left(\beta_{nk}^{i*}\beta_{nk}^{i}\right) = 0$. This thus proves Eq. (2.7), or alternately

$$Z = \frac{-i}{\pi}\int_{1D\ BZ} dk \sum_{n\in occ}\left(\alpha_{nk}^{\dagger}\partial_k\alpha_{nk} - \beta_{nk}^{\dagger}\partial_k\beta_{nk}\right) \tag{2.12}$$

Eq. (2.12) requires only the knowledge of the occupied wavefunctions, rather than full information of the Hamiltonian matrix, and is very convenient in calculating the bulk-index analytically We want to point out that the CPI is very different from that of an index obtained with the intercell part of the Zak phase used in the previous work[37],[44],[45] , namely, the intercell Zak phase is given by $\sum_{n\in occ} inter\left(\int_{1DBZ}\langle u_{nk}|\partial_k|u_{nk}\rangle\,\mathrm{d}k\right)$. The CPI is determined by the difference between the intercell part of the Zak phase contributed by the A sublattice and that contributed by the B sublattice rather than the sum of these two parts, and yields a Z classification rather than a Z_2 classification.

An important general consequence of Eq. (2.7) is that the CPI is fully gauge-invariant. Applying a gauge transformation to the wavefunction, $\alpha_{nk} \to \alpha_{nk} e^{if_n(k)}$ and $\beta_{nk} \to \beta_{nk} e^{if_n(k)}$, from Eq. (2.7), the CPI changes to:

$$\begin{aligned} Z = & \frac{-i}{\pi} \int_{1DBZ} dk \sum_{n\in occ} \left(\alpha_{nk}^{\dagger} \partial_k \alpha_{nk} - \beta_{nk}^{\dagger} \partial_k \beta_{nk} \right) \\ & + \frac{1}{\pi} \int_{1D\ BZ} dk \sum_{n\in occ} \left(\alpha_{nk}^{\dagger} \alpha_{nk} \partial_k f_n(k) - \beta_{nk}^{\dagger} \beta_{nk} \partial_k f_n(k) \right) \end{aligned} \tag{2.13a}$$

$$= \frac{-i}{\pi} \int_{1D\ BZ} dk \sum_{n\in occ} \left(\alpha_{nk}^{\dagger} \partial_k \alpha_{nk} - \beta_{nk}^{\dagger} \partial_k \beta_{nk} \right) + 0 \tag{2.13b}$$

From Eq. (2.13a) to Eq. (2.13b), we have used the relation given by Eq. (2.10). This gauge-invariant property is an essential character of the CPI, leading to its value being an integer number of any value, in contrast with the Zak phase which could only be 0 or π(i.e., $Z_2 = 0$ *or* 1). We would also like to address that chiral phase index is only defined for the charge neutrality gap since chiral symmetry in the form of Eq. (2.3) has been used.

As a gauge-invariant quantity, the CPI is expected to be a measurable quantity. While the Zak phase in 1D connects with the modern theory of polarization[46], the CPI can be related to the difference between the electric dipole moments per unit cell of the two sub-lattices. However, a most straightforward way of measuring CPI would be counting the number of topological end states at the end of the system with vacuum. This quantity is connected to the bulk-index (of a unit cell commensurate to the boundary termination) by using the bulk-boundary correspondence as given in [42]: $Z_{bulk} = N_+ - N_-$ for a system that is terminated to the right. $N_{+(-)}$ is the number of zero-mode with positive (negative) chirality. States with positive (negative) chirality localize only on the A (B) sublattice. (For an AGNR, the convention used here is that, along a zigzag chain of atoms traversing across the width of the ribbon, the atom on the right is denoted as sublattice A and that on the left is denoted as sublattice B. See Fig. 2.3(b)). The number of protected in-gap end states would be equal to the number of mid-gap states of one chirality in excess over the other chirality, since pairs of states of opposite chirality can interact through perturbations at the end and move out of the bulk gap. In short, through the bulk-boundary correspondence, the CPI contains two pieces of important information at the termination of the system. Firstly, $|Z|$ gives the number of end states that are protected by chiral symmetry; and secondly, $sgn(Z)$ gives the chirality of the end states[42]. Moreover, the bulk-boundary correspondence applies when two such bulk materials with distinct CPIs are joined and topological-protected junction states are formed. One can show that the number of topological junction states, as two bulk structures with bulk index Z_{bulk}^{left} and Z_{bulk}^{right} are joined, is $N_+ - N_- = Z_{bulk}^{left} - Z_{bulk}^{right}$.

2.4 General Z Index for AGNRs

We now obtain an explicit expression for the CPI of AGNRs with different widths and end terminations using Eq. (2.12). The tight-binding wavefunctions of the GNRs may be analytically calculated from a linear combination of graphene's wavefunctions with proper

boundary conditions[37]. To get an analytic form of the CPI or Z index of an armchair graphene nanoribbon (AGNR) for a specific unit cell, we evaluate the orbital wavefunctions of the nanoribbons from those of graphene within a first-nearest-neighbor interaction model, namely:

$$H_k^{Gr} = \begin{pmatrix} 0 & -t - te^{-ik_x\frac{\sqrt{3}a}{2}+ik_y\frac{a}{2}} - te^{-ik_x\frac{\sqrt{3}a}{2}-ik_y\frac{a}{2}} \\ -t - te^{ik_x\frac{\sqrt{3}a}{2}-ik_y\frac{a}{2}} - te^{ik_x\frac{\sqrt{3}a}{2}+ik_y\frac{a}{2}} & 0 \end{pmatrix}$$

Diagonalizing this matrix, we get the periodic part of the Bloch wavefunction:

$$u_{Gr}^{\pm}(k) = \frac{1}{\sqrt{2}}\begin{pmatrix} e^{-i\phi(k)} \\ \mp 1 \end{pmatrix} \tag{2.14}$$

where + and - sign denotes the unoccupied and occupied π bands of graphene, and

$$e^{-i\phi(k)} = \frac{h_x(k) - ih_y(k)}{\sqrt{h_x^2(k) + h_y^2(k)}} \tag{2.15}$$

where

$$\begin{aligned} h_x(k) &= 1 + 2\cos\left(\frac{k_y a}{2}\right)\cos\left(\frac{\sqrt{3}k_x a}{2}\right), \\ h_y(k) &= 2\cos\left(\frac{k_y a}{2}\right)\sin\left(\frac{\sqrt{3}k_x a}{2}\right) \end{aligned} \tag{2.16}$$

Here, the x-direction is taken along the armchair direction (see Fig. 2.1), a is the length of the lattice vector of graphene, k is the wavevector measured from the Dirac point in the graphene Brillouin zone, and we have expressed all energies in units of the first-nearest-neighbor hopping energy t. The unit cell and lattice vectors of graphene are shown in Fig. 2.1. Within this model and assuming that the hopping parameter does not change in forming the AGNR, the wavefunctions of the AGNR can be obtained by a linear combination of graphene's wavefunctions with proper boundary conditions.

To begin our analysis, we first consider an AGNR with a specific unit cell that is commensurate to a bearded termination at the end of the nanoribbon as illustrated in Fig. 2.1. (A bearded termination at an AGNR end is defined to be one with a structure similar to the unit cell edge shown in Fig. 2.3(c) of the main text. Such an end termination has every pair of horizontal carbon atoms connected.) Within the tight-binding formalism, the appropriate boundary condition is that the amplitude of the wavefunction on the site of the virtual atoms beyond the nanoribbon side edge has zero magnitude (e.g., on atom 1 and atom 2 in Fig. 2.1). From the expression of $h_x(k)$ and $h_y(k)$, we have $\phi(k_x, k_y) = \phi(k_x, -k_y)$. This symmetry, along with the standing wave condition [37] (defining N to be the number of rows of carbon atoms forming the AGNR's width)

$$\frac{k_y a(N+1)}{2} = n\pi \tag{2.17}$$

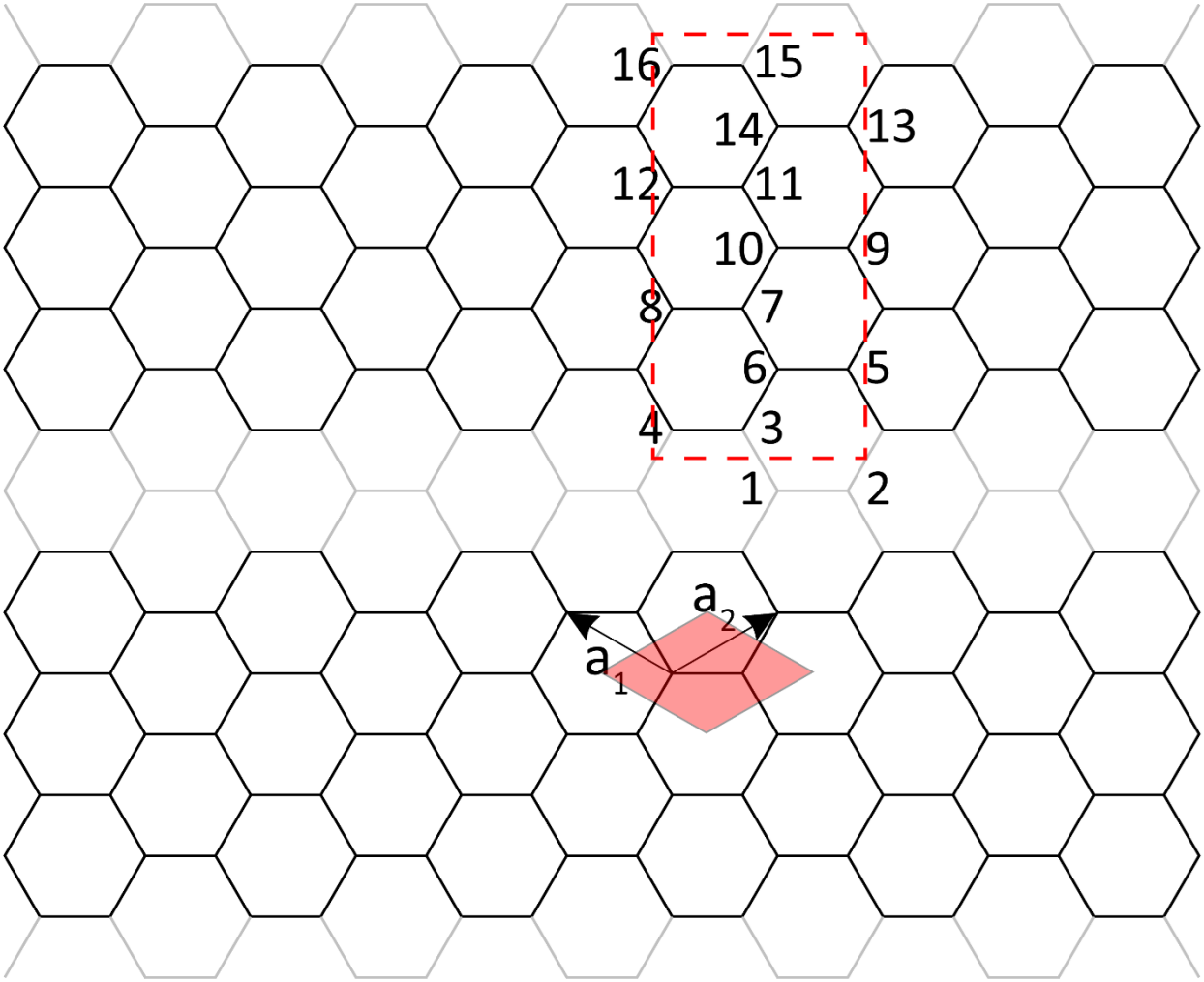

Figure 2.1: AGNR on the backbone of graphene. The darken vertices and lines correspond to carbon atoms and bonds of the AGNR, respectively. The atoms in an AGNR unit cell that are commensurate to a bearded termination (red dashed-line rectangle) are labeled 3 to 16, and the lattice vectors of pristine graphene are also shown. The unit cell of graphene is shown by the red-shaded region.

with $n = 1,\ 2 \ldots N$, ensures that, for any k_x, a symmetric combination of graphene states at k_y and $-k_y$ (with k_y satisfying Eq. (2.17)) will satisfy the required boundary condition. Thus, for each k_x, and each band of graphene, we have N pairs of $(k_y, -k_y)$ forming N AGNR bands. From the orthogonalization of the graphene wavefunctions, the AGNR's eigenstates as constructed are also orthogonal to each other. Since in total we have $2N$ bands (equal to the number of atoms in a N-AGNR's primitive unit cell), they are also complete within the defined Hilbert space.

Since the wavefunction of the empty states of a bipartite system is related to those of the occupied states, we may also use the empty states to evaluated the CPI from Eq. (2.7). The wavefunction of the empty bands of the AGNR with a unit cell consistent with bearded termination can now be written as a $2N$ column vector in the basis of π orbitals on the atoms (for the specific case of $N = 7$, on atoms 3 to 16 as shown in Fig. 2.1):

$$u_{k_y}(k_x) = \frac{i}{\sqrt{(N+1)}} \begin{pmatrix} e^{\frac{ik_x\sqrt{3}}{2}a} sin(\frac{k_y a}{2}) e^{-i\phi(k)} \\ -e^{\frac{ik_x\sqrt{3}}{2}a} sin(\frac{k_y a}{2}) \\ sin(k_y a) e^{-i\phi(k)} \\ -sin(k_y a) \\ . \\ . \\ . \\ e^{\frac{ik_x\sqrt{3}}{2}a} sin(\frac{k_y (N-1) a}{2}) e^{-i\phi(k)} \\ -e^{\frac{ik_x\sqrt{3}}{2}a} sin(\frac{k_y (N-1) a}{2}) \\ sin(\frac{k_y N a}{2}) e^{-i\phi(k)} \\ -sin(\frac{k_y N a}{2}) \end{pmatrix} \tag{2.18}$$

Substitute it into Eq. (2.7), we have:

$$Z = \sum_{k_y} \sum_{m=1}^{N} \frac{-1}{2\pi(N+1)} \left(\frac{1 - \cos(k_y m a)}{2} \right) \left[2\phi \left(\frac{2\pi}{\sqrt{3}a}, k_y \right) - 2\phi(0, k_y) \right] \tag{2.19}$$

To derive an analytic formula for the value of Z of the AGNRs, we need to investigate the change of the phase $2\phi(k)$ as one scans through the range of distinct k_x for a given k_y. From the expression of $h_x(k)$ and $h_y(k)$, we could see that the value of $2\phi(k)$ depends on the value of k_y. As shown in Fig. 2.2, for the bearded termination, if $k_y a/2$ resides in the range $\left(\frac{1}{3}\pi, \frac{2}{3}\pi\right)$, the change in $2\phi(k)$ along k_x is zero, corresponding to a winding number of zero around the origin for the function $h_x(k) + ih_y(k)$ in the complex plane. If it resides in $(0, \frac{1}{3}\pi) \cup (\frac{2}{3}\pi, \pi)$, the change in $2\phi(k)$ is 2π, corresponding to a winding number of 1. If the width of the AGNR is $N = 3p + 2$, with p an integer, $k_y a/2 = \frac{1}{3}\pi$ or $\frac{2}{3}\pi$ is possible. In this case, the winding is ambiguous and our naïve tight-binding model suggests that this type of AGNR is a metal. We will first focus on the case of $N = 3p$ or $3p + 1$, and later treat the special case of $N = 3p + 2$.

For $N = 3p$ or $3p + 1$, and using Eq. (2.17) which gives $\frac{k_y a}{2} = \frac{n\pi}{N+1}$, $n = 1, 2 \ldots N$, the number of $\frac{k_y a}{2}$ that contribute to nonzero winding is $\left\lfloor \frac{N+1}{3} \right\rfloor * 2$. Now Eq. (2.19) becomes:

$$Z = -\left\lfloor \frac{N+1}{3} \right\rfloor \tag{2.20}$$

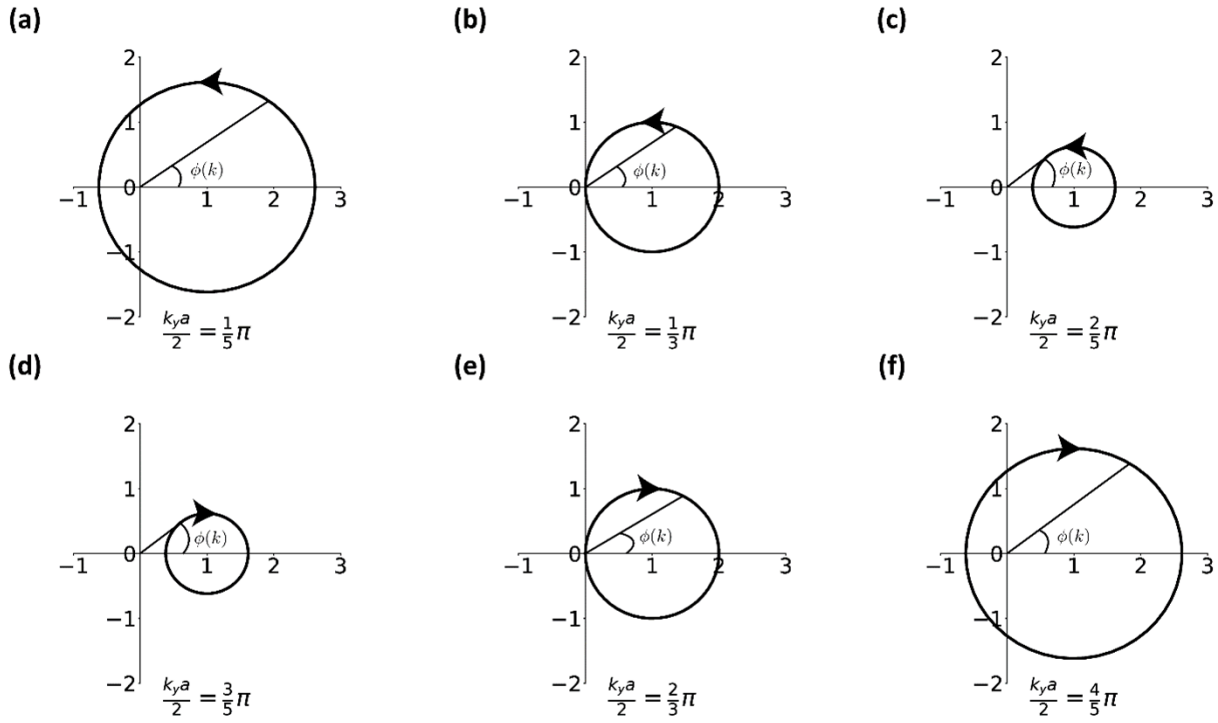

Figure 2.2: The property of $\phi(k)$ along k_x with different given k_y. Plotted in each panel is the value of $h_x(k) + ih_y(k)$ in Eq. (2.14) in the complex plane. In the plot, the parameter k_x goes from 0 to $4\pi/(\sqrt{3}a)$ rather than $2\pi/(\sqrt{3}a)$. In this way, we obtain the change in value of $2\phi(k)$ used in Eq. (2.19) and explicitly see the winding of the function $h_x(k) + ih_y(k)$ around the origin. When $(k_y a)/2 < \pi/3$ or $(k_y a)/2 > 2\pi/3$, the change in $2\phi(k)$ is 2π, and the winding number of the function $h_x(k) + ih_y(k)$ around the origin is one. When $\pi/3 < (k_y a)/2 < 2\pi/3$, the change in $2\phi(k)$ is 0 and the winding number is zero. When $(k_y a)/2 = \pi/3$ or $2\pi/3$, the change in $2\phi(k)$ depends sensitively on any possible perturbation.

We have used the relation: $\sum_{m=1}^{N} \cos\left(\frac{2nm\pi}{N+1}\right) = -1$. As stated above, the specific unit cell of the AGNR that we considered so far is the one with the bearded termination. The CPI or Z index for other nanoribbon end terminations (and hence having different shapes of bulk commensurate unit cells) can be obtained starting from the bearded termination analysis plus a gauge change. By choosing a different unit cell, we will have new wavefunctions with some components differed by a phase factor $e^{\pm ik_x\sqrt{3}a}$. These phases contribute an extra term to the chiral phase index, making the value of the Z-index to be different for different terminations. Taking this extra phase into consideration, we arrive at the general formula:

$$Z = N_{notco} \; - \left\lfloor \frac{N+1}{3} \right\rfloor \tag{2.21}$$

where N_{notco} is defined as the number of rows of atoms with carbon pairs not connected by σ bonds within the unit cell as defined in Fig. 2.3.

Next, we investigate the special case of $N = 3p + 2$ for the bearded termination in some details. Although the simple tight-binding model predicts this class of AGNRs to be metals, DFT and other higher-level calculations have shown that this type of AGNRs is insulating due to structural relaxation of the atoms (and hence their hopping parameters) at the side edge [35]. The edge modification can be considered in the tight-binding model by adding a perturbation on the hopping parameter of the edge atoms. Without the perturbation, the band gap is closed at the Fermi level at $k_x = 0$ and $k_x = \frac{\pi}{\sqrt{3}a}$. The two degenerate wavefunctions at the Γ point ($k_x = 0$) in the basis of π orbitals are:

$$u^{+}_{\frac{k_y a}{2}=\frac{2\pi}{3}}\,(k_x = 0) = \frac{i}{\sqrt{(N+1)}} \begin{pmatrix} -\frac{\sqrt{3}}{2} \\ -\frac{\sqrt{3}i}{2} \\ . \\ . \\ . \end{pmatrix}$$

$$u^{-}_{\frac{k_y a}{2}=\frac{2\pi}{3}}\,(k_x = 0) = \frac{i}{\sqrt{(N+1)}} \begin{pmatrix} -\frac{\sqrt{3}}{2} \\ \frac{\sqrt{3}i}{2} \\ . \\ . \\ . \end{pmatrix} \tag{2.22}$$

Due to a shorter bond length found in previous studies, the atoms at the edge (atoms 3 & 4 and atoms 15 & 16) have slightly bigger hopping parameters, which can be considered through a perturbation matrix:

$$\begin{pmatrix} 0 & -\Delta t & 0 & \dots \\ -\Delta t & 0 & 0 & \dots \\ 0 & 0 & 0 & \dots \\ \vdots & \vdots & \vdots & \ddots \\ 0 & 0 & 0 & -\Delta t \\ 0 & 0 & -\,\Delta t & 0 \end{pmatrix} \tag{2.23}$$

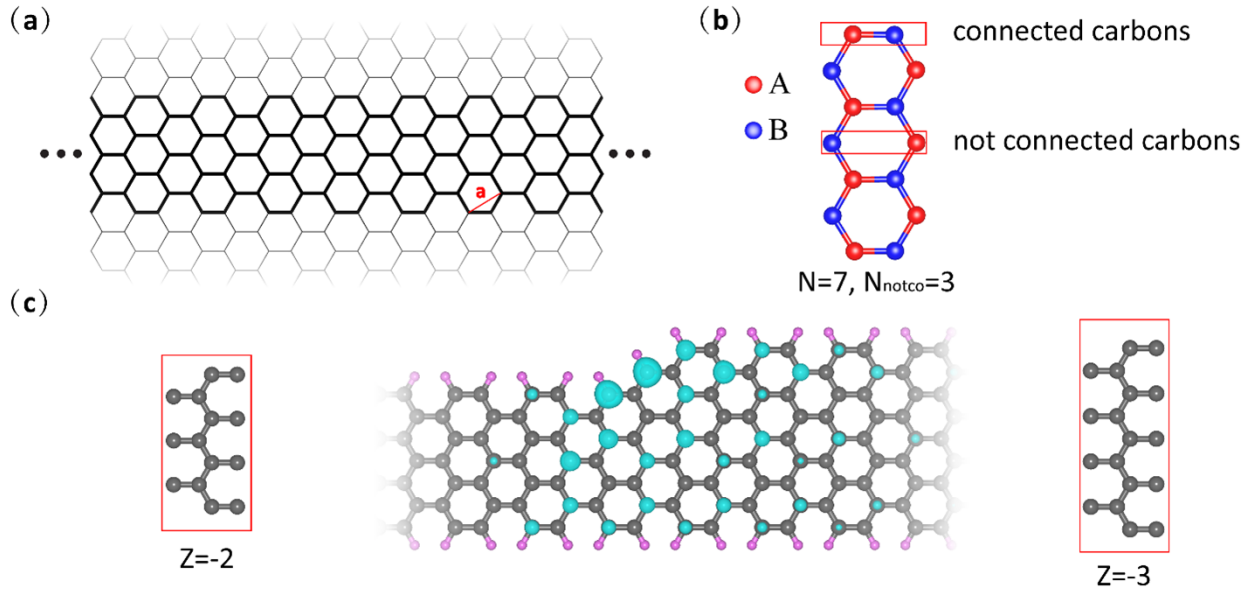

Figure 2.3: Armchair graphene nanoribbon (AGNR) is specified by the number of carbon rows N forming its width, labeled as N-AGNR. (a) Structure of 7-AGNR (bold region) from the graphene backbone background. a is the length of the lattice vector of graphene. The σ bond of the edge atoms of GNRs are typically passivated by hydrogen atoms in experiment. (b) Unit cell of a 7-AGNR with zigzag termination, the rows with two carbon connected by a σ bond within the unit cell (connected carbons), and the rows with two carbon not connected by a σ bond within the unit cell (not connected carbons) are indicated. This case corresponds to having 3 rows of not connecting pairs, $N_{notco} = 3$. (c) An asymmetric junction of 7-AGNR and 9-AGNR with bearded termination. The corresponding commensurate bulk unit cells for the two segments are shown on the sides, and the 5% isosurface of the wavefunction square (blue color) of the in-gap junction state from DFT-LDA calculation is shown in the middle.

This perturbation breaks the energy degeneracy of the two wavefunctions in Eq. (2.22). Using degenerate perturbation theory, the new conduction band minimum wavefunction is approximately equal to, in the lowest order:

$$u^{+}_{\frac{k_y a}{2}=\frac{2\pi}{3}}(k_x = 0) = \frac{i}{\sqrt{(N+1)}} \begin{pmatrix} \frac{\sqrt{3}i}{2} \\ -\frac{\sqrt{3}i}{2} \\ . \\ . \\ . \end{pmatrix} \tag{2.24}$$

Compared to Eq. (2.18), the new wavefunction equals to the old conduction band minimum wavefunction after changing from $\phi\left(k_x = 0, \frac{k_y a}{2} = \frac{2\pi}{3}\right) = -\frac{\pi}{2}$ to 0. Thus, the trajectory in Fig. 2.2(e) will change. The starting point that originally at $(0, 0)$ shifts to the right slightly to $(\epsilon, 0)$, making the change in $2\phi(k)$ vanish for $\frac{k_y a}{2} = \frac{2\pi}{3}$. A similar phenomenon happens

for the X point ($k_x = \frac{\pi}{\sqrt{3}a}$). The change in $2\phi(k)$ vanishes for $\frac{k_y a}{2} = \frac{\pi}{3}$. In conclusion, the number of $\frac{k_y a}{2}$ that contribute to nonzero winding is $(\lfloor \frac{N+1}{3} \rfloor - 1) * 2$ for $N = 3p + 2$. It is also straightforward to show that the number of nonzero winding contributions, which is $(\lfloor \frac{N+1}{3} \rfloor - 1) * 2$ for $N = 3p + 2$ and $\lfloor \frac{N+1}{3} \rfloor * 2$ for $N = 3p, 3p + 1$, can now be unified into a single expression $\lfloor \frac{N}{3} \rfloor * 2$ for an arbitrary integer N, leading to the chiral phase index for any AGNR with arbitrary width N and arbitrary end termination to be equal to:

$$Z = N_{notco} \; - \left\lfloor \frac{N}{3} \right\rfloor \tag{2.25}$$

Here N is the total number of rows of carbon atoms forming the width of the AGNR[35] and N_{notco} is the number of rows of atoms with carbon pairs not connected by σ bonds within the specific unit cell that is commensurate to an anticipated termination. The topless brackets denote the floor function which takes the largest integer less than or equal to the value within the brackets. The definition of connected carbon pairs (with distance close to $a/\sqrt{3}$) and unconnected pairs (with distance close to $\sqrt{3}a/2$) are shown in Fig. 2.3(b). Eq. (2.25) is deceptively compact and simple, as well as easy to evaluate, yet an essential finding of the analysis.

With the Z classification using chiral symmetry, the in-gap junction states localized at the asymmetric junction in Fig. 2.3 formed by bearded termination of 7-AGNR and 9-AGNR observed in experiment[39][2] could now be well explained. The bearded 7-AGNR unit cell has $Z = 2$, while the bearded 9-AGNR unit cell has $Z = -3$, giving rise to one protected in-gap state at the junction as confirmed by our explicit density functional theory (DFT) calculations within the local-density approximation (LDA) as implemented in the Quantum Espresso package[17]. Since $Z^{left}_{bulk} - Z^{right}_{bulk} = +1$, the junction state has amplitudes only on the A sublattice (Fig. 2.3(c)).

2.5 Topological Spin Chains

Eq. (2.25) can be applied to AGNRs of any general termination types that preserve chiral symmetry, not limited to the common studied zigzag, zigzag', or bearded types[37]. As shown in Fig. 2.4(a), the zigzag termination of 7-AGNR has $Z = 1$ and the "bullet" termination of 9-AGNR has $Z = -1$. When terminated to the vacuum, one in-gap end state exists at the termination of each structure. Nevertheless, the two corresponding bulk structures belong to different classes because of the opposite sign of the CPI. Two topologically protected junction states should occur when these two structures are joined, as confirmed by DFT-LDA calculation (Fig. 2.4(b)). A simple physical understanding of why these two in-gap localized states do not hybridize significantly with each other at the junction and move out of the gap is that they are localized on the same sublattice. Any interaction allowing hopping between the same sublattice would have to break chiral symmetry. In principle, for physical AGNR junctions, there may be a small energy splitting between the two junction states due to second-nearest-neighbor hopping. Our DFT-LDA results show that such splitting due to the breaking of chiral symmetry is minimal in this case. Remarkably, if the electron spin degree of freedom is considered, the junction states depicted in Fig. 2.4(b) would couple to each other ferromagnetically if one can arrange for the atomic structure of such a junction

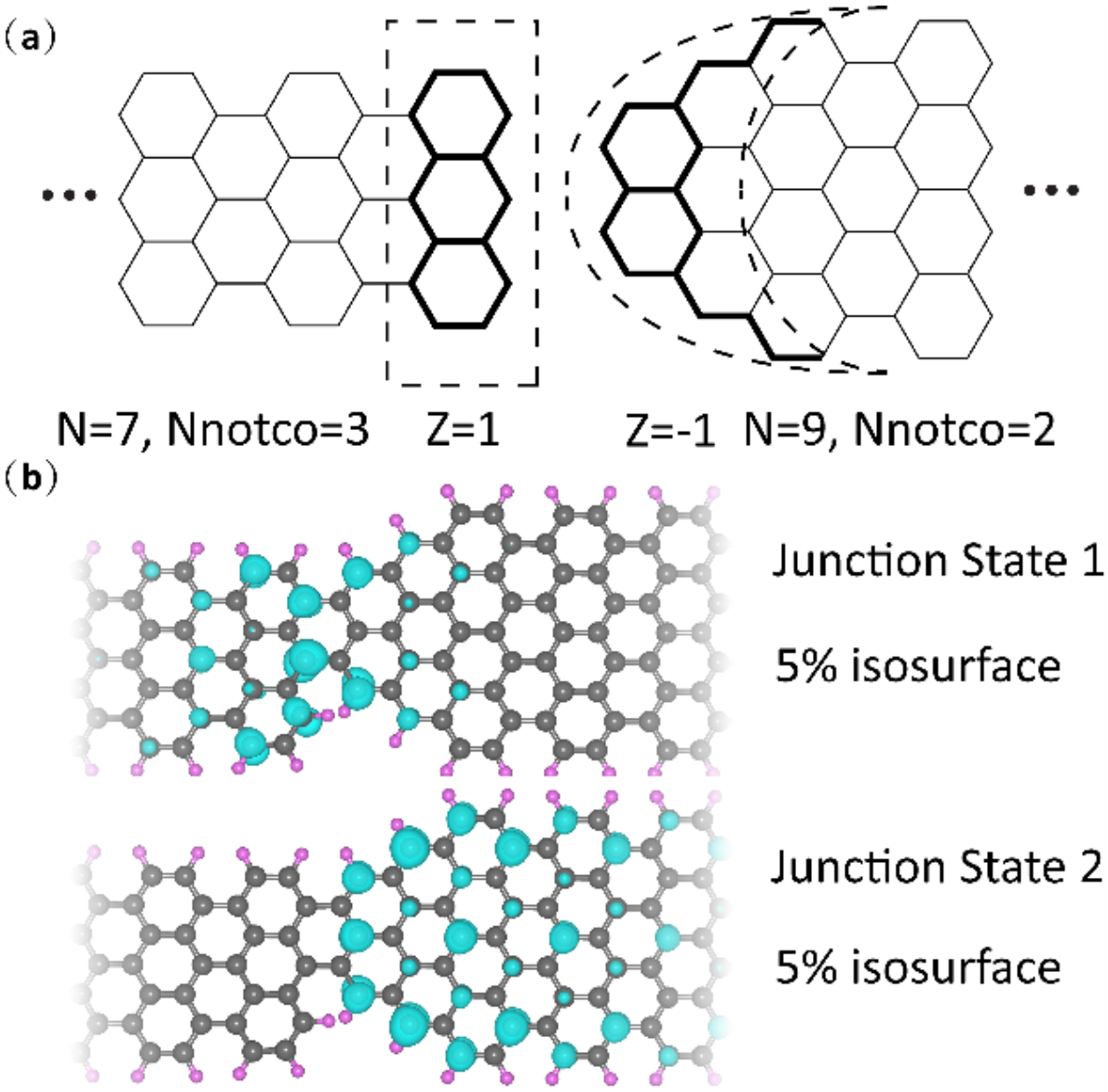

Figure 2.4: (a) Left: a 7-AGNR with zigzag termination is shown; the unit cell commensurate with the termination has 3 rows of unconnected carbons pairs and $Z = 1$. Right: a "bullet" termination of 9-AGNR is shown. Its commensurate unit cell has 2 rows of unconnected carbons pairs and $Z = -1$. (b) Joining the two structures in (a) results in a junction with $\Delta Z = 2$, giving rise to two in-gap junction states. The 5% isosurface of the wavefunction square of the two junction states from a DFT-LSDA calculation are shown in blue. Here only the occupied spin-up states are shown. One state localizes in the 7-AGNR region; the other localizes in the 9AGNR region.

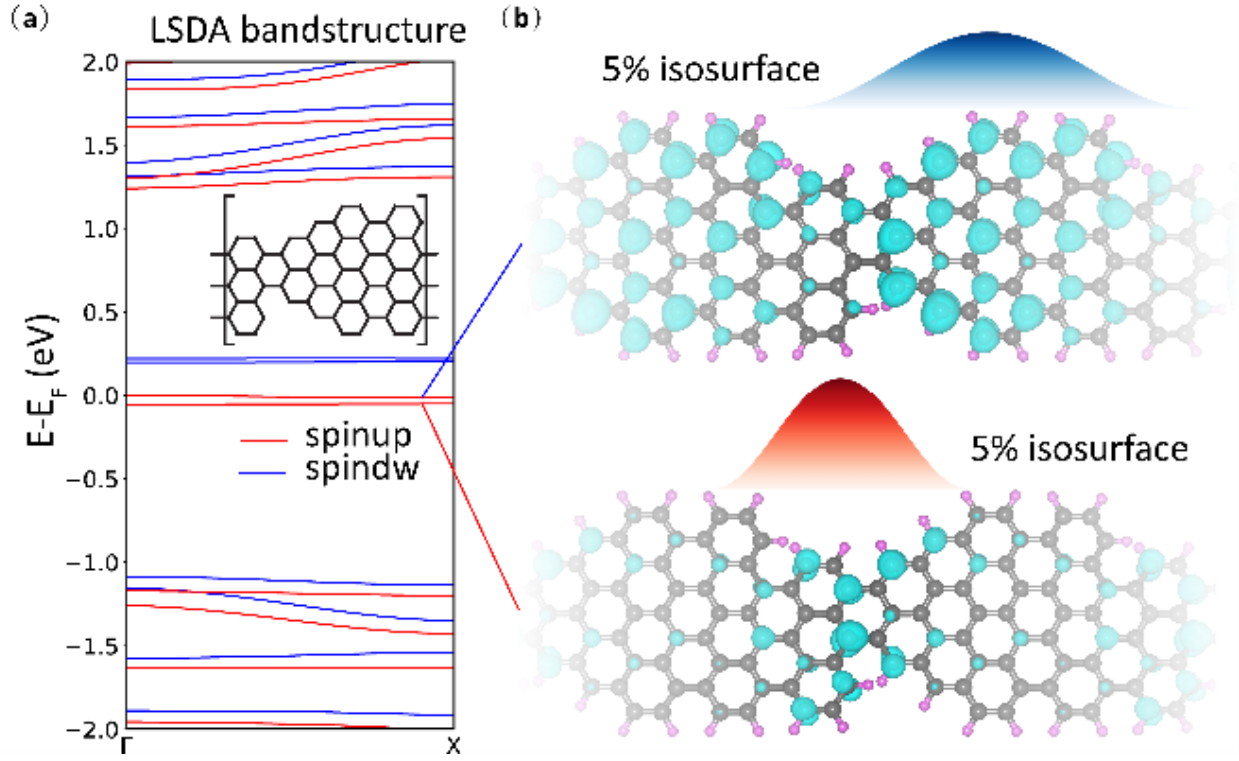

Figure 2.5: (a) Computed DFT-LSDA band structure of a periodic GNR spin chain structure (unit cell shown by insert). Top of the occupied bands is set at zero. The in-gap bands (in window -0.1 to 0.3 eV) are nearly flat, indicating negligible hopping between neighboring junction states. A spin-splitting of 0.2 eV occurs between oppositely oriented spin bands; the two majority-spin (spin-up) bands are occupied, leaving their spin-down counterparts empty. Each unit cell has two Bohr magnetons of magnetization. (b) The isosurface at 5% of the wavefunction square of the two occupied junction states at $k = \Gamma$ is shown (blue color). One is localized in the 9-AGNR region while the other is localized in the 7-AGNR region.

to have locally a sublattice imbalance of two carbon atoms, according to Lieb's theorem[47]. And if such junctions were repeated into a 1D superlattice, a 1D ferromagnetic spin chain would form. The insert in Fig. 2.5(a) illustrates the unit cell of such a superlattice we designed. Since each superlattice unit cell has a sublattice imbalance of two atoms, we have a net magnetization of two Bohr magnetons per unit cell. We have confirmed this prediction by performing a DFT-LSDA calculation, and the magnetization is found to be mainly contributed by the two occupied symmetry-protected junction states (Fig. 2.5), in agreement with the conclusion of our topology theory and Lieb's theorem. Since the direct exchange coupling J between two electron spins is proportional to their wavefunction overlap, having the two states mainly localized near the same junction is expected to give rise to a strong exchange coupling. To analyze the magnetic properties of such a chain, we map the

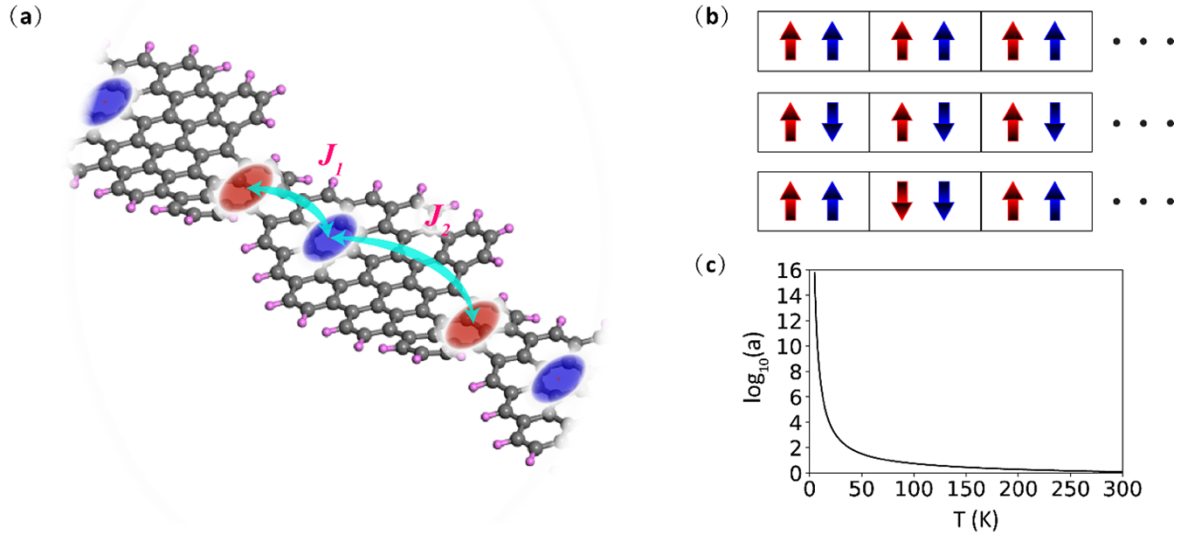

Figure 2.6: (a) Schematic of a 1D GNR spin chain (Fig. 2.5) and exchange interactions (J_1 and J_2). (b) Three different spin configurations are considered in first-principles DFT-LSDA calculations to extract the exchange coupling parameters. (c) Spin-spin correlation length (in unit of lattice vector and log scale) as a function of temperature from a classical canonical ensemble of 1D Ising model.

LSDA results to those of a 1D Ising model Hamiltonian with two spins per unit cell:

$$H = \sum_i J_1 \hat{s}_{i,1z} \hat{s}_{i,2z} + J_2 \hat{s}_{i,2z} \hat{s}_{i+1,1z} \tag{2.26}$$

where i denotes the unit cell index. To extract the coupling strengths, J_1 and J_2, from first-principles calculations, we consider three different spin configurations shown in Fig. 2.6(b) and performed DFT-LSDA studies. The three configurations correspond to states with total energy/unit cell of $\frac{1}{4}J_1 + \frac{1}{4}J_2$, $-\frac{1}{4}J_1 - \frac{1}{4}J_2$, and $\frac{1}{4}J_1 - \frac{1}{4}J_2$, respectively. Using the total energy differences from our first-principles calculations under constrained LSDA, we obtain $J_1 = -87meV/\hbar^2$ and $J_2 = -30meV/\hbar^2$, making them parameters for a stronger ferromagnetic (FM) 1D systems compared to what has been achieved before[48]. Since exchange coupling decays exponentially with distance[37], we estimate the second nearest neighbor exchange to be around $-6meV/\hbar^2$ and can be ignored in our model.

Due to thermal fluctuation effects, it is known that there is no long-range magnetic order at finite temperature in 1D structures with isotropic spin interactions, according to the Mermin-Wagner theorem[49]. Thus, the meaningful quantity one should consider is the spin-spin correlation length. As a rough estimate of this quantity, we may use a canonical ensemble of 1D Ising model with partition function:

$$Z = \sum_{\{s_{\alpha i}\}} e^{-\beta H(\{s_{\alpha i}\})} \tag{2.27}$$

The spin-spin correlation length, defined as $a = -R/ln\langle s_{\alpha i} s_{\alpha,i+R}\rangle$, where R is the distance between two spins, can be calculated analytically by treating the spins classically. Evaluating the expectation value and expressing it as a function of the coupling strengths and temperature, we have[50]:

$$a = -\frac{2}{ln(|tanh\beta J_1|) + ln(|tan\beta J_2|)} \tag{2.28}$$

where $\beta = 1/k_B T$. The temperature dependence of the correlation length in this model is plotted in Fig. 2.6(c). At $3K$ (at which low-temperature STM measurements typically are done), the spin correlation length is expected to be at the tens-of-nanometers scale. The strong coupling strength and long correlation length of such designed GNRs should open up applications to spin qubits[51] and spin-dependent transport[52] through nanostructures.

2.6 Stability of the Electronic Structure upon Doping

In practice most GNRs are synthesized on a gold substrate; doping and hybridization/screening effects of gold tend to reduce the magnetic order [38]. We found that, within LSDA at $T = 0$, the FM order remains stable up to a transfer of 1.5 electrons per unit cell into the system. Fig. 2.7 shows the doping dependence of the band structure of the periodic spin chain discussed in the main text. The spin-splitting character of the topological bands is well established up to one electron or one hole doping per unit cell, while the spin-up and spin-down bands start to merge if 1.5 electrons or 1.5 holes per unit cell are doped into the system. As a final remark, we would like to point out that the present classification theory, together with our simple analytic expression for Z of AGNRs, could be applied generally to generate a variety of spin configurations. One could design junctions with arbitrary numbers of coupled localized spin states; and by controlling how the junctions are connected, either FM or AFM coupling between junctions could be realized. The theory may also be applied to other 1D chiral structures, such as the 1D chiral GNRs which could be synthesized[53].

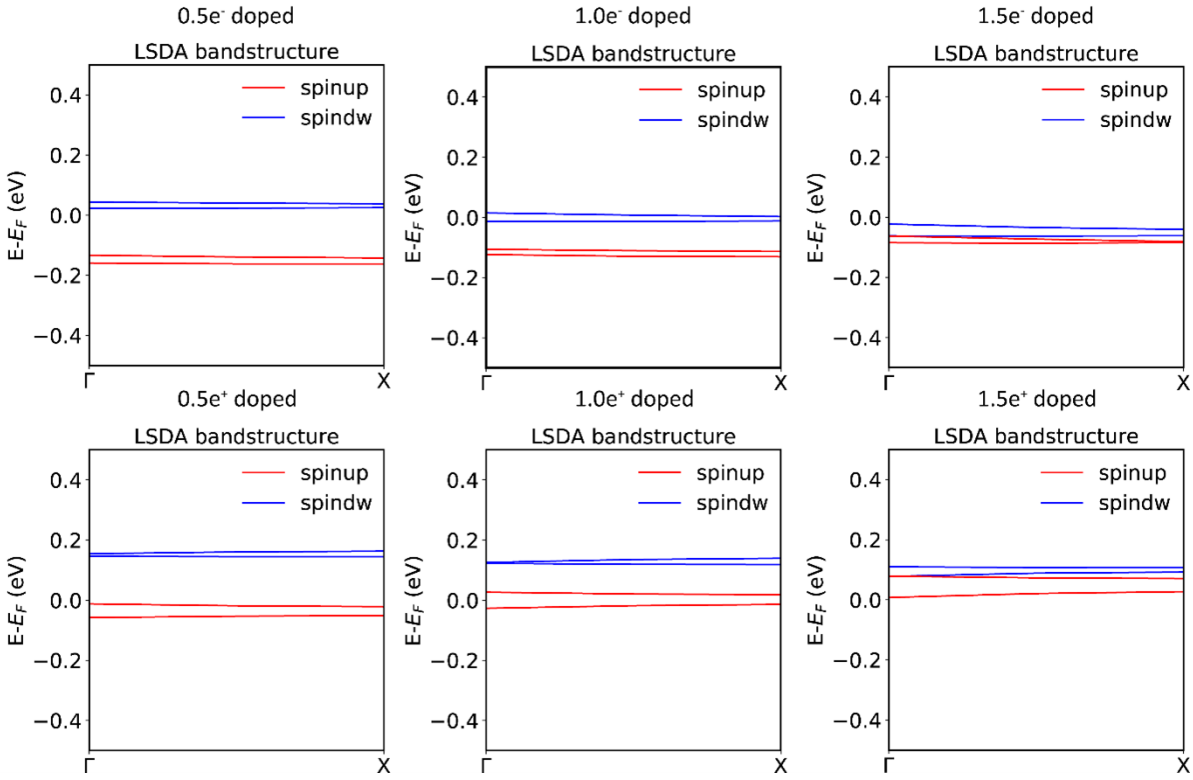

Figure 2.7: The band structure of the in-gap spin-polarized states of a sawtooth AGNR (composed of segments of AGNRs in a superlattice with a periodic spin chain structure) in the DFT-LSDA approximation under different level of doping. The spin-splitting of the bands is seen up to more than one electron or hole doping per unit cell.

Chapter 3

Inducing Metallicity in Graphene Nanoribbons via Zero-Mode Superlattices

In this chapter, we introduce the application of the topological states in graphene nanoribbons in building metallic nanowires. The design and fabrication of robust metallic states in graphene nanoribbons (GNRs) is a significant challenge since lateral quantum confinement and many-electron interactions tend to induce electronic band gaps when graphene is patterned at nanometer length scales. Recent developments in bottom-up synthesis have enabled the design and characterization of atomically-precise GNRs, but strategies for realizing GNR metallicity have been elusive. Here we demonstrate a general technique for inducing metallicity in GNRs by inserting a symmetric superlattice of zero-energy modes into otherwise semiconducting GNRs. We verify the resulting metallicity using scanning tunneling spectroscopy as well as first-principles density-functional theory and tight- binding calculations. Our results reveal that the metallic bandwidth in GNRs can be tuned over a wide range by controlling the overlap of zero-mode wavefunctions through intentional sublattice symmetry-breaking.

3.1 Introduction

Extended two-dimensional (2D) graphene is renowned for being a gapless semimetal, yet when it is laterally confined to nanometer-scale one-dimensional (1D) ribbons a sizable energy gap emerges[35], [36]. Unlike carbon nanotubes (which can exhibit metallicity depending on their chirality), isolated armchair and zigzag graphene nanoribbons (GNRs) always feature a band gap that scales inversely with the width of the ribbon[36]. This is a selling point for GNRs since it makes them attractive as transistor elements for logic devices at the ultimate limits of scalability[54]. But it is also a limitation since metallic GNRs would be valuable as device interconnects and could create new opportunities for exploring novel 1D phenomena such as Luttinger liquids [55][56][57], plasmonics [58]-[59], charge density waves [60][61], and superconductivity[62][63]. Thus far, the finite band gaps of GNRs synthesized using atomically-precise bottom-up fabrication techniques [33]-[34] have been consistent with semi-

conducting theoretical predictions. New opportunities for achieving GNR metallicity arise from emergent topological concepts that allow the placement of topologically-protected junction states at predetermined positions along the GNR backbone[37][64][38][39][44]. These localized states each contribute a single unpaired electron at mid-gap to the electronic structure (i.e., at E = 0) and so judicious placement of such zero-mode states raises the possibility of creating new metallic and magnetic configurations. Thus far, however, only semiconducting GNRs have been fabricated and theoretically studied using this technique[38][39].

3.2 Design 1D Metallic GNRs

Here we demonstrate a general approach for designing and fabricating metallic GNRs using the tools of atomically-precise bottom-up synthesis. This is accomplished by embedding localized zero-mode states in a symmetric superlattice along the backbone of an otherwise semiconducting GNR. Quantum mechanical hopping of electrons between the adjacent zero-mode states results in a metallic band as predicted by elementary tight-binding electronic structure models[65]. Using scanning tunneling spectroscopy (STS) and first-principles theoretical modeling, we find that zero-modes confined to only one of graphene's two sublattices (i.e., sublattice-polarized states) result in narrow-band metallic phases that reside at the border of a magnetic instability. The metallic bandwidth of these GNRs, however, can be increased by more than a factor of 20 by intentionally breaking the GNR bipartite symmetry, thus resulting in robust metallicity. This is accomplished by inducing the formation of just two new carbon-carbon bonds per GNR unit cell (each unit cell contains 94 carbon atoms in the bottom-up synthesized GNRs presented here). This dramatic change in electronic structure from a seemingly minor chemical bond rearrangement arises from the loss of sublattice polarization that accompanies broken bipartite symmetry. This concept provides a useful new tool for controlling GNR metallicity and for tuning GNR electronic structure into new physical regimes.

Our strategy for designing metallic GNRs is based on a simple theorem: if a piece of graphene has a surplus of carbon atoms (ΔN) on sublattice A versus sublattice B, then this results in a minimum of $\Delta N = N_A – N_B$ eigenstates localized on the A sublattice at E = 0 ("zero-modes") that are each occupied by one electron. Here N_A (N_B) is the number of atoms residing on sublattice A (B) This can be derived from 1st nearest neighbor tight-binding model. Within this model, the π-orbitals of carbon atoms of a single-layer graphene-based materials possess a bipartite lattice. The Hamiltonian of a bipartite lattice has chiral symmetry and thus can be written as

$$\hat{H}^{1st} = \begin{pmatrix} 0 & H_{nm}^{\dagger} \\ H_{nm} & 0 \end{pmatrix} \tag{3.1}$$

Where m and n are the number of atoms belonging to the A and B sublattices, respectively, and $N = m + n$ is the total number of atoms in the unit cell. Here we are only considering π orbitals so $\hat{H}^{1st}$ is an $N \times N$ matrix and H_{nm} is an $n \times m$ matrix. For the sGNR, $\Delta N = m - n = 2$ within the unit cell. We want to find the zero-modes of the sGNR

Hamiltonian. This means we need to find eigenvectors ψ_0 satisfying:

$$\begin{pmatrix} 0 & H_{nm}^{\dagger} \\ H_{nm} & 0 \end{pmatrix} \psi_0 = 0 \tag{3.2}$$

ψ_0 can be expressed using an atomic π-orbital basis:

$$\psi_0 = \begin{pmatrix} A_1 \\ . \\ . \\ A_m \\ B_1 \\ . \\ . \\ B_n \end{pmatrix} \tag{3.3}$$

The first m components represent the magnitude of the projection of ψ_0 onto the atomic orbitals belonging to the A sublattice and the remaining n components correspond to the B sublattice amplitudes. Substituting Eq. (3.3) into Eq. (3.2) and setting all n coefficients on the B sublattice basis to zero (i.e. looking for A sublattice-polarized zero-modes), we have:

$$H_{nm} \begin{pmatrix} A_1 \\ . \\ . \\ A_m \end{pmatrix} = 0 \quad for \quad any \quad n \tag{3.4}$$

With m variables and only n constraints ($\Delta N = m - n > 0$), this under-constrained set of homogeneous linear equations must have at least ΔN non-trivial solutions. In other words, there will be at least ΔN completely flat zero-mode bands (ZMBs) at E_F that possess states that are polarized to the A sublattice. This demonstrates that the chiral symmetry of the GNR bipartite lattice can be exploited to produce ΔN sublattice-polarized flat bands by introducing a sublattice imbalance ΔN within the GNR unit cell. For the sGNR, we therefore expect there to be two ZMBs.

Within this framework, second nearest-neighbor hopping acts as a perturbation on the original Hamiltonian (3.1), introducing a small dispersion to the sGNR ZMBs. For the 5-sGNR, the formation of five-membered rings disrupts the bipartite lattice since two carbon atoms from the same sublattice are connected. This can be seen as a perturbation to (3.1) on the order of the first nearest-neighbor hopping, causing a much larger dispersion for the 5-sGNR ZMBs compared to those of the sGNRs.

Expanding this idea to 1D GNR systems with a periodic sublattice imbalance, one can construct a low-energy effective tight-binding model to describe the resulting electronic bands by introducing a parameter, t, that represents electron hopping between adjacent zero-modes. This concept can be used to design metallic GNRs by providing them with a unit cell that contains a surplus of two carbon atoms on sublattice A ($\Delta N = 2$). Under this construction, there are two relevant hopping amplitudes, the intra-cell hopping amplitude (t_1) and the inter-cell hopping amplitude (t_2). A tight-binding analysis of this situation leads to the well-known Su-Schrieffer-Heeger (SSH)[65] dispersion relationship for the zero-mode bands:

$$E_{\pm}(k) = \pm\sqrt{|t_1|^2 + |t_2|^2 + 2|t_1||t_2|cos(k+\delta)} \tag{3.5}$$

where δ is the relative phase between t_1 and t_2 (which in general are complex). Two bands result here since there are two zero-mode states per unit cell and the energy gap between them is $\Delta E = 2||t_1|-|t_2||$. If the two hopping amplitudes are identical, $|t_1| = |t_2|$, then the energy gap is reduced to zero and the resulting 1D electronic structure should be metallic.

Using this idea as a guide for creating metallic GNRs, we designed the GNR precursor molecule 1 (Fig. 3.1(A)). A graphene honeycomb lattice superimposed onto this molecule reveals that under cyclodehydrogenation the methyl group carbon atom attached to the central tetracene (highlighted grey in Fig. 3.1(A)) will fuse and provide one surplus carbon atom on sublattice A over sublattice B per monomer. Previous step-growth polymerizations of structurally related molecules[39] suggest that the surface polymerization of 1 will place the central tetracene unit in an alternating pattern on either side of the GNR growth axis. If polymerization proceeds in a head-to-tail configuration then the resulting GNRs feature two additional carbon atoms on sublattice A per unit cell (Fig. 3.1(A)). Following cyclodehydrogenation the anticipated GNR structure is comprised of short zigzag edges and prominent cove regions (reminiscent of a saw blade) and will herein be referred to as the sawtooth-GNR (sGNR). Based on the symmetry of the sGNR unit cell one anticipates that the hopping amplitudes t_1 and t_2 will be equal (Fig. 3.1(A), red arrows) resulting in a metallic band structure for the sGNR. A caveat to this approach is the limited control over head-to-tail surface polymerization since head-to-head and tail-to-tail polymerizations place the extra carbon atoms on opposite sublattices and are expected to lead to gapped semiconductors.

3.3 STM Measurement and DFT Calculations

In order to experimentally determine GNR metallicity, the electronic structure of sGNRs was characterized using STM spectroscopy. Fig. 3.2(A) shows a typical dI/dV point spectrum obtained on a sGNR (dI/dV spectroscopy provides a measure of the local density of states (LDOS) located beneath the STM tip). Distinctive features associated with valence band (VB) and conduction band (CB) edges can be seen at V = –1.07 ± 0.03 V (State 1) and V = 1.36 ± 0.03 V (State 3), respectively. Most prominent, however, is the sharp peak in LDOS (State 2) that is centered near V = 0 (E_F) (0.02 ± 0.02 V). This peak continuously spans energies both below and above E_F, a clear signature of a gapless, metallic density of states. dI/dV imaging of the wavefunction of these metallic sGNR states shows a characteristic serpentine pattern that snakes back and forth across the sGNR width (Fig. 3.2(B)). The valence and conduction band edge states, in contrast, have their highest intensity along the armchair edges of the GNR (Fig. 3.2(B)), consistent with previous measurements of conventional semiconducting GNRs under similar conditions[66][67]. A similar experimental analysis was also performed on the fused 5-sGNRs as depicted in Fig. 3.3(A). The point spectroscopy of 5-sGNRs was seen to be quite different from that of sGNRs. While features associated with the valence band edge (V = –1.12 ± 0.03 V, State 1) and conduction band edge (V = 1.64 ± 0.09 V, State 3) of 5-sGNRs are observed at similar energies compared to sGNR states, the 5-sGNR spectrum does not feature a central peak at V = 0 (Fig. 3.3(A)). Instead it exhibits a shallow dip at V = 0 and a broad density of states (DOS) feature that spans an energy range above and below E_F. The electronic wavefunctions corresponding to

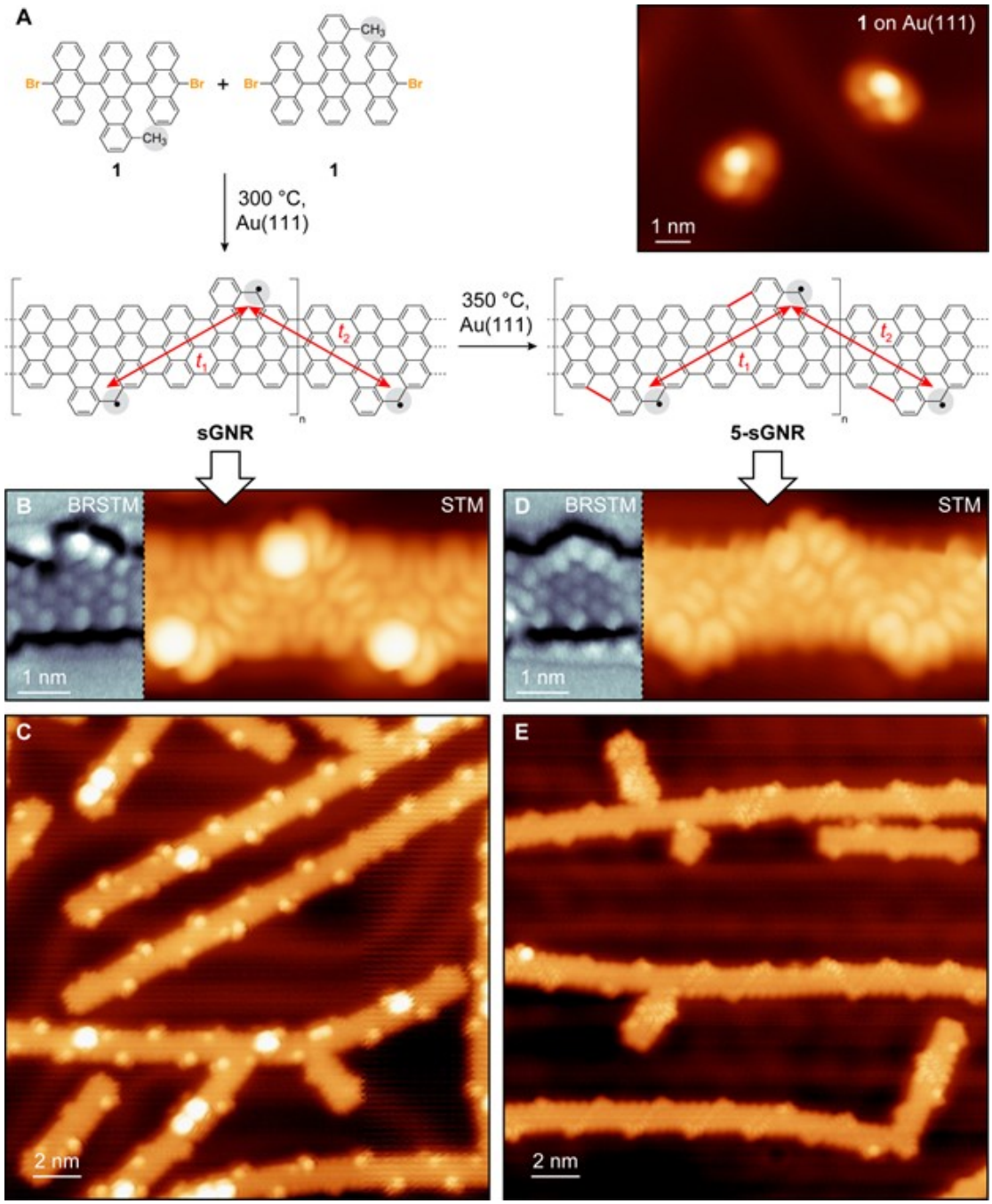

Figure 3.1: Bottom-up synthesis of sawtooth GNRs. (A) Schematic representation of bottom-up growth of both sGNRs and 5-sGNRs from molecular precursor 1. Inset: STM topograph of two isolated monomers of 1 deposited on Au(111). (B) STM topograph of a segment of a sGNR. (C) Larger-scale image of sGNRs. (D) STM topograph of a segment of a 5-sGNR. (E) Large-scale image of 5-sGNRs.

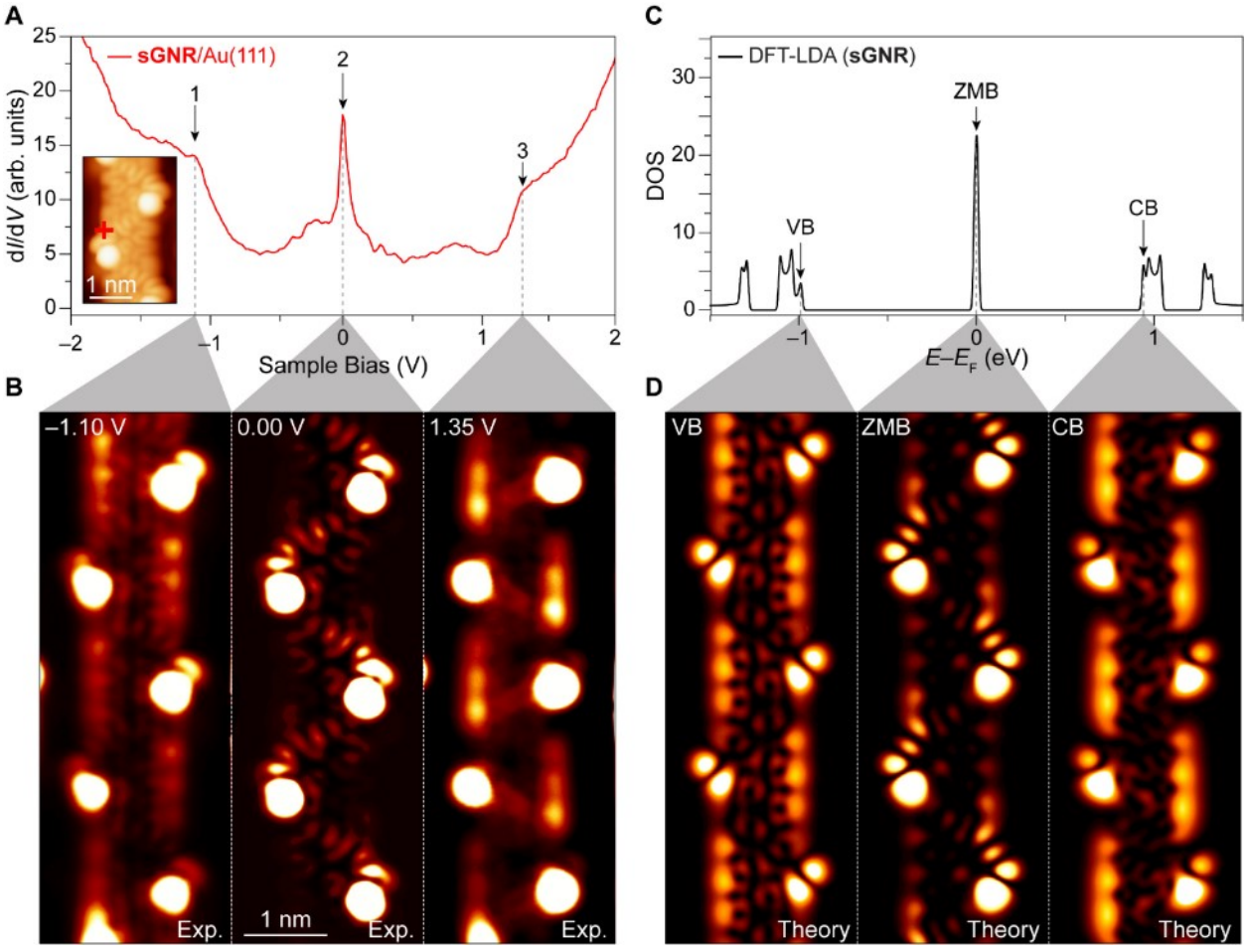

Figure 3.2: Electronic structure of sGNRs. (A) dI/dV point spectroscopy of a sGNR/Au(111) performed at the position shown in the inset (spectroscopy parameter: V_{AC} = 10 mV. Imaging parameters: I_t = 80 pA, V_s = 0.006 V). (B) Constant-height dI/dV maps of 5-sGNRs conducted at the biases indicated in (A) (spectroscopy parameters: V_{AC} = 20 mV for States 1 and 3, V_{AC} = 4 mV for State 2). Constant-height dI/dV maps were subjected to background subtraction of substrate LDOS. (C) DFT-LDA calculated DOS of the sGNR (spectrum broadened by 10 meV Gaussian). Van Hove singularities near E–E_F = 0 are merged because of gaussian smearing. (D) DFT-calculated LDOS of an sGNR at energies shown in (C) (LDOS sampled at a height of 3.5 $\mathring{A}$ above the plane of the sGNR).

States 1-3 in 5-sGNRs are similar to the corresponding features in sGNRs except for the lack of periodic bright spots associated with the non-planar cove edges (Fig. 3.3(B)). For example, dI/dV images performed at biases near the conduction and valence band edges show the LDOS concentrated at the GNR edges while near V = 0 we observe a serpentine pattern (Fig. 3.3(B)) very similar to the metallic state seen in sGNRs. This implies that 5-sGNRs are also metallic and that the LDOS dip observed near V = 0 is not an energy gap but rather a metallic density-of-states feature.

We further explored the apparent metallicity of sGNRs by using ab initio density functional theory (DFT). Fig. 3.4(C) shows the resulting band structure calculated for an isolated sGNR using the local density approximation (LDA). Two narrow bands (denoted zero-mode bands (ZMBs)) are observed bracketing E_F, while CB and VB edges can be seen at much further energies. The two bands bracketing E_F have no bandgap and are fit well by the SSH expression (Eq. 3.5) with $t_1 = t_2 = 5.2meV$ and $\delta = 0$ (Fig. 3.4(C), red dashed lines), and are also stable against Peierls distortion[68] (as confirmed via supercell calculations). The resulting theoretical density of states (Fig. 3.2(C)) shows a single peak centered at E_F as well as VB/CB peaks at lower/higher energies, in good agreement with the STM point spectroscopy for sGNRs (Fig. 3.2(A)). The theoretical wavefunction maps (Fig. 3.2(D)) also match the experimental dI/dV maps obtained at E_F and at the band edge energies, providing further evidence of metallicity in sGNRs.

While our sGNRs clearly match the metallic predictions of the symmetric SSH model, a potential complication is the very narrow metallic sGNR bandwidth (∼21 meV). Metals with high DOS at E_F are often unstable to Mott insulator transitions or magnetic phase transitions as dictated by the Stoner criterion[69][70]. The metallic behavior here may be due to the fact that spin polarization is not accounted for in our simplified tight-binding or LDA-based calculations. To test for this type of magnetic instability in sGNRs, we calculated the sGNR band structure using the local spin density approximation (LSDA) for an isolated sGNR. The result (Fig. 3.5) shows that the sGNR electronic structure does, in fact, undergo a ferromagnetic phase transition which opens a 200 meV energy gap about E_F. We show that the reason we do not see a gap experimentally is due to a combined effect of p-doping and surface electric fields induced by the underlying Au(111) substrate. When these are properly accounted for in our DFT calculation, the gap does, indeed, vanish at the LSDA level, and the metallic result is recovered (Fig. 3.5(D)). Therefore, while it is technically correct to say that sGNR/Au(111) is metallic, our DFT calculation predicts that a significant energy gap will open up and metallicity will be lost due to a magnetic phase transition as soon as this sGNR is removed from the Au(111) surface. While this represents an interesting and potentially useful 1D magnetic phase transition, the question remains whether it is possible to engineer a sGNR with more robust metallicity that would not suffer this fate.

This question can be answered by looking no further than the 5-sGNR whose metallic DOS features are much wider in energy than the narrow peak at E_F seen for sGNRs (Figs. 3.2, 3.3). To clarify the robustness of 5-sGNR metallicity we also analyzed its electronic structure via ab initio DFT calculations. At the LDA level, the 5-sGNR band structure does, indeed, show a much wider metallic band than the corresponding sGNR band structure (Figs. 3.4(C), (D)). When the SSH expression (i.e., the tight-binding result from Eq. 3.5) is fit to the 5-sGNR DFT-LDA band structure, we find a hopping amplitude of $t_1 = t_2 = 480meV$, which corresponds to a bandwidth 23 times larger than the sGNR DFT-LDA bandwidth (Fig.

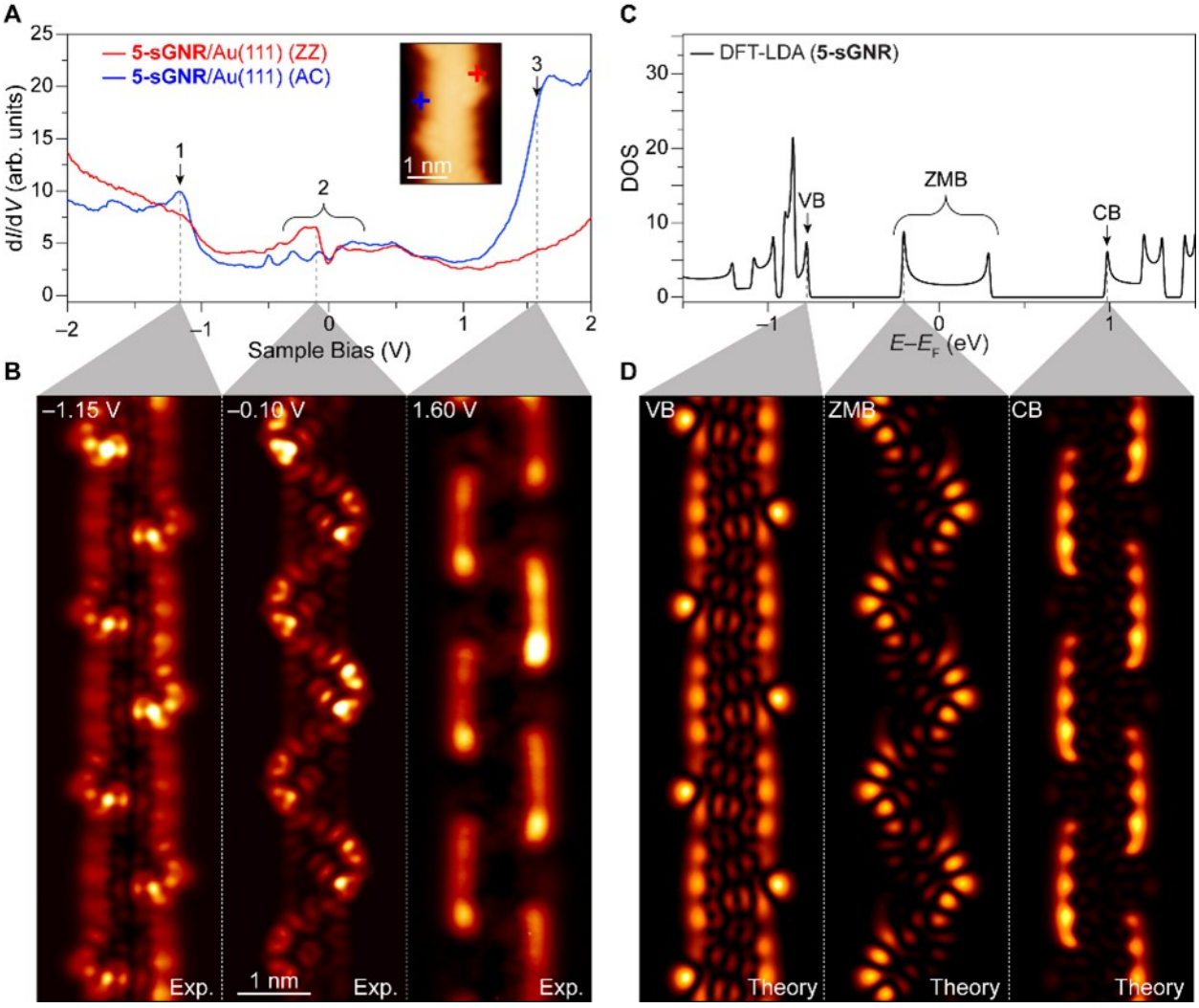

Figure 3.3: Electronic structure of 5-sGNRs. (A) dI/dV point spectroscopy conducted on 5-sGNR/Au(111) at the armchair (blue) and zigzag (red) positions marked in the inset (spectroscopy parameter: V_{AC} = 10 mV. Imaging parameters: I_t = 60 pA, V_s = – 0.100 V). (B) Constant-height dI/dV maps of 5-sGNRs conducted at the biases indicated in (A) (spectroscopy parameter: V_{AC} = 20 mV). Constant-height dI/dV maps were subjected to background subtraction of substrate LDOS. (C) DFT-LDA calculated DOS of the 5-sGNR (spectrum broadened by 10 meV Gaussian). (D) DFT-LDA calculated LDOS of a 5-sGNR at energies shown in (C) (LDOS sampled at a height of 3.5 $\AA$ above the plane of the 5-sGNR).

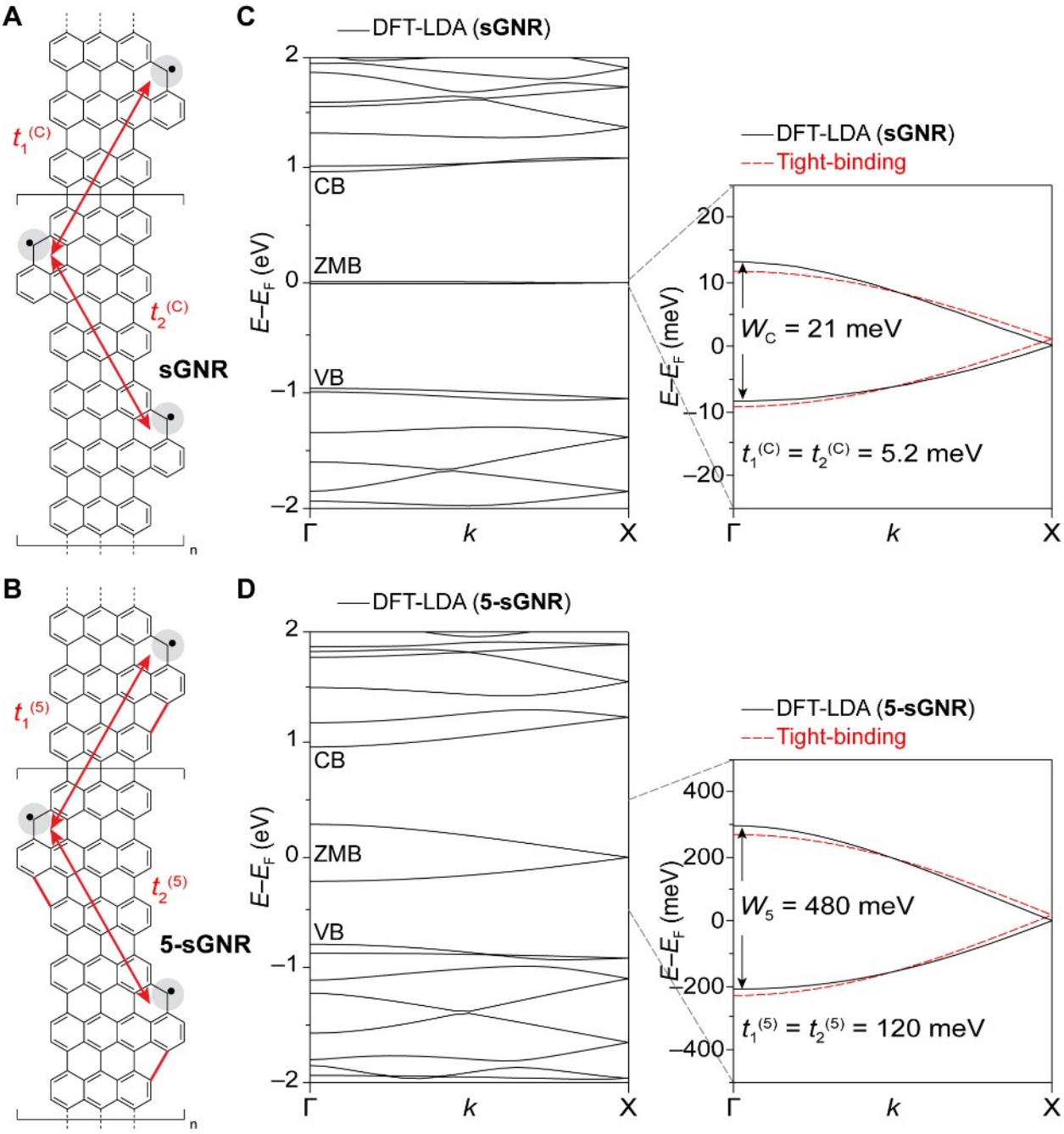

Figure 3.4: Zero-mode band structure. Schematic representation of inter- and intracell hopping between localized zero-modes embedded in (A) sGNRs and (B) 5-CGNRs. (C) Left panel: DFT-LDA calculated band structure for sGNRs. Frontier bands are labelled VB, ZMB, and CB. Right panel: tight-binding fit (red) to DFT-LDA band structure yields hopping parameter $t_1^{(c)} = t_2^{(c)} = 5.2meV$. (D) The same as (C) but for 5-sGNRs. Hopping parameter for 5-sGNR (and corresponding bandwidth) is 23 times larger than for sGNR.

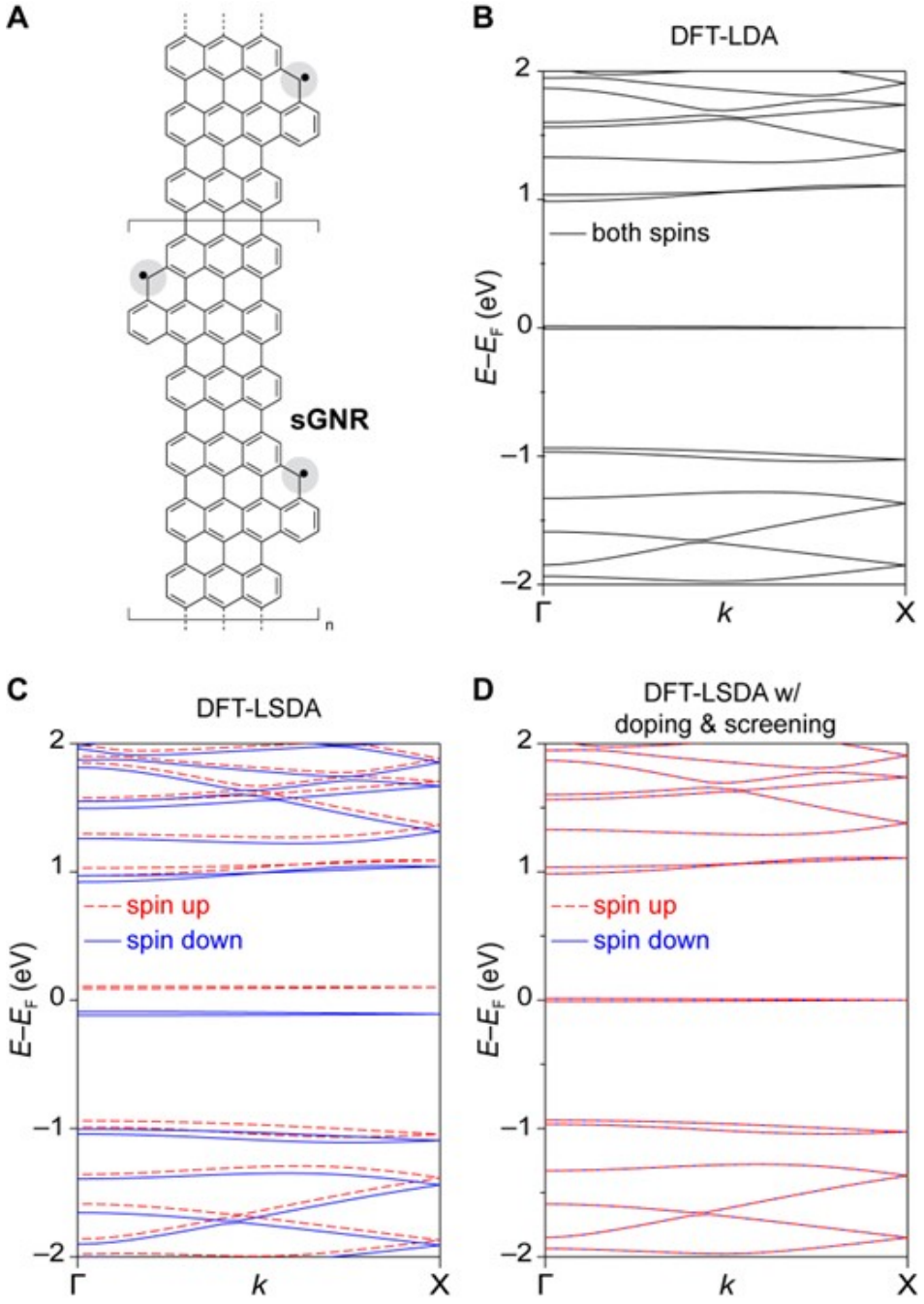

Figure 3.5: DFT Calculations for head-to-tail sGNRs in the local spin-density approximation (LSDA). (A) Sketch of sawtooth GNR structure (sGNR). (B) LDA calculation for free-standing sGNR shows a metallic ground state. (C) LSDA calculation for free-standing sGNR shows a gapped ferromagnetic ground state. (D) The magnetic gap of the sGNR is seen to close when substrate doping and polarization effects are taken into account (the sGNR is assumed to be doped by $\sim 0.4e^+$ / unit cell by the Au).

3.4(D), red dashed lines). This is also reflected in the calculated DOS (Fig. 3.3(C)) which shows a broad U-shaped feature (with peaks characteristic of 1D van Hove singularities), consistent with the experimental dip in LDOS observed at V = 0 for 5-sGNRs (Fig. 3.3(A)). The theoretical LDOS patterns calculated for the 5-sGNR band edge and metallic states (Fig. 3.3(D)) also correspond well to the 5-sGNR experimental dI/dV images (Fig. 3.3(B)). Our DFT calculations of the 5-sGNR at the LSDA level additionally show no signs of magnetism and are identical to the LDA-based results (Fig. 3.6). We conclude that 5-sGNRs exhibit robust metallicity with a much wider bandwidth than sGNRs, both experimentally and theoretically, and are not expected to undergo a magnetic phase transition upon transfer from Au(111) to an insulator.

3.4 The Role of Chiral Symmetry Breaking

The last question that we address is how the seemingly small structural difference between 5-sGNRs and sGNRs leads to such a large difference in their electronic behavior. The dramatic increase in bandwidth observed for 5-sGNRs can be understood as a result of the loss of sublattice polarization of the electron wavefunction induced via the disruption of the graphene bipartite lattice symmetry due to the new five-membered ring bonds (which bridge what were previously open coves). This can be understood by remembering that the two extra atoms added to the sGNR unit cell on sublattice A result in two new $E = 0$ eigenstates (zero modes) per unit cell whose wavefunctions are also confined to sublattice A. This sublattice polarization is preserved in the sGNR Bloch waves for the two in-gap bands (Fig. 3.7(B)), and the sGNR bandwidth is determined by the effective amplitude (t_{eff}) for an electron to hop between adjacent zero-modes (Fig. 3.7(A)). Because the zero-modes are all on the same sublattice it can be shown that $t_{eff} \propto t'$ where t' is the second-nearest-neighbor hopping amplitude of graphene (since there is no zero-mode state density on sublattice B). In the case of 5-sGNRs, however, the bipartite lattice is disrupted by the bond that closes the coves; the zero-modes are thus no longer sublattice polarized (Fig. 3.8). Consequently, the resulting Bloch waves are no longer sublattice polarized (i.e., both sublattices now exhibit state density (Fig. 3.7(C)) and so $t_{eff} \propto t$ where t is the nearest-neighbor hopping amplitude of graphene (Fig. 3.7(A)). To explicitly show this, we model the frontier band structure formed by a zero-mode superlattice using an effective two-band tight-binding model. By expressing the new effective hopping between local zero-modes in terms of the graphene hopping parameters, we show that sublattice polarization and mixing of zero-mode wavefunctions leads to narrow and dispersive zero-mode bands, respectively.

As discussed above, the DFT-calculated ZMBs for both the sGNR and the 5-sGNR are well-captured using a simple two-band tight-binding model. With two zero-modes per unit cell, the resulting dispersion relation can be expressed in terms of complex-valued inter- and intracell hopping terms t_1 and t_2 and their relative phase δ (Eq. 3.5). For both GNRs presented in the text, t_1 and t_2 are equal in magnitude and real-valued so $\delta = 0$. The resulting ZMB bandwidth W is proportional to the effective hopping $t_1 = t_2 = t_{eff}$ between the two zero-modes within the GNR unit cell, ψ_0^1 and ψ_0^2. These two states can be expressed

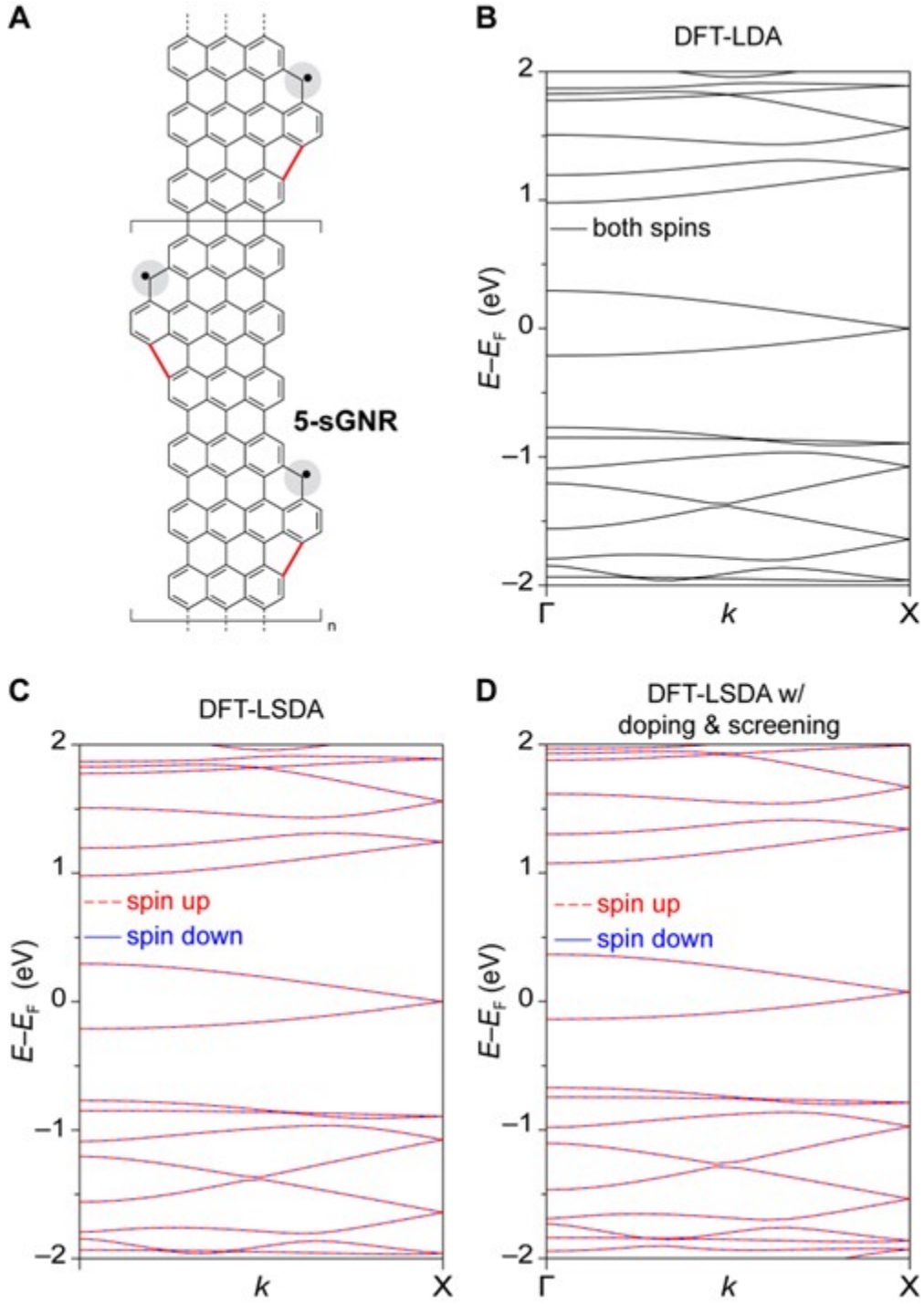

Figure 3.6: DFT Calculations of metallic 5-sGNRs in the local spin-density approximation (LSDA). (A) Sketch of head-to-tail 5-sawtooth GNR structure (5-sGNR). (B) LDA calculation for free-standing 5-sGNR shows a metallic ground state. (C) LSDA calculation for free-standing 5-sGNR shows a non-magnetic metallic ground state. (D) LSDA calculations of the 5-sGNR band structure when substrate doping and polarization effects are taken into account (the sGNR is assumed to be doped by $\sim 0.4e^+$ / unit cell by the Au). The 5-sGNR band structure is essentially unaffected by substrate doping and screening.

as linear combinations of atomic π-orbitals $\phi_{\pi,i}$ within the GNR unit cell:

$$\psi_0^1 = \sum_{i=1}^{m} a_i^1 \phi_{\pi,A_i} + \sum_{i=1}^{n} b_i^1 \phi_{\pi,B_i} \tag{3.6}$$

$$\psi_0^2 = \sum_{j=1}^{m} a_j^2 \phi_{\pi,A_j} + \sum_{j=1}^{n} b_j^2 \phi_{\pi,B_j} \tag{3.7}$$

Where we have explicitly broken summations into its A and B sublattice components for clarity. The effective hopping between these states can be expressed in terms of the GNR Hamiltonian H:

$$t_{eff} = \langle \psi_0^1 | H | \psi_0^2 \rangle \tag{3.8}$$

Combining Eq. 3.6 and Eq. 3.7 with Eq. 3.8, we get:

$$t_{eff} = \sum_{i,j;AtoB} a_i^1 b_j^2 t_{ij}^{AB} + \sum_{i,j;BtoA} b_i^1 a_j^2 t_{ij}^{BA} + \sum_{i,j;bothA} a_i^1 a_j^2 t_{ij}^{AA} + \sum_{i,j;bothB} b_i^1 b_j^2 t_{ij}^{BB} \tag{3.9}$$

For brevity's sake we have used t_{ij} to represent the hopping between atomic orbitals lying on the ith and jth lattice site within the GNR unit cell:

$$t_{ij}^{SS'} = \langle \phi_{\pi,S_i} | H | \phi_{\pi,S'_j} \rangle \tag{3.10}$$

Where S and S' can be substituted by A or B and indicate the sublattice on which i and j lie. We note that the first two terms in Eq. 3.9 account for hopping between orbital components of ψ_0^1 and ψ_0^2 on different sublattices, while the second two terms account for hopping on the same sublattice. Given that ψ_0^1 and ψ_0^2 lie on a bipartite lattice, the lowest order t_{ij} for the first two terms is t (the nearest-neighbor hopping of graphene), while that of the second two terms is t' (the second nearest-neighbor hopping of graphene). Here, we set the onsite energy of π-orbitals to zero. Writing this explicitly, we find:

$$t_{eff} = t \left(\sum_{i,j}^{1st\ n.n.} a_i^1 b_j^2 + \sum_{i,j}^{1st\ n.n} b_i^1 a_j^2 \right) + t' \left(\sum_{i,j}^{2nd\ n.n} a_i^1 a_j^2 + \sum_{i,j}^{2nd\ n.n} b_i^1 b_j^2 \right) + O(3rd\ n.n.) \tag{3.11}$$

The form of Eq. 3.11 is convenient because it expresses the effective hopping between two graphene-supported zero-modes in terms of the lowest-order graphene hopping parameters t and t'. It also shows that if ψ_0^1 and ψ_0^2 are both polarized on the same sublattice (both A or both B), then the effective hopping between the two states will be less than the second nearest-neighbor hopping of graphene, t' (i.e. the nearest-neighbor hopping terms will be exactly zero). On the other hand, if ψ_0^1 and ψ_0^2 are either polarized on opposite sublattices (one on A and one on B) or are both sublattice-mixed (both on A and B), then the effective hopping will be constrained by the first nearest-neighbor hopping of graphene, t.

This reveals the mechanism by which the zero-mode hopping (re: bandwidth) was increased by more than an order of magnitude between the sGNR and 5-sGNR. The prior is composed entirely of zero-modes polarized on the same sublattice, whereas those of the latter are sublattice mixed as a result of the pentagonal bond closure (Fig. 3.8). Hence,

the effective hopping in the sGNR is constrained by the second nearest-neighbor hopping of graphene, while that of the 5-sGNR is constrained by the first nearest-neighbor hopping of graphene.

This explanation is consistent with the ratio of the bandwidths of the two GNRs (~ 23) which falls within the range of accepted values for t/t'[71]. The key insight here is that the loss of sublattice polarization (i.e., through intentional fusion of five-membered rings along the cove edges) greatly increases the effective overlap of adjacent localized zero-mode states and strongly enhances the metallic bandwidths. This provides a useful new design criterion for engineering robust metallic systems from zero-mode superlattices in carbon networks.

3.5 Head to Head Structure and Topology

Besides to head to tail connections analyzed in details. It is also possible to see head to head, or tail to tail structures. These structures turn out to be insulators with nontrivial topology. The DFT-LSDA, and DFT-LDA bandstructures are shown in Fig. 3.9. A tight-binding model is fitted to the DFT bandstructure as well. This structure yields insulators that give potential topology characterized by Z_2 index. We calculate Z_2 index for this particular structure. The result shows $Z_2 = 1$ when the tail to tail unit cell is chosen, and $Z_2 = 0$ when the head to head unit cell is chosen. This theoretical prediction is further confirmed by STM measurement on a head-to-head/tail-to-tail junction (Fig. 3.10), the topological junction state is measured at near-zero bias, consistent with the theoretical prediction.

3.6 Conclusion

In conclusion, we have successfully demonstrated the ability to rationally design 1D metallic GNRs by embedding symmetric zero-mode superlattices into otherwise semiconducting GNR backbones. Our results provide a general strategy for introducing zero-modes into graphene-based materials, and also reveal the hidden role of sublattice polarization in controlling the emergent band structure of these systems. This general approach provides new opportunities for creating nanoscale electrical devices, and for exploring novel electronic and magnetic phenomena in a new class of 1D metallic systems.

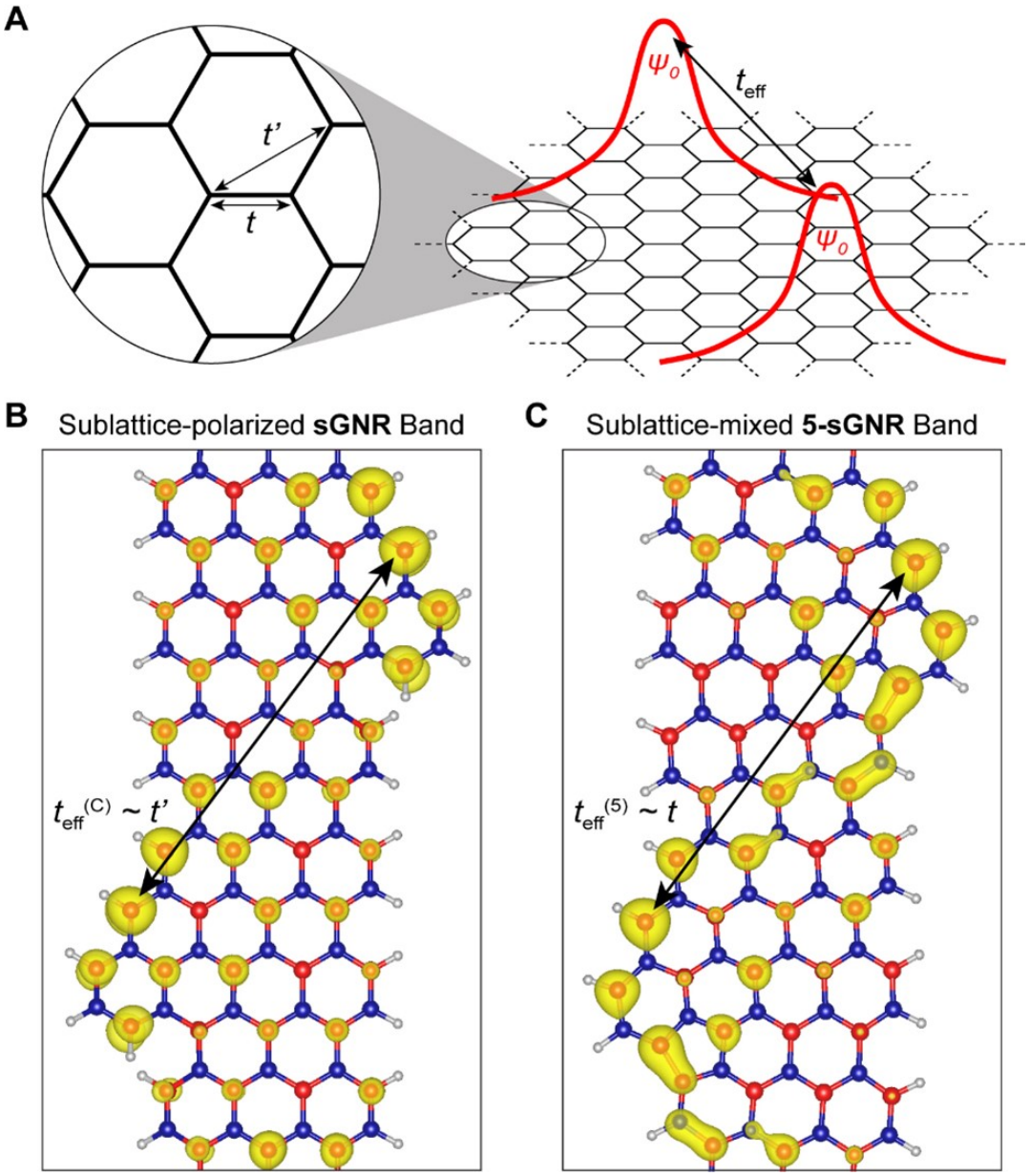

Figure 3.7: Zero-mode engineering in GNRs. (A) Diagram of effective hopping t_{eff} between two localized states (labeled Ψ_0) embedded in graphene. Inset: schematic representation of the first (t) and second (t') nearest-neighbor hopping parameters of graphene. (B) DFT-calculated wavefunction 5% density isosurface of a sGNR for states near $E = 0$. (C) Same for 5-sGNRs. Different sublattices are denoted with different colors (A sublattice in red and B sublattice in blue). The sGNR wavefunction is completely sublattice polarized, while the 5-sGNR wavefunction is sublattice mixed and more delocalized.

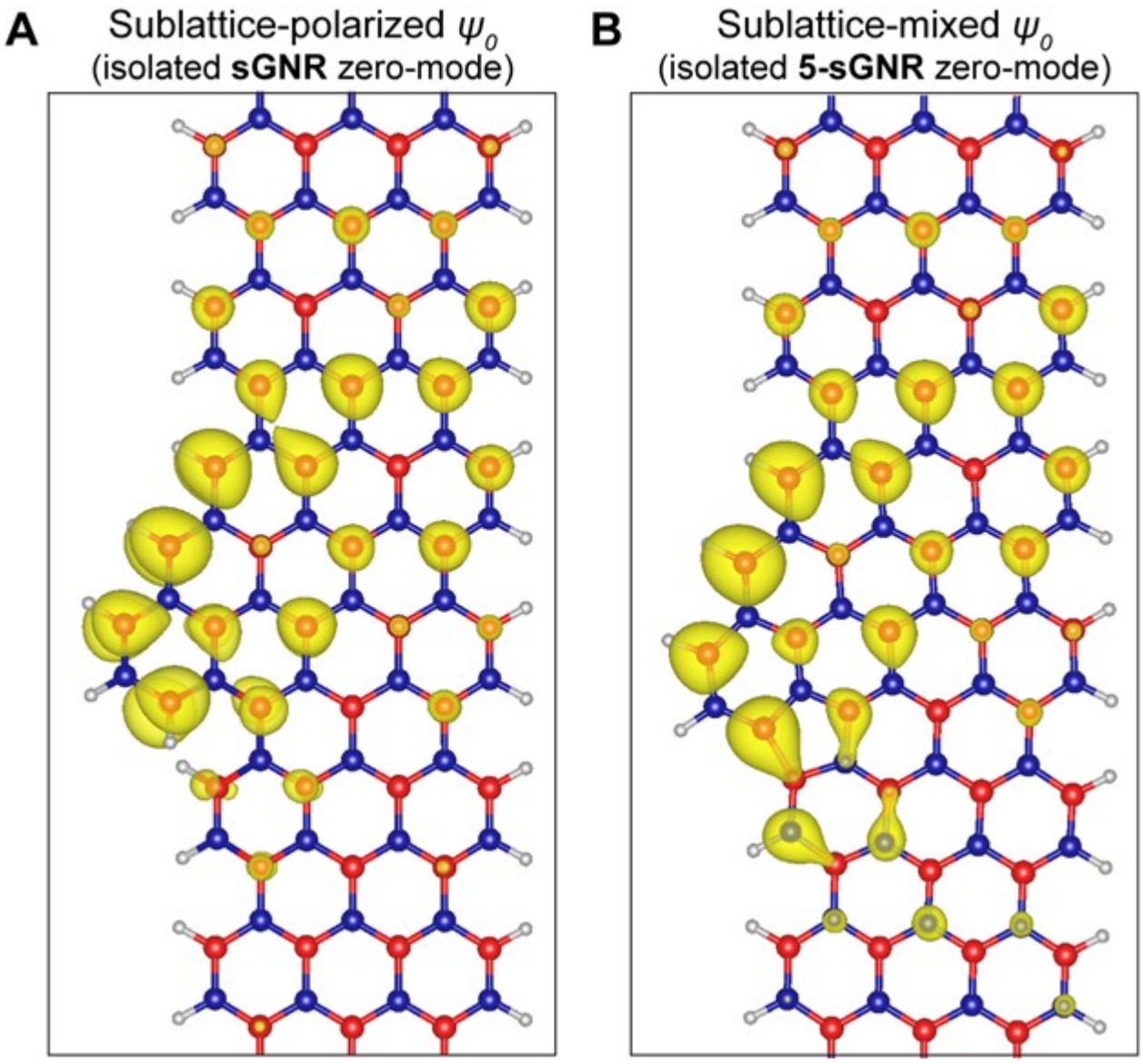

Figure 3.8: Sublattice polarization/mixing of GNR zero-modes. (A) DFT calculated 3% charge density isosurfaces of a structure exhibiting an isolated zero-mode (the purpose of this is to provide insight into the sublattice polarization of sGNR zero-mode bands (ZMBs)). Different sublattices are denoted with different colors (A sublattice is red, B sublattice is blue). The sGNR structure leads to a sublattice-polarized zero-mode since the intact cove preserves bipartite lattice symmetry. (B) Same as (A), but for an isolated 5-sGNR zero-mode. Here there is no sublattice polarization of the zero-mode since the bipartite lattice symmetry is broken by the pentagonal ring.

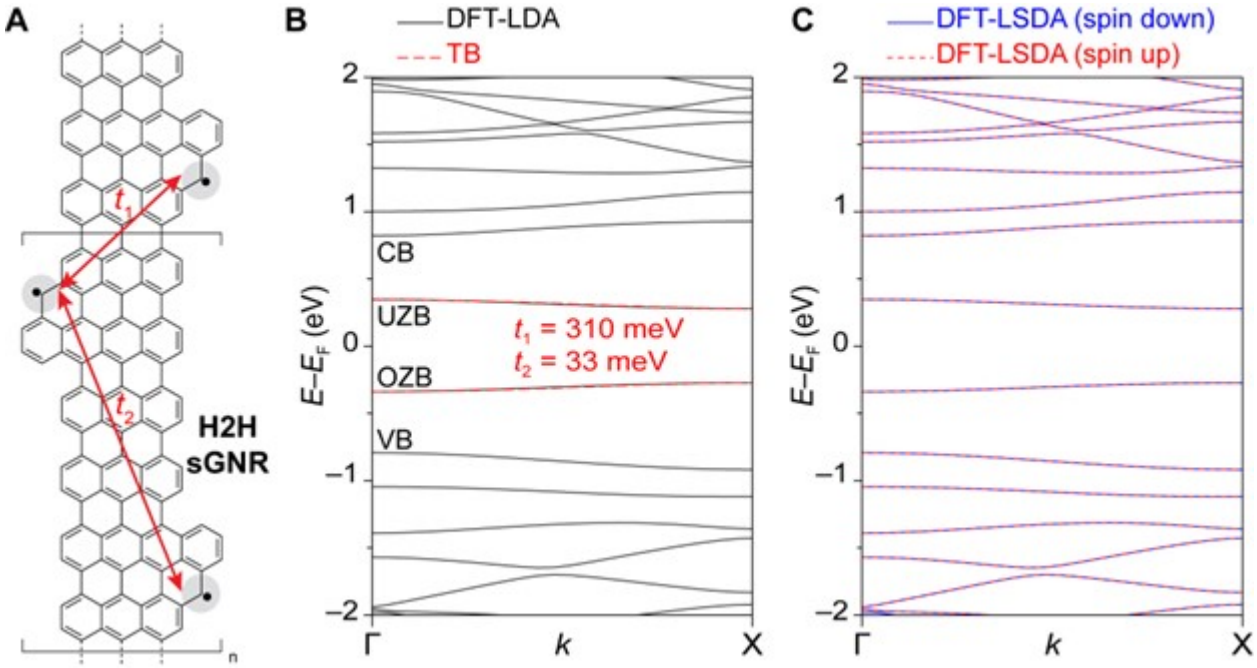

Figure 3.9: Theoretical electronic structure of head-to-head sGNR. (A) Schematic representation of inter- and intracell hopping between localized zero-modes embedded in head-to-head sGNRs. (B) DFT-LDA calculated band structure for head-to-head sGNRs (black) overlaid with a tight-binding fit (red) to the OZB/UZB bands (the tight-binding fit yields hopping parameters $t_1 = 310meV$ and $t_2 = 33meV$). (C) DFT-LSDA calculated band structure for head-to-head sGNRs shows a non-magnetic ground state. Lieb's theorem raises the possibility of antiferromagnetism, but the relatively large overlap between adjacent zero-modes pushes this GNR into a non-magnetic ground state.

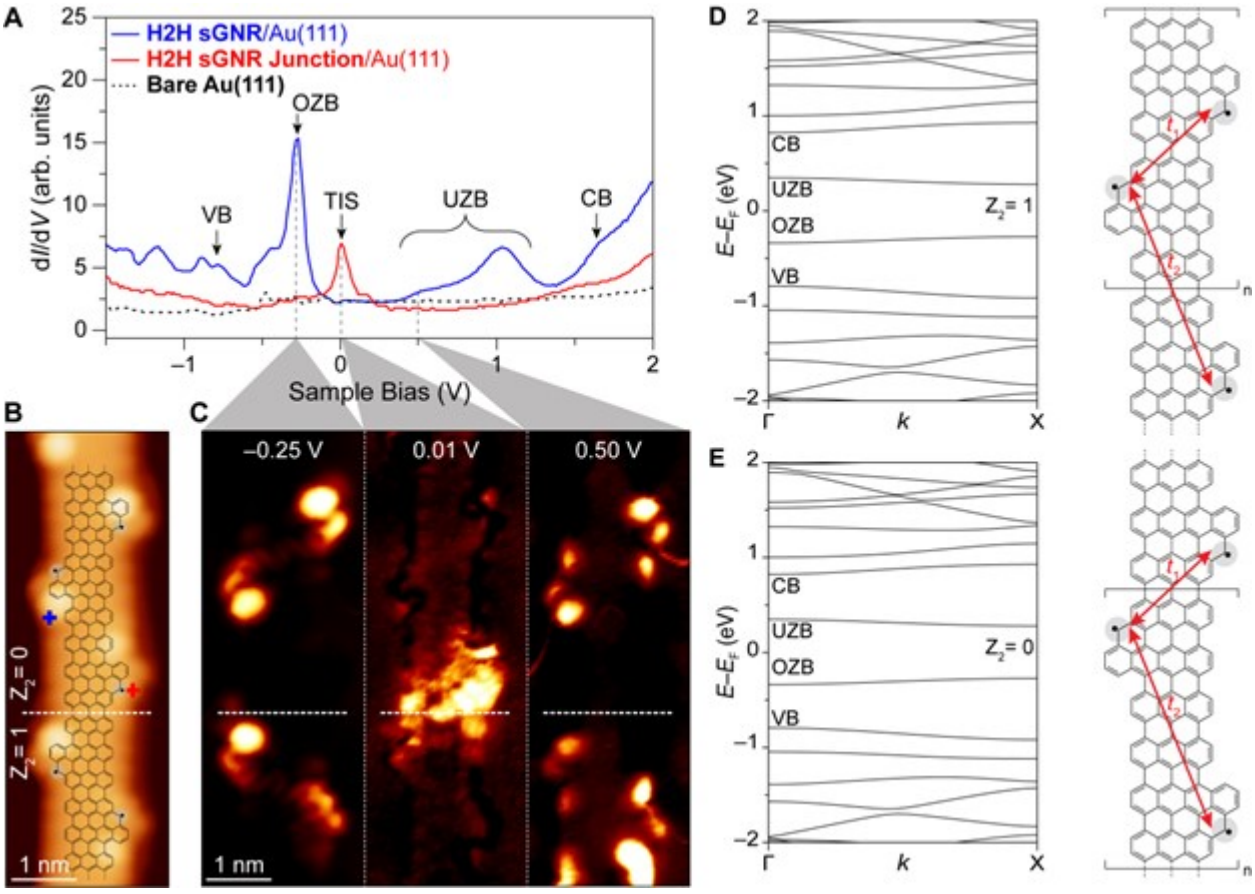

Figure 3.10: Electronic structure of head-to-head sGNR topological homojunction. (A) dI/dV point spectroscopy performed on bare gold (dotted black curve) and on a head-to-head sGNR topological homojunction in the bulk (blue curve) and at the junction interface (red curve) as marked in (B). (B) Topographic image of head-to-head sGNR topological homojunction overlaid with the corresponding chemical structure (I_t = 150 pA, V_s = –1.10 V). The topological invariant Z_2 on either side of the junction (dotted white line) is indicated based on the terminating unit cells shown in (D) and (E). (C) Constant-current dI/dV maps of a head-to-head sGNR topological homojunction conducted at the biases indicated in (A) (I_t = 150 pA, V_{AC} = 10 mV for OZB and UZM maps and I_t = 80 pA, V_{AC} = 10 mV for the topological interface state (TIS) map). (D) Band structure of the indicated head-to-head sGNR for nontrivial topology (as determined by the unit cell commensurate with the GNR terminus) and for (E) trivial topology (as determined by a different unit cell). The Z_2 invariants associated with each unit cell are labelled in the corresponding band structures, showing that the UZB/OZB gap should host a TIS, as confirmed experimentally in (A).

Chapter 4

Rationally-Designed Topological Quantum Dots in Bottom-up Graphene Nanoribbons

In this chapter, we show that the topological states could be utilized to form 1D topological quantum dots. The topological control was achieved through the synthesis and on-surface assembly of three distinct molecular precursors designed to exhibit structurally-derived topological electronic states. We perform DFT and tight-binding (TB) calculations, revealing that the magnitude and sign of orbital hopping between topological zero-mode states can be tuned based on the bonding geometry of the interconnecting region. Using a combination of low-temperature scanning tunneling microscopy and spectroscopy (STM/STS), we have characterized two GNR topological quantum dot (TQD) arrangements synthesized under ultrahigh vacuum (UHV) conditions. The STM measurement agrees with theoretical calculations. These results demonstrate the utility of topological zero modes as building blocks for designer quantum dots that promise new functionality for future advanced electronic devices.

4.1 Introduction

The advent of atomically-precise bottom-up growth of graphene nanoribbons (GNRs)[72] has enabled realization of numerous well-defined GNR structures possessing a wide range of material and electronic properties originating from the rational design of molecular precursors. For example, this approach has been broadly applied to successfully synthesize tailored GNRs with a variety of widths,[33][34][73] edge structures,[74][53][75] and heteroatom dopants[76][77]-[78] at the atomic scale. Multiple synthetic strategies for achieving GNR heterostructures from monomeric precursors have been demonstrated, including the introduction of ancillary chemical reactions to GNRs derived from a single molecular precursor[79][80][81]-[82] and copolymerization of distinct but chemically compatible precursor monomers.[39][67][83]-[84] GNR heterostructures have also been exploited to create quantum dots[67][85][86][87] that possess electronic structures dependent on the size and shape of constituent GNR segments (i.e., where the behavior is determined by randomly

connected segments of arbitrary length). Hierarchical growth[88] and sterically-enforced selective co-polymerization[38], on the other hand, represent viable routes for creating deterministic GNR quantum dots, but have not yet been explored in this context.

The discovery of distinct topological phases[37] in the GNRs and new experimental[38][39] and theoretical[1][37][64][44] developments in engineering GNR topology have recently prompted a paradigm shift in the design and fabrication of GNR electronic structure. From this perspective, every periodic GNR structure possesses an invariant topological classification that is characteristic of its terminating unit cell and associated symmetries (e.g., a Z_2 invariant for time reversal and spatial symmetries[37][64][44] and a Z invariant for chiral symmetry[1]). The bulk-boundary correspondence principle then dictates that an interface between two GNRs possessing different topological invariants will host a topological zero mode: a symmetry-protected state that lies energetically at or near midgap and may be associated with a localized spin under suitable conditions[37][1][89]. The creation and controlled hybridization of neighboring zero modes[37] has been validated as a viable strategy for experimentally realizing small-gap semiconducting [38][39]and metallic[2] GNRs, as well as nanoporous graphene[4] wherein the frontier electronic structure is composed of topological zero-mode bands. By extension, isolated topological zero modes should provide a well-defined basis for realizing topological quantum dots (TQDs) embedded in extended GNR structures that are potentially suitable for applications such as tunneling field-effect transistors.[90]

Here we report the deterministic growth and electronic structure characterization of GNR quantum dots composed of pairs of topological zero-mode states that appear at the interfaces between seven- and nine-atom-wide armchair GNRs (7-AGNRs and 9-AGNRs, respectively) as predicted theoretically in ref. [37]. We make novel use of a bifunctional molecular linker previously used to generate 7/9-AGNR superlattices[38] and discover that it is synthetically compatible with specific 7- and 9-AGNRs precursors. The latter 9-AGNR precursor was specifically designed for this study to permit viable copolymerization with the bifunctional linker into ordered nanostructures. The resulting GNRs are characterized by pristine segments of 7- and 9-AGNRs connected by a well-defined interface. These reproducible heterojunctions are separated by a fixed distance ensuring the creation of topological zero modes that hybridize across short AGNR segments with predetermined electron hopping amplitudes. Since the low-energy spectra of quantum dots defined by coupled zero modes is ultimately determined by this hopping amplitude, all TQDs synthesized through this reproducible methodology possess the same electronic structure, in contrast to the random GNR quantum dot structures realized previously through nondeterministic synthetic approaches[85][67]. Experimental characterization of two varieties of GNR TQDs using scanning tunneling microscopy and spectroscopy (STM/STS) reveal a systematic dependence of the TQD zero-mode splitting on the width of the intermediate GNR segment. These results are supported by first-principles DFT and TB calculations which provide additional insight into the physical origins of the magnitude and sign of the hopping terms that encode the energetic splitting and wavefunction character of the topological quantum dot states. These results provide groundwork for achieving magnetic spin centers with deterministic coupling using similar synthetic approaches.

4.2 Comparison of Theoretical and Experimental Results

Our design for GNR quantum dots is based on a topologically nontrivial junction[37] that enables controlled bridging between 7-AGNR and 9-AGNR segments. To achieve this, we selected interfacial unit cells for the adjacent GNR segments that correspond to different topological classifications. The two unit cells are based on the zigzag' (for 7-AGNRs) and zigzag (for 9-AGNRs) terminating unit cells,[37] which both possess mirror and inversion symmetry and can therefore be classified with a Z_2 invariant (Fig. 4.1(A)). In addition to the Z_2 classification scheme, the approximate chiral symmetry of all periodic graphene-based materials also permits assignment of a Z invariant to these structures[1] (also shown in Fig. 4.1(A)). While a difference in the value of Z_2 across an interface in one-dimension (1D) indicates the presence of an odd number of topological interface states, a difference in Z provides the exact number of such interface states. As seen in Fig. 4.1(A), predictions based on both of these topological classification schemes are consistent with one zero-mode state at the interface of the 7-AGNR and 9-AGNR unit cells whose structure is shown in Fig. 4.1.

In order to generate the specific 7/9-AGNR interface that is predicted to give rise to this zero-mode state[1][37] (Fig. 4.1(C),(D)), we employed a stepwise synthesis based on the co-deposition of the bifunctional linker with either monomer for 7- or 9-ANGRs on a Au(111) surface under ultrahigh vacuum (UHV) conditions (Fig. 4.1(B). In the first step, dilute quantities of the bifunctional linker 2 are deposited onto a clean Au(111) surface along with an excess of either precursor 1 or 3 (which constitute the 7- and 9-AGNR bulk, respectively). During radical step-growth polymerization of these mixtures, polymerization of bulk 7- or 9-AGNR precursors is the dominant process since they are present in much higher quantities than the bifunctional linker. Concurrently, dilute quantities of the bifunctional molecular linker 2 co-deposited on the same surface dimerize. If we designate the side featuring the bromoanthracene group as the A side of the bifunctional linker and the bromobiphenyl group the B side, then the dimerization of 2 can lead to two possible structures featuring an AB–BA bond (dimers are linked by the biphenyl groups) or a BA–AB bond (dimers are linked by the bromoanthracene groups). The unreacted ends of these dimers can continue to bond with bulk 7- or 9-AGNR proto-polymer segments (Fig. 4.1(B)), respectively. Further annealing results in fully graphenized pairs of GNR topological interfaces, where monomer 1 (3) bonds with the AB–BA (BA–AB) dimers to yield extended 7-AGNR (9-AGNR) segments interrupted by a segment of three 9-AGNR (7-AGNR) unit cells (Fig. 4.1(C),(D)). We refer to these structures as 7/9/7 and 9/7/9 TQDs, respectively. While the syntheses and on-surface polymerization of precursors 1 and 2 have been reported previously,[72][38] molecular precursor 3 was designed specifically for this study.

STM topographic images of both 7/9/7 TQDs (Fig. 4.1(C)) and 9/7/9 TQDs (Fig. 4.1(D)) show characteristic width modulations along the GNR axis consistent with short segments of three-unit-cells of either 9-AGNR (in the case the 7/9/7 TQD) or 7-AGNR (in the case of the 9/7/9 TQD).

In order to probe the electronic properties of GNR TQDs, we performed STS point spectroscopy measurements and differential conductance (dI/dV) mapping on both types of GNR TQDs. These measurements directly probe the energy- and spatial-dependence

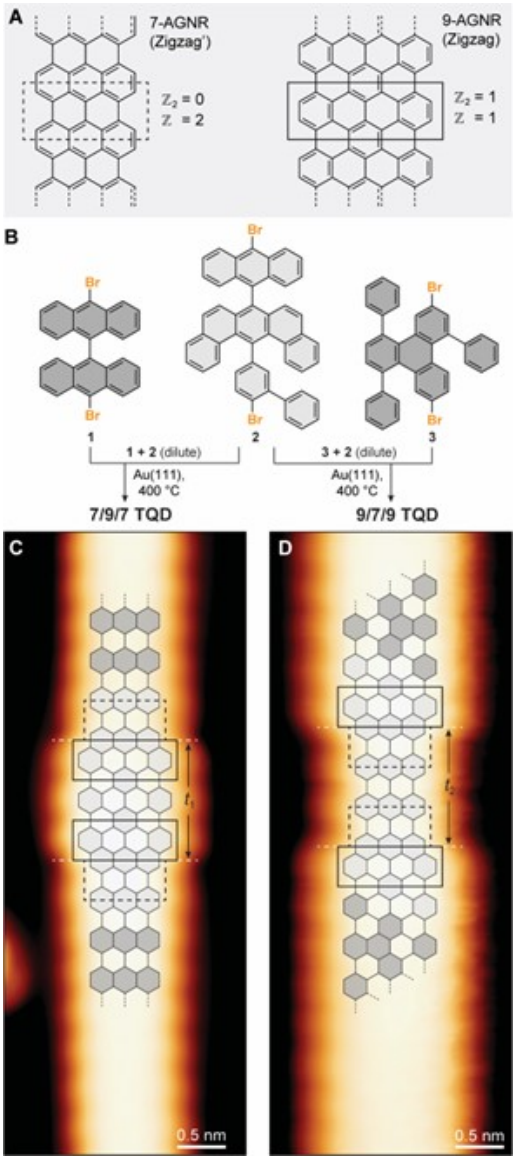

Figure 4.1: On-surface synthesis of AGNR topological quantum dots. (A) The topological invariants Z_2 and Z for the depicted AGNRs are determined by the terminating unit cell with mirror/inversion symmetry and chiral symmetry, respectively. The zigzag' termination of 7-AGNRs (dashed box, left panel) possesses topological invariants $Z_2 = 0$ and $Z = 2$, while the zigzag termination of 9-AGNRs (solid box, right panel) possesses topological invariants $Z_2 = 1$ and $Z = 1$. Crossing an interface as depicted by the structure in (C) and (D) between these two unit cells corresponds to a change in both topological invariants. Therefore, such an interface is expected to host one topological zero-mode state. (B) Molecular precursors 1 and 3 generate extended sections of 7-AGNRs and 9-AGNRs, respectively. (C) The structures of the 7/9/7 and (D) 9/7/9 topological quantum dots superimposed on the corresponding STM topographic images.

of the local density of states (LDOS) of each GNR structure. Fig. 4.2(A) shows that point spectra collected on the bulk 7-AGNR segment of 7/9/7 TQDs exhibit two prominent features at –0.8 V and 1.6 V (features 1 and 4; red curve) that are consistent with previously reported STS measurements of the valence and conduction band edges of pure 7-AGNRs.[66] In contrast, point spectra collected in the 7/9/7 TQD junction region show two low-energy states at –0.1 V and 0.6 V (features 2 and 3; blue curve) that appear within the bulk 7-AGNR energy gap. dI/dV maps collected at the energies associated with these features demonstrate that states at 1 and 4 are localized mainly on the bulk 7-AGNR segments while states at 2 and 3 are localized to the 7/9-AGNR junction (Fig. 4.2(B)). The LDOS for the lower energy state 2 shows a uniform high intensity throughout the short 9-AGNR segment (i.e., an antinode) linking the two topological interface states, while state 3 shows a diminished intensity in the same region (i.e., a node). The energetic alignment and spatial characteristics of states 2 and 3 suggest that they arise from hybridization between the two topological junction states. Simple quantum mechanical reasoning implies that the magnitude of the splitting between states 2 and 3 (E_{g1}) yields an experimental measure of the electron hopping amplitude (t_1) between the two topological junction states across the 9-AGNR segment: $E_{g1} = |2t_1| = 0.7eV$.

We performed analogous STS measurements on a 9/7/9 TQD, which features the same 7/9 topological junctions as the 7/9/7 TQD, but with an inverted geometry (i.e. hybridization across a 7-AGNR segment). As before, four features can be observed in the point spectroscopy (features 5–8 in Fig. 4.3A). States associated with features 5 and 8 are most prominent when the STM tip is placed above the bulk 9-AGNR segment (red curve), while states at 6 and 7 only appear in spectra collected in the region of the 7/9-AGNR junctions (blue curve). The energy gap between states 5 and 8 is consistent with previous STS measurements of pristine 9-AGNRs2, and dI/dV maps obtained at these energies show LDOS predominantly localized to the bulk 9-AGNR segments (Fig. 4.3B). Conversely, dI/dV maps obtained at biases associated with in-gap states at 6 and 7 show localization to the 7/9-AGNR junction regions (Fig. 4.3(B)), suggesting that states at 6 and 7 are associated with topological zero modes coupling through the short 7-AGNR segment. In this case, the lower energy state 6 features a node across the 7-AGNR segment while the higher energy state 7 shows the characteristics spatial LDOS associated with an antinode. This pattern of bonding and antibonding linear combinations is inverted when compared to the nodal patterns observed for the in-gap states 2 and 3 associated with the 7/9/7 TQD (Fig. 4.2(B)). The energy gap between in-gap states 6 and 7 implies that the electron hopping amplitude between topological junction states across the short 7-AGNR segment is roughly one-seventh of that across the 9-AGNR segment: $E_{g2} = |2t_2| = 0.1eV$. The values of both t_1 and t_2 obtained on these two TQDs are consistent with the measured band gap of a 7/9-AGNR superlattice.[38]

4.3 Theretical Analysis

To better understand the wavefunction characteristics and energetic alignment of TQD states, we compute the electronic states in our TQDs using first-principles DFT calculations. GNR point spectra collected on the 7/9/7 TQD were modeled by evaluating the DFT local

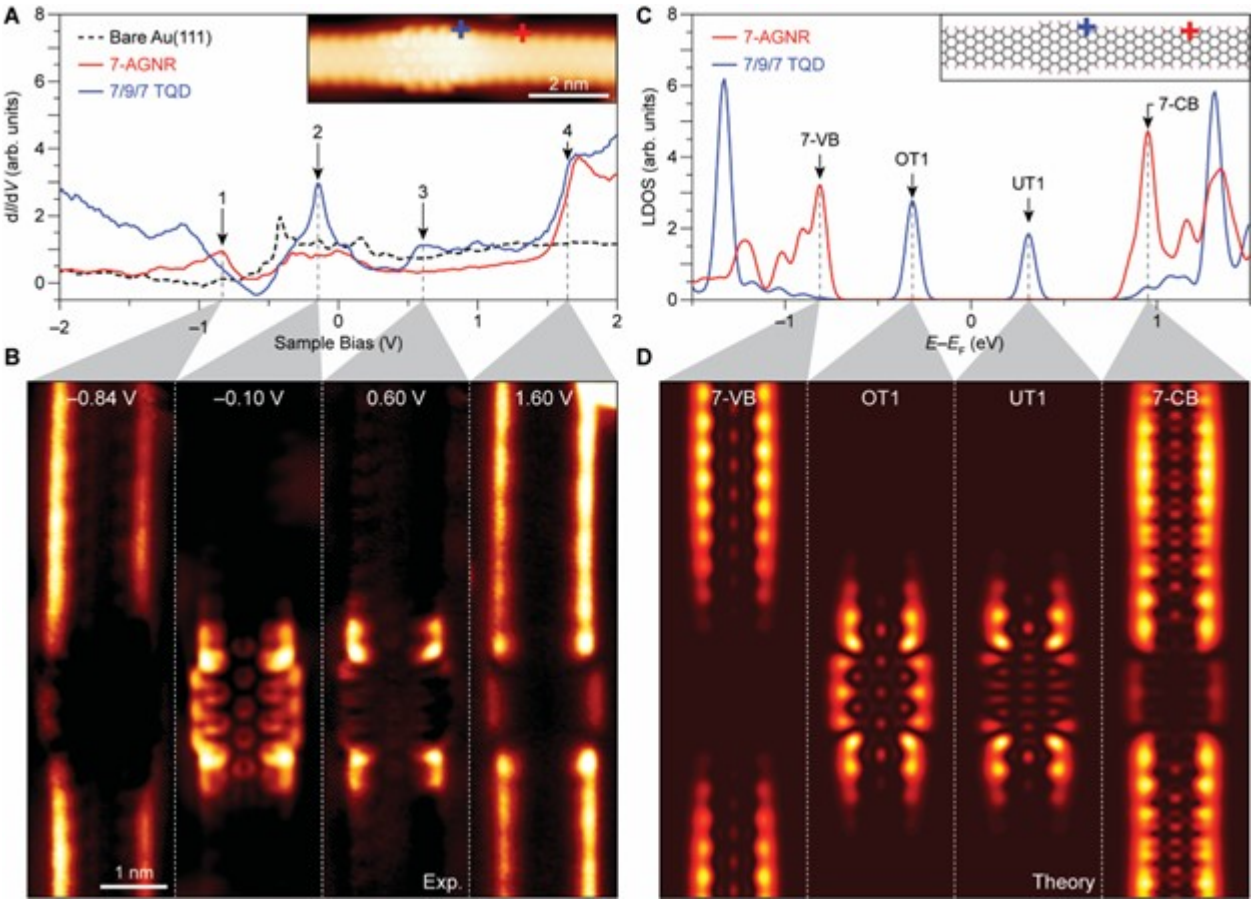

Figure 4.2: Electronic structure of 7/9/7 topological quantum dot. (A) Inset: STM topographic image of the 7/9/7 topological quantum dot (V_s = –0.10 V, I_t = 90 pA). dI/dV point spectroscopy conducted on the 7-AGNR bulk and the 7/9/7 TQD are plotted in red and blue, respectively, as indicated in the inset. The dashed black curve corresponds to a reference spectrum conducted on bare Au(111). For all point spectra, V_{AC} = 10 mV. (B) dI/dV maps of the 7/9/7 TQD conducted at the indicated biases corresponding to peaks in (A) (I_t = 90 pA, V_{AC} = 20 mV). (C) DFT-LDA calculated LDOS for the theoretical 7/9/7 TQD structure shown in Fig. 4.5(A). The blue and red curves correspond to LDOS sampled over the region indicated by the blue and red crosses in the inset, respectively (spectrum broadened by 10 meV Gaussian). (D) DFT-calculated LDOS map of the 7/9/7 TQD at each of the four peak energies indicated in (C). LDOS is sampled 4 $\AA$ above the GNR plane. T = 4 K for all measurements.

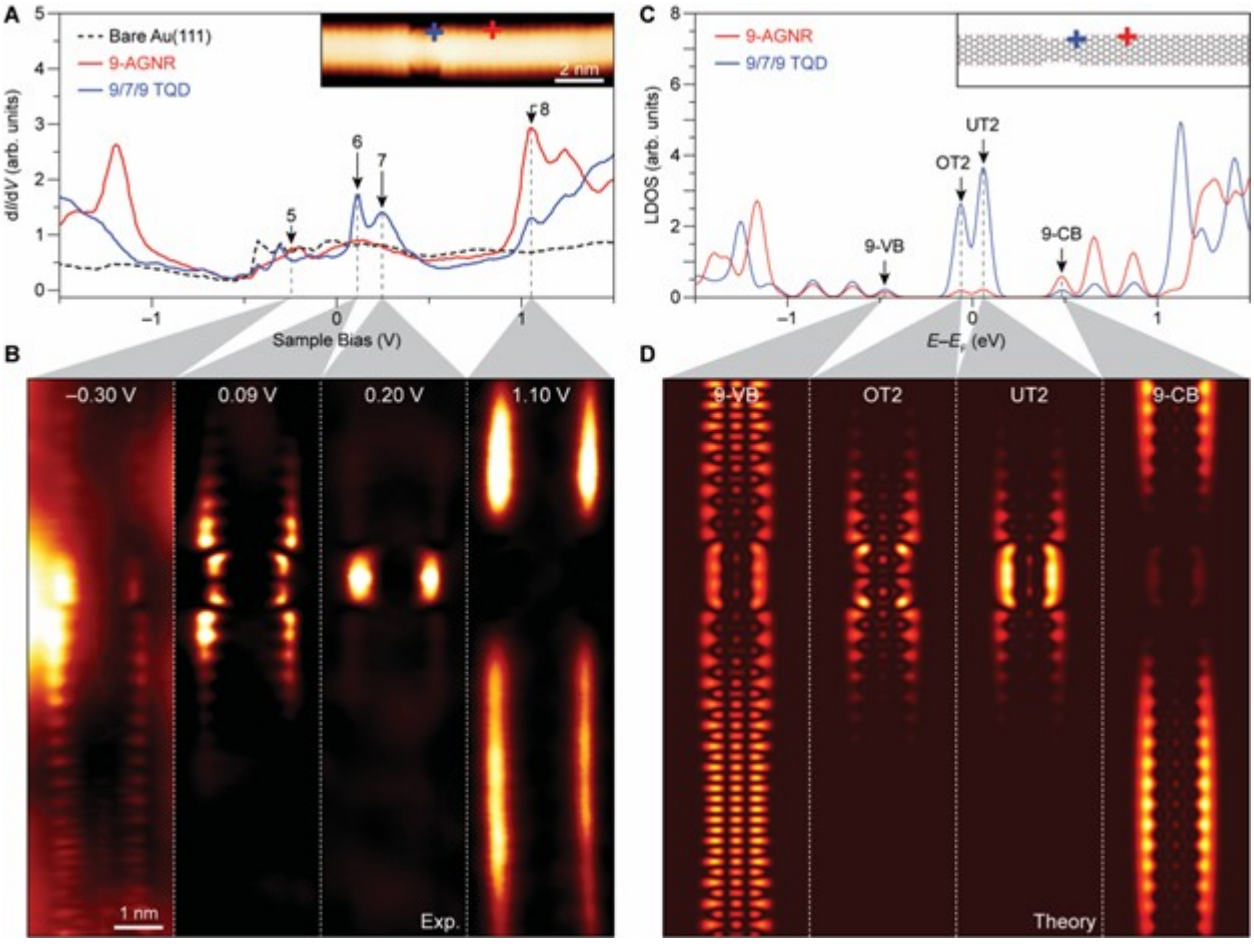

Figure 4.3: Electronic structure of 9/7/9 topological quantum dot. (A) Inset: STM topographic image of the 9/7/9 topological quantum dot (V_s = 0.20 V, I_t = 3 nA). dI/dV point spectroscopy conducted on the 9-AGNR bulk and the 9/7/9 TQD are plotted in red and blue, respectively, as indicated in the inset. The dashed black curve corresponds to a reference spectrum conducted on bare Au(111). For all point spectra, V_{AC} = 10 mV. (B) dI/dV maps of the 9/7/9 TQD conducted at the indicated biases corresponding to peaks in (A) (State 5: I_t = 8 nA, V_{AC} = 20 mV; States 6–8: I_t = 3 nA, V_{AC} = 20 mV). (C) DFT-LDA calculated LDOS for the theoretical 9/7/9 TQD structure shown in Fig. 4.5(B). The blue and red curves correspond to LDOS sampled over the region indicated by the blue and red crosses in the inset, respectively (spectrum broadened by 10 meV Gaussian). (D) DFT-calculated LDOS map of the 9/7/9 TQD at each of the four peak energies indicated in (C). LDOS is sampled 4 $\AA$ above the GNR plane. T = 4 K for all measurements.

density-of-states (LDOS) located in the 7-AGNR bulk as well as at the 7/9-AGNR junction (as indicated by the crosshairs in the inset in Fig. 4.2(C)). The LDOS sampled in the 7-AGNR bulk resulted in a prominent occupied-state peak associated with the bulk valence band (labeled 7-VB) and an unoccupied-state peak associated with the conduction band (labelled 7-CB), in reasonable alignment with experimental features 1 and 4. The LDOS sampled in the 7/9-AGNR junction region is dominated by two low-energy states that gap symmetrically about E_F (labeled occupied topological state 1 (OT1) and unoccupied topological state 1 (UT1) and is in good agreement with experimental states 2 and 3. Fig. 4.2(D) shows the theoretical LDOS maps for the 7-VB, OT1, UT1, and 7-CB states. The theoretical LDOS maps mirror most of the salient features seen in the experimental data in Fig. 4.2(B), including the extending of the 7-VB and 7-CB states throughout the 7-AGNR bulk region and confinement of the OT1 and UT1 states to the topological junctions. Notably, the nodal structure of the theoretical OT1 and UT1 LDOS mirrors that of experimental states 2 and 3. These theoretical results support the conclusion that the four experimental peaks observed in the 7/9/7 TQD correspond to bulk 7-AGNR band edge van Hove singularities along with two in-gap topological states.

Theoretical analysis of the 9/7/9 TQD yields similar good physical understanding of the experimental data. Specifically, the LDOS in the 9-AGNR bulk shows peaks associated with the pristine 9-AGNR top valence and bottom conduction bands (9-VB and 9-CB of Fig. 4.3(C); red curve), while the LDOS in the 7/9 junction region reveals a pair of in-gap states (occupied and unoccupied topological state 2 (OT2 and UT2) of Fig. 4.3(C); blue curve). The theoretical LDOS maps for these four states (Fig. 4.3(D)) show again agreement with the experimental dI/dV maps for features 5–8 (Fig. 4.3(B)). For example, OT2 has a nodal line at the center of the 7-AGNR segment (similar to state 6 in Fig. 4.3(B)), while UT2 shows an antinode (similar to state 7 in Fig. 4.3(B)). We note that states 6 and 7 both appear at positive bias (rather than gapping symmetrically about V = 0) due to charge transfer with the underlying Au(111) surface as observed previously for AGNR-supported zero-mode states.[38][39][91] These theoretical results demonstrate that our experimental observations reflect the intrinsic topologically-based electronic behavior of both 9/7/9 and 7/9/7 TQDs.

A useful analysis can be used to deconvolute the TQD states in the two quantum dots (QDs) in order to gain further insight into their energetic alignment and physical origin. We accomplish this by calculating the interface state for an isolated 7/9-AGNR topological junction (characterized by a zero mode at E_F) and using it as a basis state to build up the TQD in-gap state eigenfunctions. The top panel of Fig. 4.4(A) shows the wavefunction for such an isolated zero mode with a 7/9 orientation (denoted $|\psi_0^L\rangle$) which has a 7-AGNR segment on the left and a 9-AGNR segment on the right and is overlaid on the left junction of a 7/9/7 TQD. The bottom panel of Fig. 4.4(A) shows an isolated zero mode with the opposite 9/7 orientation overlaid on the right 7/9/7 junction (denoted $|\psi_0^R\rangle$). If these states interact via an electron hopping amplitude t_1, then the effective Hamiltonian is diagonalized by states of antisymmetric and symmetric linear combinations of $|\psi_0^L\rangle$ and $|\psi_0^R\rangle$ (Fig. 4.4(B)) that possess eigenenergies $\pm t_1$ relative to E_F. These states are analogous to the UT1 and OT1 states shown in the 7/9/7 TQD ab initio energy level diagram (energies reproduced in Fig. 4.4(C)). For a positive t_1, the symmetric state $\frac{1}{\sqrt{2}}[|\psi_0^L\rangle+|\psi_0^R\rangle]$ (which has zero nodes) is lower in energy than the antisymmetric state $\frac{1}{\sqrt{2}}[|\psi_0^L\rangle-|\psi_0^R\rangle]$ (which has one node) (Fig.

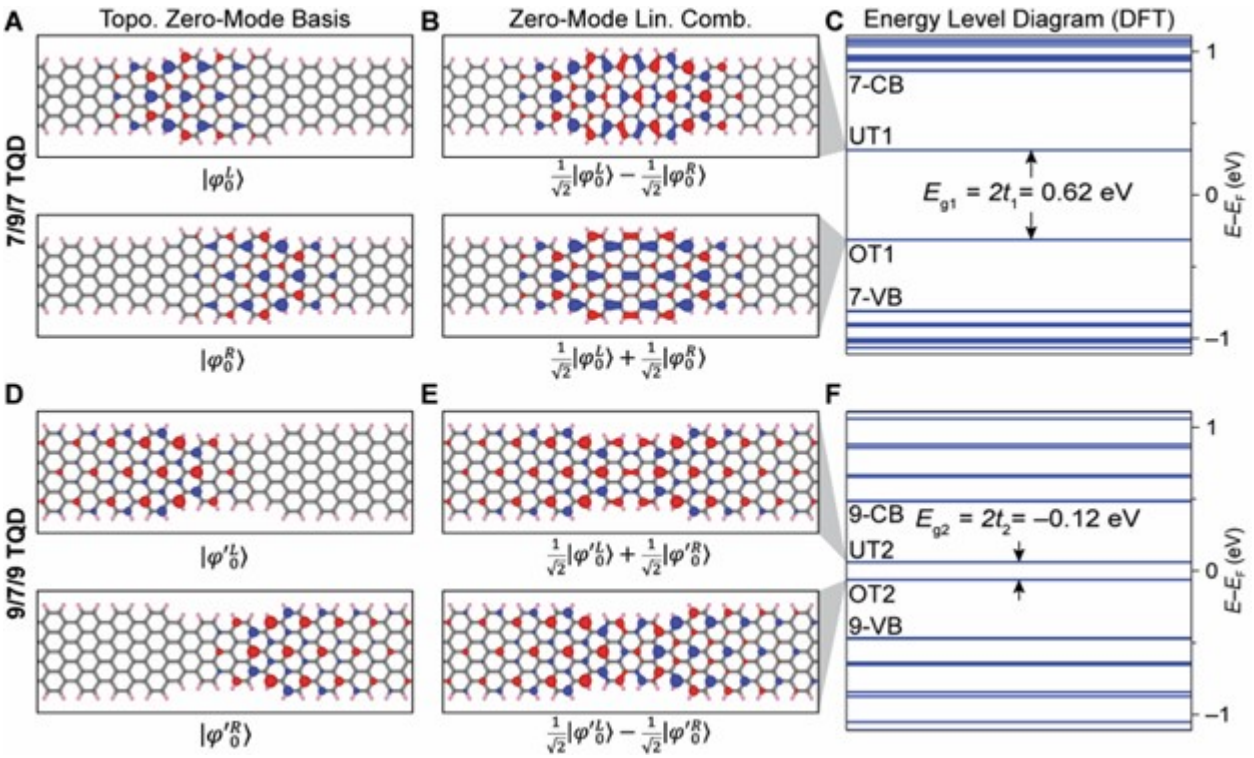

Figure 4.4: Emergence of quantum dot states from topological zero modes. (A) Left and right topological zero-mode basis states ($|\psi_0^L\rangle$ and $|\psi_0^R\rangle$ in the top and bottom panels, respectively) superimposed on the 7/9/7 TQD chemical structure. Color indicates the sign of the phase factor. (B) Symmetric (bottom panel) and antisymmetric (top panel) linear combinations of zero-mode states shown in (A) correspond to the OT1 and UT1 states in the 7/9/7 TQD. (C) The DFT-LDA energy level diagram associated with a superlattice of a finite length theoretical 7/9/7 TQD structure (detailed structure in Fig. 4.5(A)). The frontier energy levels originating from the 7-AGNR bulk are labeled 7-CB and 7-VB and the quantum dot states are UT1 and OT1. The energy splitting between UT1 and OT1 is equal to twice the electron hopping amplitude t_1 between $|\psi_0^L\rangle$ and $|\psi_0^R\rangle$. (D) Same as (A) but for the 9/7/9 TQD. Here the left and right zero-mode basis states are labeled $|\psi_0'^L\rangle$ and $|\psi_0'^R\rangle$ as shown in the top and bottom panels, respectively. (E) Same as (B) but for the 9/7/9 TQD. In contrast to the states shown in (B), the symmetric linear combination of zero-mode states has a higher energy than the antisymmetric linear combination. (F) Same as (C) but for the 9/7/9 TQD from a superlattice of the finite length structure shown in Fig. 4.5(B). Here the electron hopping amplitude t_2 between $|\psi_0'^L\rangle$ and $|\psi_0'^R\rangle$ is negative as dictated by the energy ordering of the symmetric and antisymmetric linear combinations of zero-mode states.

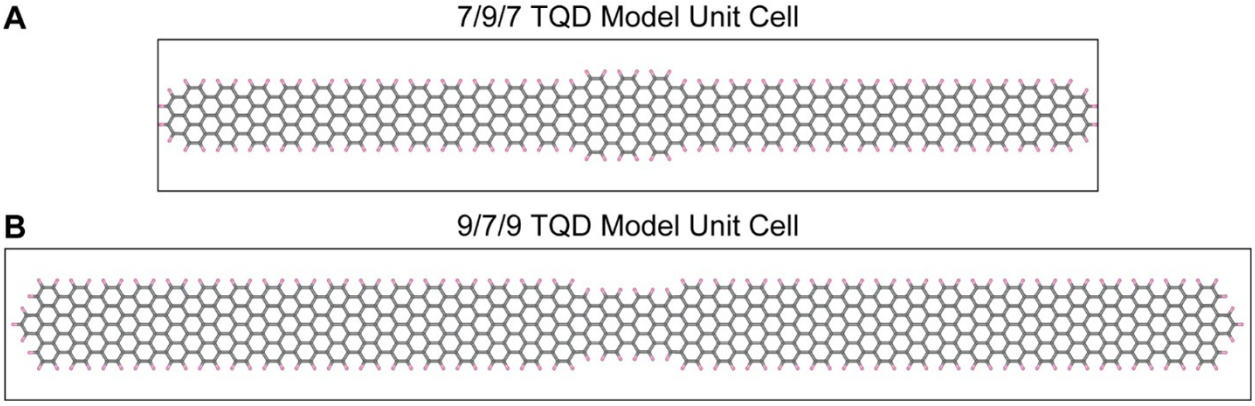

Figure 4.5: Model GNR TQDs used for DFT calculations. (A) Model unit cell of the 7/9/7 TQD used for DFT-LDA calculations presented in Fig. 4.2, 4.4(A), (B), and (C). (B) Model unit cell of the 9/7/9 TQD used for the DFT-LDA calculations presented in Fig. 4.3, 4.4(D), (E), and (F).

4.4(B)). This is consistent with the experimental observation of Fig. 4.2 that the TQD state with a central antinode (state 2) is lower in energy than the nodal state (state 3), and demonstrates that t_1 ¿ 0.

When we repeat this process for the 9/7/9 TQD, we get a somewhat different result. Here we label the left- and right-hand topological zero modes as $|\psi_0'^L\rangle$ and $|\psi_0'^R\rangle$ (Fig. 4.4(D)), and once again introduce an electron hopping amplitude t_2 between them which causes splitting of the energy of the states around E_F and formation of symmetric and antisymmetric linear combinations (Fig. 4.4(E)). As expected, the symmetric state (top panel, Fig. 4.4(E)) shows an antinode whereas the antisymmetric state has a central node. In contrast to the 7/9/7 case, however, the antisymmetric state $\frac{1}{\sqrt{2}}[|\psi_0'^L\rangle$-$|\psi_0'^R\rangle]$ (which corresponds to OT2) is a lower-energy eigenstate than the symmetric state $\frac{1}{\sqrt{2}}[|\psi_0'^L\rangle+|\psi_0'^R\rangle]$ (which corresponds to UT2) in both DFT and experiment. Hence, the electron hopping amplitude in this case is negative (t_2 ¡ 0).

The fact that the hopping amplitudes of the 9/7/9 and 7/9/7 cases are opposite in sign is a consequence of the phase structure of the zero-mode wavefunction and the contrasting edge structures of the two TQDs (i.e., wide-narrow-wide versus narrow-wide-narrow, respectively). To show this, one can write an explicit expression for the hopping amplitudes between the junction states in both TQDs in a π-orbital basis.

First, we consider the left zero mode of the 7/9/7-AGNR junctions ($|\psi_0^L\rangle$) shown in Fig. 4.6(A). We can represent the Hamiltonian of the single junction system within a tight-binding framework with 1st nearest neighbor hopping on a π-orbital basis as:

$$H_{79} = \sum_{<i,j>_{n.n.}} t_{ij}|\phi_j\rangle\langle\phi_i| \tag{4.1}$$

where $t_{ij} = t$ within a nearest-neighbor hopping framework and $|\phi_i\rangle$ is the atomic π-orbital

state associated with atomic site i. The following is true of the zero mode $|\psi_0^L\rangle$ by definition:

$$H_{79}|\psi_0^L\rangle = 0 \tag{4.2}$$

Writing the zero mode as a linear combination of atomic π-orbitals $|\phi_i\rangle$ for all sites i:

$$|\psi_0^L\rangle = \sum_i C_i^L |\phi_i\rangle \tag{4.3}$$

where C_i^L is the amplitude of the wavefunction $|\psi_0^L\rangle$ on site i. Taking Eq. 4.1, 4.2, and 4.3 together, it follows that:

$$\sum_{\{i|\langle i,j\rangle n.n\}} t_{ji} C_i^L |\phi_i\rangle = 0 \quad \forall j \tag{4.4}$$

Therefore, for all sites j with nearest neighboring sites i, the sum of the amplitudes C_i^L is zero. For example, if we consider site 1 in Fig. 4.6 with nearest neighbor sites 2, 3, and 4, Eq. 4.4 implies that

$$t(C_2^L + C_3^L + C_4^L) = C_2^L + C_3^L + C_4^L = 0 \tag{4.5}$$

Now, we will consider the behavior of $|\psi_0^L\rangle$ within the 7/9/7 TQD structure described by a new Hamiltonian H_{797}. While the general form is similar to Eq. 4.1, we have now removed certain carbon sites compared to the system described by H_{79}, so $|\psi_0^L\rangle$ is no longer a zero mode of the new Hamiltonian H_{797}.

$$H_{797}|\psi_0^L\rangle \neq 0 \tag{4.6}$$

Therefore, Eq. 4.4 no longer holds in the new system. On the other hand, Eq. 4.5 is a property of $|\psi_0^L\rangle$ and would still be valid. $|\psi_0^R\rangle$ is simply a mirrored state of $|\psi_0^L\rangle$ as a zero mode of Hamiltonian H_{97}. An explicit expression can be written for the hopping amplitude t_1 between $|\psi_0^L\rangle$ and $|\psi_0^R\rangle$:

$$t_1 = \langle \phi_0^L | H_{797} | \phi_0^R \rangle = \sum_{<i,j>n.n.} C_i^L C_j^R \langle \phi_i | H_{797} | \phi_j \rangle \tag{4.7}$$

where by definition

$$\langle \phi_i | H_{797} | \phi_j \rangle = t \tag{4.8}$$

is the nearest neighbor hopping of graphene. Therefore

$$t_1 = t \sum_{<i,j>n.n.} C_i^L C_j^R \tag{4.9}$$

Any term in Eq. 4.9 associated with site j where $C_j^R \neq 0$ in the 7/9/7 TQD and all adjacent sites i are also present in the single-junction structure will be exactly zero since all nearest neighbor C_i^L sum to zero according to Eq. 4.5. This is true of all interior carbon atoms. However, if site j in the 7/9/7 TQD does not possess the same nearest neighbors i as in the single-junction structure, equation 4.9 will have a non-zero term. This is true only for

the edge carbon atoms. For instance, consider site 1 in Fig. 4.6(A) and (B) with nearest-neighbor sites 2, 3, and 4. Site 4 is removed when generating the 7/9/7 TQD from H_{79}, and so one ends up with a non-zero term in Eq. 4.9, namely

$$t \times C_1^R(C_2^L + C_3^L) \tag{4.10}$$

Based on Eq. 4.5 and the fact that $C_4^L < 0$ as shown in Fig. 4.6(B), it can be inferred that $C_2^L + C_3^L > 0$. Since $C_1^R > 0$, this means the typical non-zero term shown in Eq. 4.10 is positive. It can be shown exhaustively that all such non-zero terms are similarly positive, and t_1 is therefore positive. One can infer from this argument that for any TQD with the same edge shape, a wider interconnecting region requires the removal of lattice sites compared to the single-junction case, and so will have a positive hopping term.

For the 9/7/9 TQD, the situation is slightly different (Fig. 4.6(C) and (D)). Here, after substituting H_{79} by H_{97}, the zero mode on the left side of the junction, $|\psi_0'^L\rangle$, obeys Eq. 4.1 – 4.4 like $|\psi_0^L\rangle$. As before, we can represent the zero mode as a linear combination of π-orbitals $|\phi_i\rangle$ for each site i with amplitudes $C_i'^L$. The hopping amplitude t_2 can be written in terms of the new Hamiltonian H_{979} and the π amplitudes of $|\psi_0'^L\rangle$ and $|\psi_0'^R\rangle$:

$$t_2 = \langle\phi_0'^L|H_{979}|\phi_0'^R\rangle = \sum_{<i,j>n.n.} C_i'^L C_j'^R \langle\phi_i|H_{979}|\phi_j\rangle = t \sum_{<i,j>n.n.} C_i'^L C_j'^R \tag{4.11}$$

By the same argument as in the 7/9/7 TQD case, all interior lattice sites will be associated with terms that are exactly zero, while only the edge sites contribute non-zero terms. Unlike in the 7/9/7 case, the formation of the 9/7/9 TQD is associated with the addition (rather than the subtraction) of lattice sites as compared to H_{97} on the right junction as indicated in Fig. 4.6(D). For example, consider the non-zero term associated with site 6:

$$t \times C_6'^R(C_5'^L + C_7'^L) \tag{4.12}$$

Here, $C_6'^R < 0$ and $C_5'^L > 0$ as indicated in Fig. 4.6(D). Since lattice site 7 does not exist in the unperturbed left-hand junction shown in Fig. 4.6(C), $C_7'^L = 0$ and the term shown in Eq. 4.12 is negative. It can also be shown exhaustively that all such non-zero terms are similarly negative and t_2 is therefore negative. Since any TQD with a narrow interconnecting region is generated by adding lattice sites to the unperturbed Hamiltonian, one can infer that all such TQDs with the same interfacial edge shape will have a negative hopping term.

Thus, by tracking the spatial variation of the phase on the π-orbitals of the zero-mode wavefunctions along the junction edge, it can be seen that all non-zero terms in the analytical expression for t_1 are positive, whereas all non-zero terms for t_2 are negative. This is a general property of all topologically non-trivial junctions formed between coaxial n- and n+2-AGNRs with zigzag'/zigzag junctions where the middle segment is either an n+2 segment (resulting in $t_{eff} > 0$) or an n segment (resulting in $t_{eff} < 0$) under the constraint that n is odd. Hence, the sign of the TQD junction-state hopping amplitude and likewise the symmetry of the associated topological quantum dot states can be tuned based on the width of the interconnecting region relative to the GNR bulk region.

The smaller energy splitting for the 9/7/9 TQD compared to the 7/9/7 TQD can be understood by inspecting the zero-mode wavefunction and noticing that its amplitude decays more rapidly in the central 7-AGNR regions compared to the decay of the wavefunction

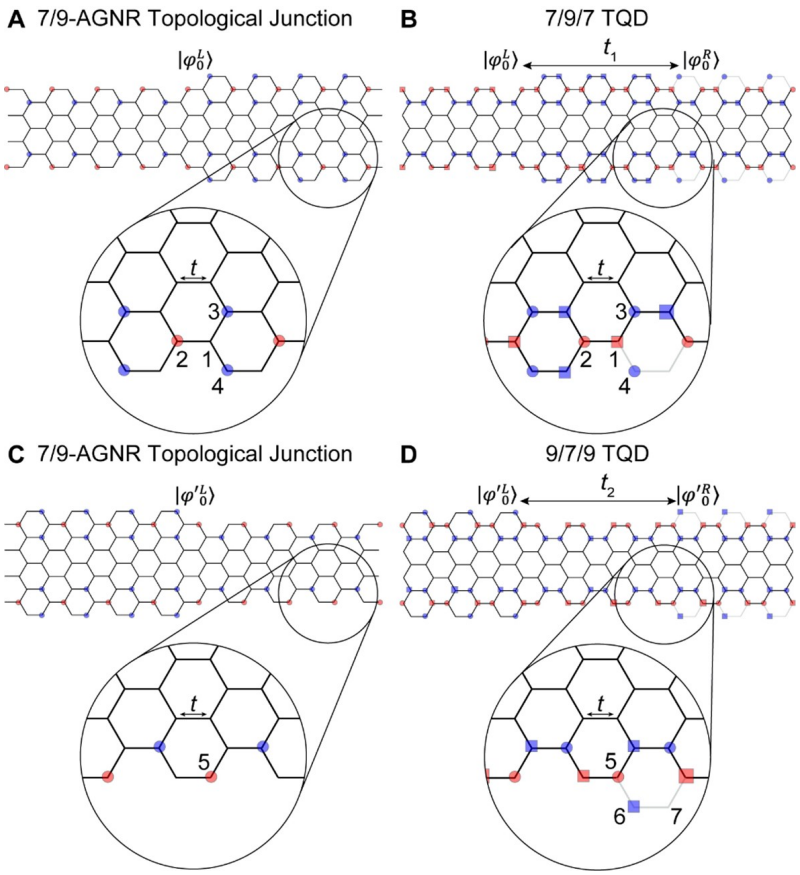

Figure 4.6: (A) Schematic plot of a 7/9-AGNR topological junction showing the phase factor on each of the π orbitals forming the zero-mode wavefunction $|\psi_0^L\rangle$ near the edge carbon atoms (red represents a positive phase factor, blue a negative phase factor). The zero mode can be written as a linear combination of atomic π-orbitals, or $|\psi_0^L\rangle = \sum_i C_i^L \phi_i$. The sum of the amplitudes of the zero-mode wavefunction on sites 2, 3 and 4 is zero. (B) Schematic of the 7/9/7 TQD with the phase factor on each π-orbital of the left and right zero-mode wavefunctions ($|\psi_0^L\rangle$ and $|\psi_0^R\rangle$) indicated by colored circles and squares, respectively. The gray bonds indicate those which are removed when generating the 7/9/7 TQD. The hopping amplitude t_1 between $|\psi_0^L\rangle$ and $|\psi_0^R\rangle$ is composed of terms such as $t \times C_1^R(C_2^L + C_3^L)$. From the diagram, it is clear that $C_1^L > 0$, and one can infer that $C_2^L + C_3^L > 0$ since $C_2^L + C_3^L + C_4^L = 0$ and $C_4^L < 0$. Together, these imply that $t_1 > 0$ (C) Similar schematic plot as shown in (A) of 9/7-AGNR topological junction. The phase factor on atomic site 5 is positive. (D) Same schematic plot as in (B) for 9/7/9 TQD. The gray bonds indicate those which are added when generating the 9/7/9 TQD. The hopping amplitude t_2 between $|\psi_0'^L\rangle$ and $|\psi_0'^R\rangle$ is composed of terms such as $t \times C_6'^R(C_5'^L + C_7'^L)$. From the diagram, it is clear that $C_6'^R < 0$, $C_5'^L > 0$, and $C_7'^L = 0$. Therefore, the hopping amplitude $t_2 < 0$.

amplitude in the 9-AGNR (Fig. 4.4(A),(D), 4.7). Therefore, the relative overlap between $|\psi_0'^L\rangle$ and $|\psi_0'^R\rangle$ across the 7-AGNR segment will be less than the overlap between $|\psi_0^L\rangle$ and $|\psi_0^R\rangle$ across the 9-AGNR segment, causing a reduction in the magnitude of t_2 compared to t_1. As expected, all four hybrid states in both TQDs possess a larger DOS in the 9-AGNR regions compared to the 7-AGNR regions (Fig. 4.7). This suggests that the necessary conditions for hosting magnetic states should be more readily achievable using the 9/7/9 scheme since the hopping amplitude is inherently smaller than in the 7/9/7 case. Since the hopping parameter should decay exponentially with the distance between topological interface states, one could realize a magnetic ground state by simply further separating the topological interface states. Indeed, first-principles calculations show that the 9/7/9 structure possesses an antiferromagnetic ground state with just five unit cells in the central segment, while the 7/9/7 structure requires 12 unit cells (Fig. 4.8). It is evident that the ability to control the energy splitting and emergence of magnetic properties in GNR TQDs is ultimately dictated by the relative decay length of the constituent zero-mode wavefunctions at either side of a topological heterojunction. Intuition based on perturbation of bulk wavefunctions would suggest that the zero-mode decay length is inversely proportional to the intrinsic gap of the supporting GNR. At first glance, this phenomenology appears to bare out in our experiment since the topological junction state extends further into the 9-AGNR regions compared to the 7-AGNR regions (the latter of which has a band gap more than twice the prior). However, closer scrutiny of this and related structures reveals that such intuition does not generally hold for all types of terminations and junctions of GNRs, where small changes in the atomic-scale interfacial structure can have a substantial impact on the resultant spatial distribution of topological zero-modes.

Origin of Zero-Mode Decay Length: End States

In Fig. 4.4 and 4.7, it is shown that the topological zero-mode state formed at the junction of the zigzag' 7-AGNR and zigzag 9-AGNR decays much more rapidly in the 7-AGNR region compared to the 9-AGNR region. In order to explain the origin of this behavior, we have developed a procedure for extracting the decay length of topological zero-modes for topologically non-trivial AGNR junctions and end states. While arguments based on perturbation of bulk wavefunctions would suggest that the zero-mode decay length should scale inversely with the intrinsic gap of the host GNR, this behavior is not observed to hold for several counter examples shown in Fig. 4.9 and 4.10. In particular, when forming a vacuum interface, the 7-AGNR end state decay length is actually longer than that of the 9-AGNR end state, despite the latter possessing a smaller intrinsic gap. Moreover, an alternative topologically non-trivial 7/9-AGNR junction can be chosen which shows more rapid decay in the 9-AGNR compared to the 7-AGNR (i.e., the opposite behavior for the zigzag/zigzag' junction explored experimentally) (Fig. 4.10(B–D)). Therefore, it appears that the zero-mode decay length depends not only on the width of the host GNR, but the boundary conditions enforced at interfaces with other GNRs or vacuum.

We systematically explore this behavior by first considering end states on zigzag termini of odd-width AGNRs (Fig. 4.9(A)). Here we only need to consider sublattice-polarized states that are localized on the graphene sublattice associated with the outer most carbon atoms of the zigzag edge (herein called the A-sublattice) from the chiral symmetry classification

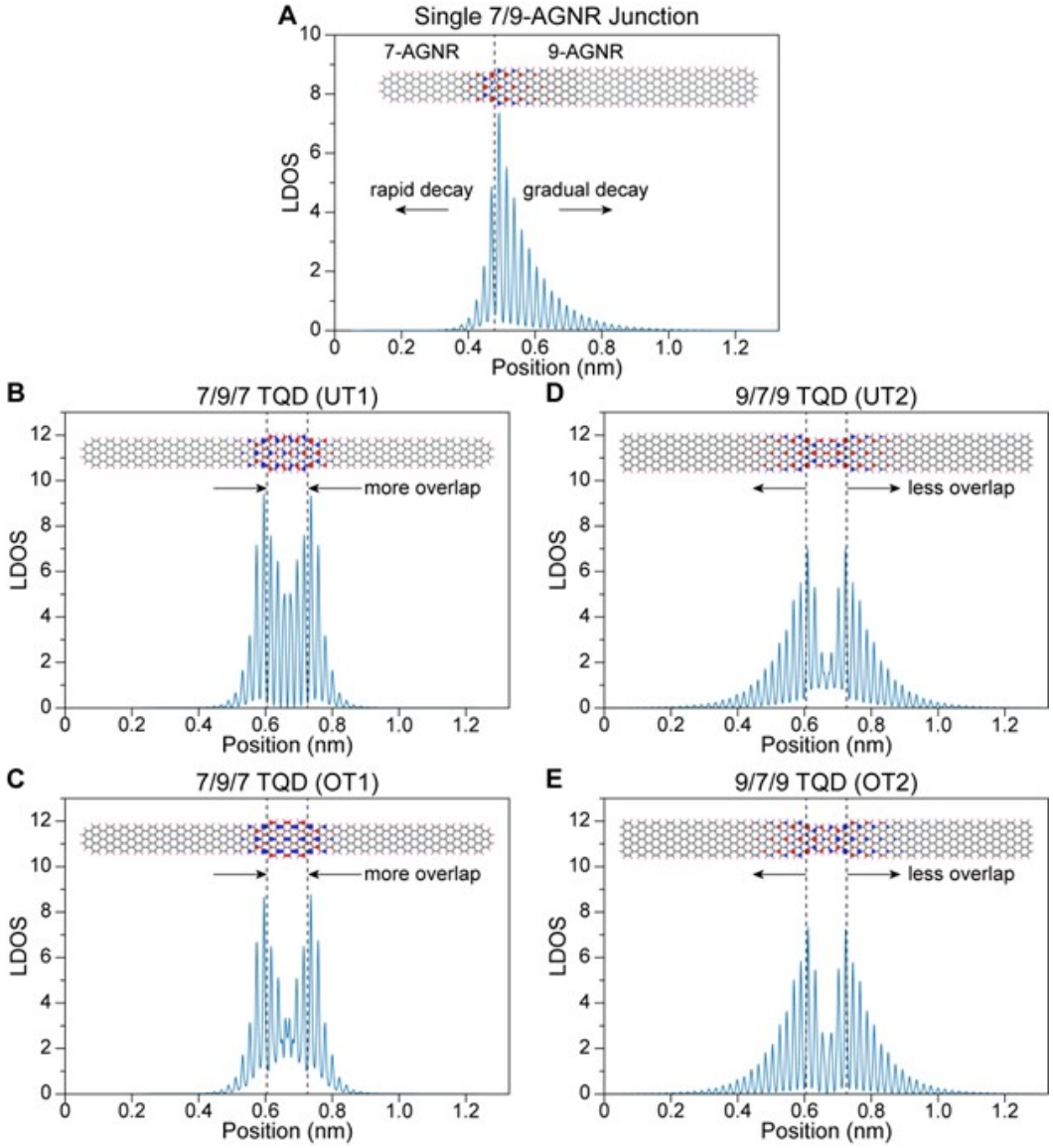

Figure 4.7: Spatial dependence of LDOS in 7/9-AGNR junction and TQD states. (A) The LDOS of the 7/9-AGNR zero-mode state integrated over the GNR width. The inset shows a top-down view of isosurfaces of constant LDOS for the same state. The state decays rapidly on the 7-AGNR side of the junction and gradually on the 9-AGNR side of the junction. (B) The same as (A) but for UT1, (C) OT1, (D) UT2 and (E) OT2. Due to the gradual decay of the single junction state into the 9-AGNR region as shown in (A), the interface states have a higher LDOS in the intermediate 9-AGNR region for UT1 and OT1 compared to the LDOS in the 7-AGNR region for UT2 and OT2. This indicates a larger overlap and thus a larger hopping between states in the 7/9/7 TQD compared to those in the 9/7/9 TQD.

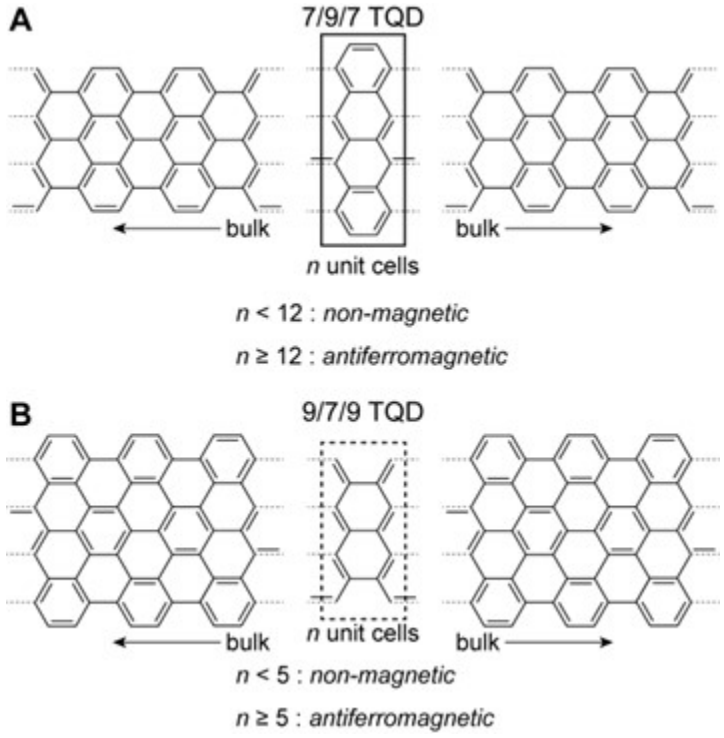

Figure 4.8: Conditions for magnetic ground states in AGNR TQDs. (A) Schematic representation of a 7/9/7 TQD with an interconnecting 9-AGNR central segment possessing a variable length of n unit cells. Using the tight-binding self-consistent field (SCF) method we determine that a minimum length n =12 is required for the 7/9/7 TQD to host an antiferromagnetic ground state. (B) Schematic of a 9/7/9 TQD with an interconnecting 7-AGNR central segment possessing a variable length of n unit cells. SCF calculations determine that for lengths $n \geq 5$ this structure hosts an antiferromagnetic ground state.

theory[1].Within the terminal unit cell, the amplitude of the wavefunction on the A-sublattice in the first column is labelled $A_i^{(1)}$ while those in the second column are labelled $A_i^{(2)}$. For an N carbon wide AGNR, the index i ranges from 1 to $n = (N-1)/2$ for the first column and ranges from 1 to $n+1 = (N+1)/2$ for the second column. We then introduce the parameter β to represent the decay factor of the wavefunction from the terminal unit cell to the neighboring unit cell, whose first and second columns now possess wavefunction amplitudes of $\beta A_i^{(1)}$ and $\beta A_i^{(2)}$, respectively. In general, these amplitudes become $\beta^{k-1} A_i^{(1)}$ and $\beta^{k-1} A_i^{(2)}$ for the kth unit cell from the terminal unit cell.

Based on the derivation in the previous section, we have shown that in addition to being sublattice polarized, a zero-mode state behaves such that for a given atomic site, the sum of the amplitudes of the wavefunction on all nearest neighboring sites must add to zero. Enforcing this rule at the four locations circled in Fig. 4.9(A), we can derive the following constraints on the wavefunction amplitudes:

$$A_1^{(1)} = -A_1^{(2)} \tag{4.13}$$

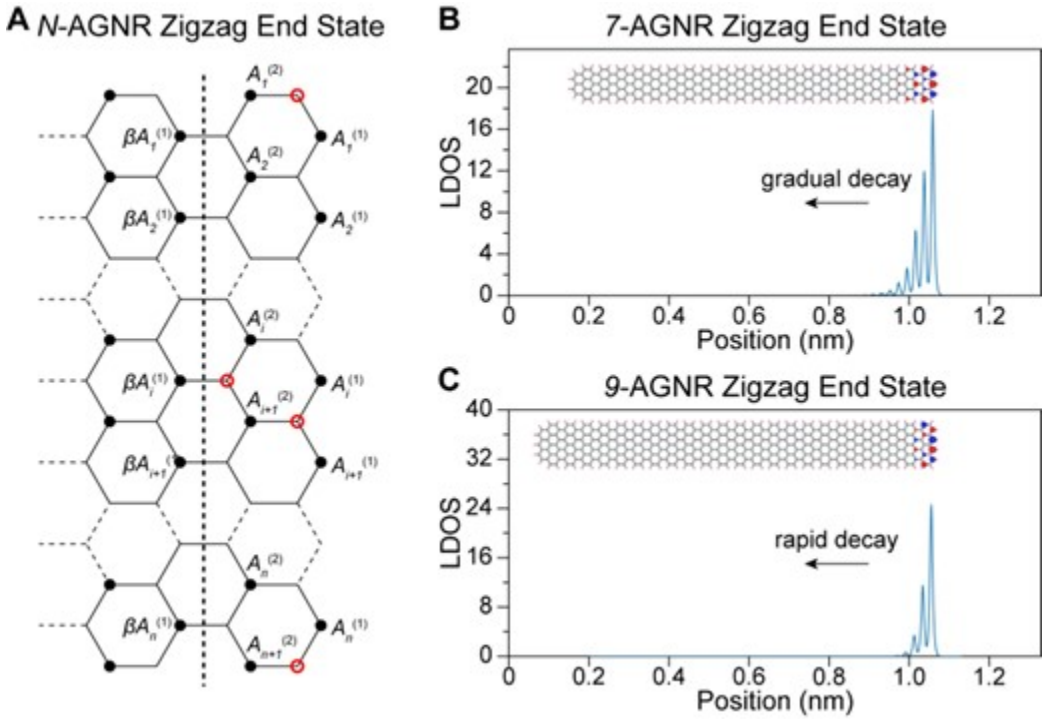

Figure 4.9: Decay length of topological end states. (A) Schematic of N-atom-wide AGNR with a zigzag terminus on the right. The A-sublattice is indicated with black circles. Here, $\beta^{k-1}A_i^{(j)}$ represents the amplitude of a generic A-sublattice-polarized end state in the jth column and ith row of the kth unit cell from the end, where β is the characteristic end state decay length. The sum of all nearest-neighbor amplitudes for any atomic site is zero. Applying this rule to the atomic sites circles in red provides the necessary constraints to solve for β. (B) Local density of states for a 7-AGNR zigzag end state showing exponential decay from the GNR terminus. The inset shows isosurfaces of constant LDOS for the same state with the red and blue colors indicating the phase factor. (C) Same as (B) but for the 9-AGNR zigzag end state. The 9-AGNR end state decays more rapidly than the 7-AGNR end state.

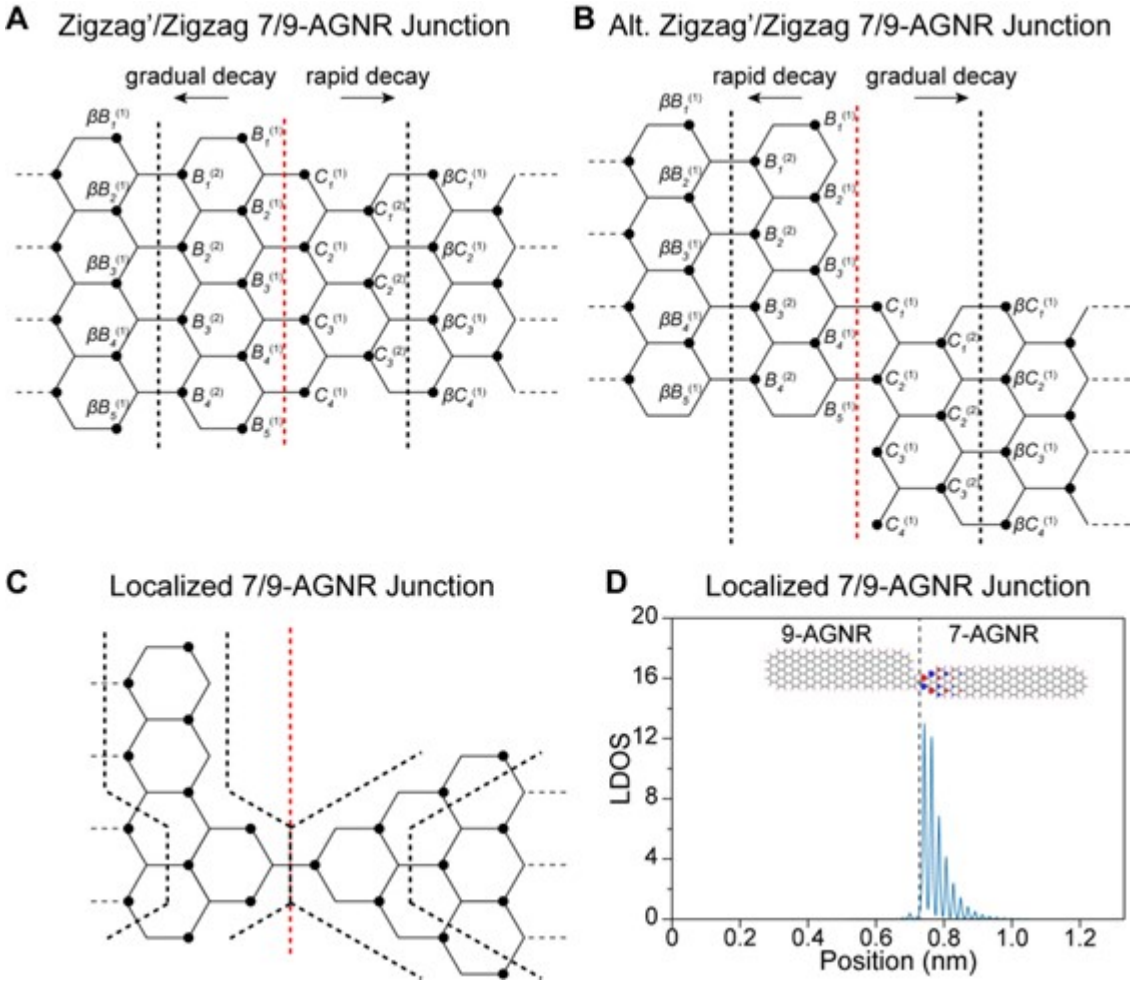

Figure 4.10: Boundary conditions on topological interface states (A) Schematic of the zigzag'/zigzag 7/9-AGNR junction explored in experiment. The B-sublattice is marked by black circles. Here, $\beta^{k-1}B_i^{(j)}$ and $\beta^{k-1}C_i^{(j)}$ represent the amplitudes of a generic B-sublattice-polarized state in the jth column and ith row of the kth unit cell from the interface on the 9-AGNR and 7-AGNR side of the junction, respectively. A topological interface state in this junction will extend further into the 9-AGNR side of the interface compared to the 7-AGNR side. (B) Same as (A) but the connection between the 7-AGNR and 9-AGNR has been shifted laterally by two rows. As a result of this shift, the topological interface state extends further into the 7-AGNR compared to the 9-AGNR. (C) A hypothetical topological 7/9-AGNR interface in which the boundary conditions associated with the interfacial geometries causes the topological interface state to be essentially completely localized on the 7-AGNR side of the interface. (D) The local density of states for the topological interface state associated with the junction shown in (C). The inset shows isosurfaces of constant LDOS for the same state with the red and blue colors indicating the phase factor.

$$A_{i+1}^{(2)} = -\beta A_i^{(1)} - A_i^{(2)} \tag{4.14}$$

$$A_{i+1}^{(1)} = -A_i^{(1)} - A_{i+1}^{(2)} = A_i^{(2)} + (\beta - 1)A_i^{(1)} \tag{4.15}$$

$$(\beta - 1)A_n^{(1)} + A_n^{(2)} = 0 \tag{4.16}$$

Eq. 4.14 and 4.15 can be summarized as a matrix equation

$$\begin{pmatrix} A_{i+1}^{(1)} \\ A_{i+1}^{(2)} \end{pmatrix} = M \begin{pmatrix} A_i^{(1)} \\ A_i^{(2)} \end{pmatrix}; \quad M = \begin{pmatrix} \beta - 1 & 1 \\ -\beta & -1 \end{pmatrix} \tag{4.17}$$

Applying Eq. 4.17 recursively across the width of the GNR, we find

$$\begin{pmatrix} A_n^{(1)} \\ A_n^{(2)} \end{pmatrix} = M \begin{pmatrix} A_1^{(1)} \\ A_1^{(2)} \end{pmatrix} \tag{4.18}$$

Combining Eq. 4.16 with 4.18, we get

$$\begin{pmatrix} \beta - 1 & 1 \end{pmatrix} \begin{pmatrix} A_n^{(1)} \\ A_n^{(2)} \end{pmatrix} = \begin{pmatrix} \beta - 1 & 1 \end{pmatrix} M^{n-1} \begin{pmatrix} A_1^{(1)} \\ A_1^{(2)} \end{pmatrix} = 0 \tag{4.19}$$

Without loss of generality, we can assign $A_1^{(1)} = 1$ (i.e., the wavefunction can be normalized later solving for β). Combining Eq. 4.13 and 4.19 and using the definition $n = (N-1)/2$, we find

$$\begin{pmatrix} \beta - 1 & 1 \end{pmatrix} M^{\frac{N-3}{2}} \begin{pmatrix} 1 \\ -1 \end{pmatrix} = 0; \quad M = \begin{pmatrix} \beta - 1 & 1 \\ -\beta & -1 \end{pmatrix} \tag{4.20}$$

Thus, in order to determine the decay length β for a topological zigzag end state of an odd N-width AGNR, one need only solve Eq. 4.20 for β. While Eq. 4.20 may yield multiple solutions, only those for which $|\beta| \leq 1$ are valid. Here it should be stressed that the form of Eq. 4.20 is completely determined by the bonding geometry of the terminating unit cell (i.e., zigzag) and the choice of sublattice (i.e., those of the outermost carbon atoms on the zigzag edge, herein called the A-sublattice). Determining the decay length of topological end states for arbitrary terminating geometries and sublattice polarization would modify the constraints in Eq. 4.13-4.16, and ultimately change the form and power of the matrix M in Eq. 4.20.

Two concrete applications of Eq. 4.20 are shown in Fig. 4.9(B), (C). The case of the 7-AGNR zigzag end state is shown in Fig. 4.9(B), where plugging in N=7 in Eq. 4.20 gives only one valid solution: $\beta = 0.586$. On the other hand, plugging in N=9 yields $\beta = 0.382$ (Fig. 4.9(C)). Hence, the 9-AGNR zigzag end state decays more rapidly than the 7-AGNR end state, despite the latter possessing a larger bulk band gap. This can be seen explicitly in the calculated LDOS for both states shown in Fig. 4.9(B), (C).

Origin of Zero-Mode Decay Length: junction States

Having established a procedure for determining the decay length of topological end states, we now turn to the task of finding the relative decay lengths of topological zero-modes in

AGNR heterojunctions. This approach will mirror the steps used for end states, where the geometry of interfacial unit cells along with a specific sublattice polarization will define a matrix equation to be solved for the decay length β. However, in the following examples, we will show that when multiple solutions for β are found, one must apply additional constraints based on the interfacial boundary conditions to determine the correct average value of β for either side of the junction.

Starting with the 7/9-AGNR heterojunction explored in this manuscript as well as [53] (Fig. 4.10(A)), we derive two matrix equations to solve for the decay lengths on either side of the interface. On the 9-AGNR side of the junction, the terminating unit cell is zigzag (as it was with the end state in the previous section). However, here the interface state is actually localized on the B-sublattice based on chiral classification theory (using the same convention defined above). Therefore, a new matrix equation will have to be derived for the 9-AGNR side of the interface. The zero-mode amplitude on carbon atoms in the first and second column of the interfacial unit cell are labelled $B_i^{(1)}$ and $B_i^{(2)}$. Equivalent locations k unit cells from the junction interface are labelled $\beta^{k-1}B_i^{(1)}$ and $\beta^{k-1}B_i^{(2)}$. Once again, for any given atomic site, the sum of the amplitudes of on all nearest-neighboring sites must add to zero. This yields the following constraints

$$B_1^{(1)} = -B_1^{(2)} \tag{4.21}$$

$$B_{i+1}^{(1)} + B_i^{(2)} + B_{i+1}^{(2)} = 0 \tag{4.22}$$

$$B_i^{(2)} + \beta B_i^{(1)} + \beta B_{i+1}^{(1)} = 0 \tag{4.23}$$

$$B_4^{(2)} + \beta B_4^{(1)} - \beta B_4^{(2)} = 0 \tag{4.24}$$

Using Eq. 4.22 and 4.23 to solve for $B_{i+1}^{(1)}$ and $B_{i+1}^{(2)}$ yields

$$B_{i+1}^{(1)} = -B_i^{(1)} - \frac{1}{\beta}B_i^{(2)} \tag{4.25}$$

$$B_{i+1}^{(2)} = B_i^{(1)} + \frac{1-\beta}{\beta}B_i^{(2)} \tag{4.26}$$

Eq. 4.25 and 4.26 can be written as a matrix equation

$$\begin{pmatrix} B_{i+1}^{(1)} \\ B_{i+1}^{(2)} \end{pmatrix} = M \begin{pmatrix} B_i^{(1)} \\ B_i^{(2)} \end{pmatrix}; \quad M = \begin{pmatrix} -1 & -\frac{1}{\beta} \\ 1 & \frac{1-\beta}{\beta} \end{pmatrix} \tag{4.27}$$

Applying recursively across the width of the GNR, Eq. 4.27 becomes

$$\begin{pmatrix} B_4^{(1)} \\ B_4^{(2)} \end{pmatrix} = M^3 \begin{pmatrix} B_1^{(1)} \\ B_1^{(2)} \end{pmatrix} \tag{4.28}$$

Without loss of generality, we can set $B_1^{(1)} = 1$. Rewriting Eq. 4.28 using Eq. 4.21, we get

$$\begin{pmatrix} 1 & \frac{1-\beta}{\beta} \end{pmatrix} \begin{pmatrix} B_4^{(1)} \\ B_4^{(2)} \end{pmatrix} = \begin{pmatrix} 1 & \frac{1-\beta}{\beta} \end{pmatrix} M^3 \begin{pmatrix} 1 \\ -1 \end{pmatrix} = 0; \quad M = \begin{pmatrix} -1 & -\frac{1}{\beta} \\ 1 & \frac{1-\beta}{\beta} \end{pmatrix} \tag{4.29}$$

Solving Eq. 4.29 for β yields three possible solutions: $\beta_1 = 0.382$, $\beta_2 = 0.276$, and $\beta_3 = 0.724$. Additional constraints are required to determine which of the valid β is representative of the heterojunction in question. First, we will need to solve for the decay length on the 7-AGNR side of the junction.

For the 7-AGNR side of the interface, we have a zigzag' terminating unit cell with the zero-mode being polarized to the sublattice associated with the terminal carbon atoms. The amplitude of the wavefunction in the first and second column of carbon atoms in the interfacial unit cell are $C_i^{(1)}$ and $C_i^{(2)}$ with an added factor of β^{k-1} for the kth unit cell beyond the terminal unit cell. Following the same rationale for the previous zero-mode states, these amplitudes are constrained as follows:

$$C_1^{(2)} = -\beta C_1^{(1)} \tag{4.30}$$

$$C_{i+1}^{(1)} = -C_i^{(1)} - C_i^{(2)} \tag{4.31}$$

$$C_{i+1}^{(2)} = -\beta C_{i+1}^{(1)} - C_i^{(2)} = \beta C_i^{(1)} + (\beta - 1) C_i^{(2)} \tag{4.32}$$

Eq. 4.31 and 4.32 can be written as a matrix equation

$$\begin{pmatrix} C_{i+1}^{(1)} \\ C_{i+1}^{(2)} \end{pmatrix} = M \begin{pmatrix} C_i^{(1)} \\ C_i^{(2)} \end{pmatrix}; \quad M = \begin{pmatrix} -1 & -1 \\ \beta & \beta - 1 \end{pmatrix} \tag{4.33}$$

Eq. 4.33 tells us

$$\begin{pmatrix} C_3^{(1)} \\ C_3^{(2)} \end{pmatrix} = M^2 \begin{pmatrix} C_1^{(1)} \\ C_1^{(2)} \end{pmatrix} \tag{4.34}$$

Without loss of generality, we can set $C_1^{(1)} = 1$. Again applying boundary conditions we get

$$\begin{pmatrix} \beta & \beta - 1 \end{pmatrix} \begin{pmatrix} C_3^{(1)} \\ C_3^{(2)} \end{pmatrix} = \begin{pmatrix} \beta & \beta - 1 \end{pmatrix} M^2 \begin{pmatrix} 1 \\ -\beta \end{pmatrix} = 0; \quad M = \begin{pmatrix} -1 & -1 \\ \beta & \beta - 1 \end{pmatrix} \tag{4.35}$$

Solving Eq. 4.35 for β yields one valid solution: $\beta_4 = 0.586$, which is the same value obtained for the 7-AGNR zigzag end state. Hence, the decay length of the topological interface on the 7-AGNR side of the heterojunction is known. The final step is then to derive the correct value for the decay length in the 9-AGNR section based on the three possible solutions derived previously.

In general, the zero-mode present at the 7/9-AGNR zigzag'/zigzag interface shown in Fig. 4.10A should be a linear combination of the four zero mode solutions derived in the preceding section (three on the 9-AGNR side and one on the 7-AGNR side):

$$|\psi_0\rangle = K_1|\psi_0^1\rangle + K_2|\psi_0^2\rangle + K_3|\psi_0^3\rangle + K_4|\psi_0^4\rangle \tag{4.36}$$

Where $|\psi_0^i\rangle$ is the zero-mode with the corresponding decay length β_i defined above. In order to determine the four linear weights K_i, we must derive four independent equations on K_i. The first of these is the normalization condition:

$$K_1^2 + K_2^2 + K_3^2 + K_4^2 = 1 \tag{4.37}$$

The remain three constraints come from boundary conditions at the junction interface that relate the wavefunction amplitudes on the 7-AGNR side of the interface to those on the 9-AGNR side of the interface. Once again, these follow from the constraint that the sum of all nearest neighbor amplitudes must add to zero:

$$C_1^{(1)} + B_1^{(1)} + B_2^{(1)} = 0 \tag{4.38}$$

$$C_2^{(1)} + B_2^{(1)} + B_3^{(1)} = 0 \tag{4.39}$$

$$C_3^{(1)} + B_3^{(1)} + B_4^{(1)} = 0 \tag{4.40}$$

$$C_3^{(1)} + B_3^{(1)} + B_4^{(1)} = 0 \tag{4.41}$$

The amplitude of the wavefunction on the ith atomic site on the 9-AGNR side of the interface $B_i^{(1)}$ can be written as a linear combination the three possible solutions:

$$B_i^{(1)} = K_1 B_{i,1}^{(1)} + K_2 B_{i,2}^{(1)} + K_3 B_{i,3}^{(1)} \tag{4.42}$$

where $B_{i,j}^{(1)}$ is the amplitude of the jth solution on the ith atomic site. Similarly

$$C_i^{(1)} = K_4 C_{i,4}^{(1)} \tag{4.43}$$

Thus, Eq. 4.42 and 4.43 can be used to rewrite the constraints of Eq. 4.38 – 4.41 in terms of the four linear weights K_i:

$$K_4 C_{1,4}^{(1)} + K_1(B_{1,1}^{(1)} + B_{2,1}^{(1)}) + K_2(B_{1,2}^{(1)} + B_{2,2}^{(1)}) + K_3(B_{1,3}^{(1)} + B_{2,3}^{(1)}) = 0 \tag{4.44}$$

$$K_4 C_{2,4}^{(1)} + K_1(B_{2,1}^{(1)} + B_{3,1}^{(1)}) + K_2(B_{2,2}^{(1)} + B_{3,2}^{(1)}) + K_3(B_{2,3}^{(1)} + B_{3,3}^{(1)}) = 0 \tag{4.45}$$

$$K_4 C_{3,4}^{(1)} + K_1(B_{3,1}^{(1)} + B_{4,1}^{(1)}) + K_2(B_{3,2}^{(1)} + B_{4,2}^{(1)}) + K_3(B_{3,3}^{(1)} + B_{4,3}^{(1)}) = 0 \tag{4.46}$$

$$K_4 C_{4,4}^{(1)} + K_1(B_{4,1}^{(1)} + B_{5,1}^{(1)}) + K_2(B_{4,2}^{(1)} + B_{5,2}^{(1)}) + K_3(B_{4,3}^{(1)} + B_{5,3}^{(1)}) = 0 \tag{4.47}$$

Since all $B_{i,j}^{(1)}$ and $C_{i,j}^{(1)}$ are known based on the solutions derived in the preceding section, further applying the constraints from Eq. 4.37 and Eq. 4.44-4.47 determines all K_i : $K_1 \approx 0$, $K_2 \approx 0.04$, $K_3 \approx 0.72$, and $K_4 \approx 0.70$. Hence, the characteristic decay length on the 9-AGNR is predominantly defined by β_3 which is greater than β_4 on the 7-AGNR side of the interface. Therefore, the topological interface state extends further into the 9-AGNR side than the 7-AGNR side. It is worth emphasizing at this point that at no point are the intrinsic gaps of the host GNRs invoked to determine the decay lengths on either side of the 7/9-AGNR junction. These were determined purely by the specific bonding geometry of the interfacial region along with the sublattice to which the zero-modes are polarized.

Finally, it is instructive to consider a counterexample for which the topological interface state at a 7/9-AGNR heterojunction possesses a larger decay length in the 7-AGNR region compared to the 9-AGNR region. To demonstrate the importance of the interfacial boundary conditions, we consider another zigzag'/zigzag 7/9-AGNR interface where the registry is shifted compared to that shown previously (Fig. 4.10(B)). Here, the linear weights K_i shift significantly: $K_1 \approx 0.36$, $K_2 \approx -0.25$, $K_3 \approx -0.34$, and $K_4 \approx 0.83$. The net result is a

topological interface state that decays more rapidly in the 9-AGNR section compared to the 7-AGNR section. In principle, GNR TQDs constructed with these alternative junctions would have a larger hoping parameter across the 7-AGNR sections than the 9-AGNR sections.

One can also consider scenarios in which the interfacial bonding geometry and boundary conditions conspire to completely localize topological interface states to the 7-AGNR side of a 7/9-AGNR junction (Fig. 4.10(C),(D)). GNR TQDs constructed from these elements would essentially have a vanishing wavefunction amplitude across the 9-AGNR segment while maintaining a non-zero wavefunction amplitude across the 7-AGNR segment.

Thus, the topological end states found at zigzag termini of 7-AGNRs and 9-AGNRs have the opposite behavior, with the shorter decay length being found in the small band gap 9-AGNRs (Fig. 4.9(A–C)). Furthermore, if the registry of the zigzag'/zigzag 7/9-AGNR interface is shift laterally, the resultant topological interface state will decay more rapidly on the 9-AGNR side of the interface compared to the 7-AGNR side (Fig. 4.10(A),(B)). The above approach reveals that the decay lengths of topological zero-mode states do not depend on the bulk band gap of the host GNR, but are instead determined by the interfacial geometry and the sublattice on which the topological zero-mode resides. Indeed, these structural factors can even conspire to completely localize topological interface states on the 7-AGNR side of a 7/9-AGNR heterojunction (Fig. 4.10(C),(D)).

4.4 Conclusion

We have developed an explicit protocol for generating rationally designed bottom-up GNR quantum dots based on topological boundary states, resulting in QD states of tunable hybridization and symmetry. The sterically-selective on-surface copolymerization strategy used in this work allows for the development of new GNR heterojunctions with customized interfacial geometries and tailored segment-lengths through use of a bifunctional linker. We also demonstrate the ability to generate interfacial zero modes between GNRs derived from synthetically orthogonal molecular precursors using this specialized linker monomer. These results show that zero-dimensional topological states embedded in GNRs provide a new platform for investigating quasi-1D topological behavior and quantum magnetism, and thus create new opportunities for future nanoelectronics applications including sensors, transistors, and qubits.

Chapter 5

Engineering Robust Metallic Zero-Mode States in Olympicene Graphene Nanoribbons

Metallic graphene nanoribbons (GNRs) represent a critical component in the toolbox of low-dimensional functional materials technology serving as 1D interconnects capable of both electronic and quantum information transport. The structural constraints imposed by on-surface bottom-up GNR synthesis protocols along with the limited control over the orientation and sequence of asymmetric monomer building blocks, as shown in the sawtooth GNRs plagued the design and assembly of metallic GNRs. In this chapter, we introduce a new type of GNR hosting robust metallic states by embedding a symmetric zero-mode superlattice along the backbone of a GNR. Tight-binding electronic structure models predict a strong nearest-neighbor electron hopping interaction between adjacent zero-mode states resulting in a dispersive metallic band. First principles DFT-LDA calculations confirm this prediction and the robust, metallic zero-mode band of olympicene GNRs (oGNRs) is experimentally corroborated by scanning tunneling spectroscopy.

5.1 Introduction

Graphene nanoribbons (GNRs) are representatives of an emerging class of bottom-up synthesized designer quantum materials whose electronic structure can be tuned with atomic precision by deterministic chemical design. Their structures exhibit unusual and some never before realized physical properties that extend far beyond the parent 2D graphene. Highly tunable band gaps,[33][72][35] photoemission,[92] magnetic spin chains,[93] and even symmetry-protected topological states[1][37][38][39] can all be tailored by real space structural parameters including among others width, symmetry, edge termination, and substitutional doping.[74][36][94][7] A dominant electronic feature common to almost all GNRs is the opening of a sizeable band gap imposed by laterally confining 2D graphene sheets to a quasi-1D GNR (width < 2 nm). This quantum confinement effect has emerged as a veritable challenge to the design of intrinsically metallic band structures. Bottom-up access to a family of robust metallic GNRs not only represents a critical component in the de-

velopment of advanced nanographene-based logic circuits,[95] e.g. as covalent inter-connects capable of electronic and quantum transport, but could serve as a versatile and highly tunable platform to explore emergent physical phenomena such as Luttinger liquids,[55][56][57][96] plasmonics,[58][97][59][98] charge density waves,[60][61][99][100] and superconductivity in 1D.[101][102][62][63]

We recently reported a general approach for accessing metallic GNRs by embedding a superlattice of localized zero-mode states along the backbone of a bottom-up synthesized sawtooth GNR (sGNR).[2][84] A key ingredient to this approach was the design of a molecular building block, 6,11-bis(10-bromoanthracen-9-yl)-1-methyltetracene (BAMT in Fig. 5.1), that introduces a sublattice imbalance ($\Delta N = N_A - N_B$) between carbon at-oms occupying the A and the B sublattice sites of graphene, respectively. The concept is reminiscent of Lieb's theorem,[47] a surplus of carbon atoms on sublattice A versus sublattice B will lead to ΔN eigenstates at $E = 0$ eV, or zero-modes, localized on the majority sublattice. Application of a simple tight-binding model, the Su-Schrieffer-Heeger (SSH) dispersion relationship,[103] that describe the interaction between these local zero-mode states gave rise to two distinctive bands defined by an intracell hopping amplitude t_1 and an intercell hopping amplitude t_2. The energy gap enclosed by these bands is $\Delta E = 2||t_1| - t_2||$. If the absolute magnitudes of the two hopping amplitudes are equal, i.e. $|t_1| = |t_2|$, as illustrated for the evenly spaced zero-mode states in sGNR (Fig. 5.1(A) the energy gap vanishes and the 1D electronic structure becomes metallic.[65][71] The presence of a metallic zero-mode band at the Fermi level (E_F) in sGNRs could be visualized by scanning tunneling spectroscopy (STS) and was further corroborated by DFT-LDA calculations. This method, however, suffered from a Stoner-type instability for narrow bands that could open up a spin-splitting gap. To overcome this, we had to introduce an effective sublattice mixing (e.g. introduction of 5-membered-rings in 5-sGNRs) to facilitate the hopping between the localized zero modes.

A major shortcoming inherent to the design of 5-sGNRs is the requirement that all bonds formed between molecular precursors as part of the on-surface radical step-growth polymerization have to follow a strict head-to-tail pattern (-AB-AB-AB- in Fig. 5.1(A) to ensure the intracell hopping amplitude $|t_1|$ remains equal in magnitude to the intercell hopping amplitude $|t_2|$. The statistical probability that this specific arrangement is adopted for a single C-C bond-forming step on the surface is only ∼50%. Were the molecular building blocks to fuse in the undesirable head-to-head (-BA-AB-) or tail-to-tail (-AB-BA-) configuration the zero-mode bands would split ($|t_3| \neq |t_4|$) and give rise to a semiconductor rather than a metal.[2][84] The probability of producing a metallic sGNR segment from n monomers is therefore $P(n) = (0.5)^n$ or less than 1% for n > 7, severely limiting the use of metallic sGNRs at length scales necessary for applications as device interconnects. While sGNRs served as a successful proof-of-concept for our general approach to access metallic phases in GNRs, designs that ensure regioregularity and an efficient sublattice mixing of zero-mode states are needed to obtain uni-form samples of extended GNRs with persistent, intrinsically metallic zero-mode bands.

5.2 Experimental Result Summary

Samples of 5-oGNRs are synthesized via bottom-up techniques, Topographic images of a high and low coverage sample, Fig. 5.2(B) and Fig. 5.2(C), respectively, reveal extended GNRs featuring a characteristic alternating pattern of protrusions along the backbone of the GNR and lengths ranging up to 30 nm. Bond-resolved STM (BRSTM) with CO-functionalized tips reveals that following the initial radial step growth polymerization at 180 °C the [4]-helicene fragments lining the edges of oGNRs have partially fused to form 5-membered rings (Fig. 5.2(E)). The second annealing step (350 °C for 15 min) merely completes the process giving access to a uniform edge termination in 5-oGNRs (Fig. 5.2(D)). Having resolved the chemical structure of 5-oGNRs we shifted our focus to the characterization of its local electronic structure using differential tunneling spectroscopy. Fig. 5.3(A) shows typical dI/dV point spectra for a 5-oGNR recorded with a CO-functionalized STM tip at the positions highlighted in the inset. Three spectral features can clearly be seen in the range of $-2.00V < V_s < +1.80V$. Two shoulders at $V_s = +1.60V$ (Peak 1) and $V_s = -0.75V$ (Peak 3) dominate the spectrum, along with a broad peak centered at $V_s = -0.90V$ (Peak 2). The signal intensities of Peaks 1 and 3 are strongest when the STM tip is placed close to the convex protrusions lining the edge of the ribbon (blue line in Fig. 5.3(A)), whereas Peak 2 is prominently featured in both spectra recorded above the center of an olympicene unit (red line in Fig. 5.3(A)) and along the edge of the ribbon. Fig. 5.3(B) shows a magnification of the dI/dV spectra taken over a narrower bias range $-0.20V < V_s < +0.20V$. Most prominent here is a U-shaped feature anchored by two peaks in the differential conductance spectrum at $V_s = -0.10V$ and $V_s = +0.10V$ when the STM tip is placed above the center of the ribbon. Differential conductance maps recorded over a continuous bias range of $V_s = +0.10V$ to $V_s = -0.10V$ (Fig. 5.3(D-J)) show that the same state, associated with a distinctive wavefunction pattern of a zero-mode, spans across E_F. The peak at $V_s = -0.10V$ can thus be assigned to the bottom edge of the lower (LZM) of two zero-mode (ZM) bands contributing to the metallic state in 5-oGNRs, while the peak at $V_s = +0.10V$ captures the top edge of the upper zero-mode (UZM) band. The U-shaped LDOS spanning across E_F is the signature of van Hove singularities associated with the flat band edges of the LZM and UZM bands.

5.3 First-principles Result of the 5-oGNR

We further explored the metallic band structure of 5-oGNRs using ab initio density functional theory (DFT). Fig. 5.3(M) and Fig. 5.3(N) show the theoretical DOS and the band structure of a 5-oGNR calculated using a local density approximation (LDA) to the exchange-correlation potential. Two highly dispersive bands, labeled LZM and UZM, span across the energy scale from $E - E_F = -0.25eV$ to $E - E_F = 0.25eV$. The LZM and UZM bands cross E_F at $k = X$ giving rise to a robust metallic band with a width of EZM $\sim$ 0.5 eV. Both the upper and lower edges of the ZM bands show a flattening as they approach $k = \Gamma$. The corresponding calculated DOS (Fig. 5.3(M)) faithfully reproduces the U-shaped signature of the metallic band identified in the experimental LDOS (Fig. 5.3(A),(B)). DFT-LDA LDOS maps evaluated at the energy position of the UZM and LZM

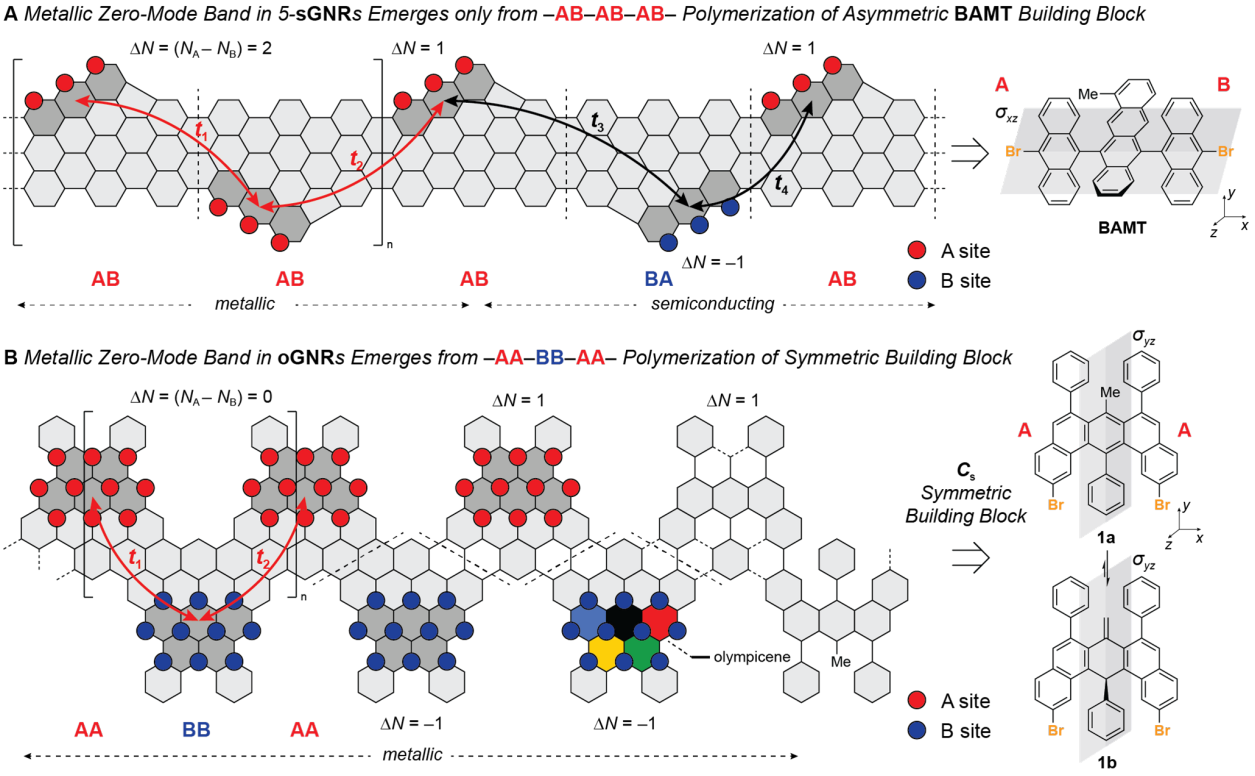

Figure 5.1: Bottom-up design and zero-mode engineering of metallic GNRs. (A) The metallic band in 5-sGNRs emerges only if the orientation of the monomers along the axis of polymerization (x-axis) follows a regioregular -AB-AB-AB- pattern. (B) The presence of a σ_{yz} mirror plane in 1a/b normal to the axis of polymerization (x-axis) ensures that either of two possible orientations of a monomer during the radical step-growth polymerization gives rise to a metallic zero-mode band in oGNRs.

edges (Fig. 5.3(P),(Q)) show the characteristic nodal pattern observed in the corresponding dI/dV maps (Fig. 5.3(D-J)). At energies above and below $E - E_F = \pm 0.25eV$ the calculated metallic ZMB gives way to mini-gaps, narrow regions of vanishing DOS that span the energy window separating the ZMB from the bottom of the CB and the top of the VB, located at $E - E_F = 0.80eV$ and $E - E_F = -0.75eV$, respectively. Both LZM and UZM bands can be fit to an SSH tight-binding model

$$E_{\pm}(k) = \pm\sqrt{|t_1|^2 + |t_2|^2 + 2|t_1||t_2|\cos(k+\delta)} \tag{5.1}$$

with the intra- and intercell hopping amplitudes $|t_1| = |t_2| = 111meV$, and $\delta = 0$ (δ is the relative phase between t_1 and t_2). Supercell calculations further show that the rigid GNR backbone renders oGNR virtually impervious to mechanical deformations usually associated with strong electron-phonon coupling along the main x-axis of the ribbon that would otherwise induce spontaneous metal-insulator transitions (i.e. Peierls distortion). Besides the decisive structural advantage over the first generation metallic sGNRs, the Cs symmetric molecular precursor 1b features a σ_{yz} mirror plane perpendicular to the axis of polymer-

ization that gives rise to uniformly predictable monomer sequences that exclusively yield metallic band structures, the family of oGNRs has one last trick up its sleeve.

Unlike sGNRs, where a fusion of the [4]helicene fragment along the sawtooth edge proved critical to induce mixing of the sublattice spin-polarized zero-mode states that led to a broadening of the metallic ZMB (i.e. a reduced DOS at E_F) sufficient to circumvent Mott insulator or Stoner magnetic phase transitions, an efficient hopping between zero-mode states localized on A and B sites in oGNRs is built into our design. The -AA-BB-AA- polymerization places zero-mode states on alternating sublattice sites ensuring that the hopping amplitudes t_1 and t_2 between adjacent states are dominated by the nearest neighbor hopping term rather than the much smaller second nearest neighbor hopping (Fig. 5.1(B). This is reflected in band structure calculations using the local spin density approximation (LSDA) that show no sign of magnetic phase transitions for the disperse metallic ZM bands in 5-oGNRs (Fig. 5.4).

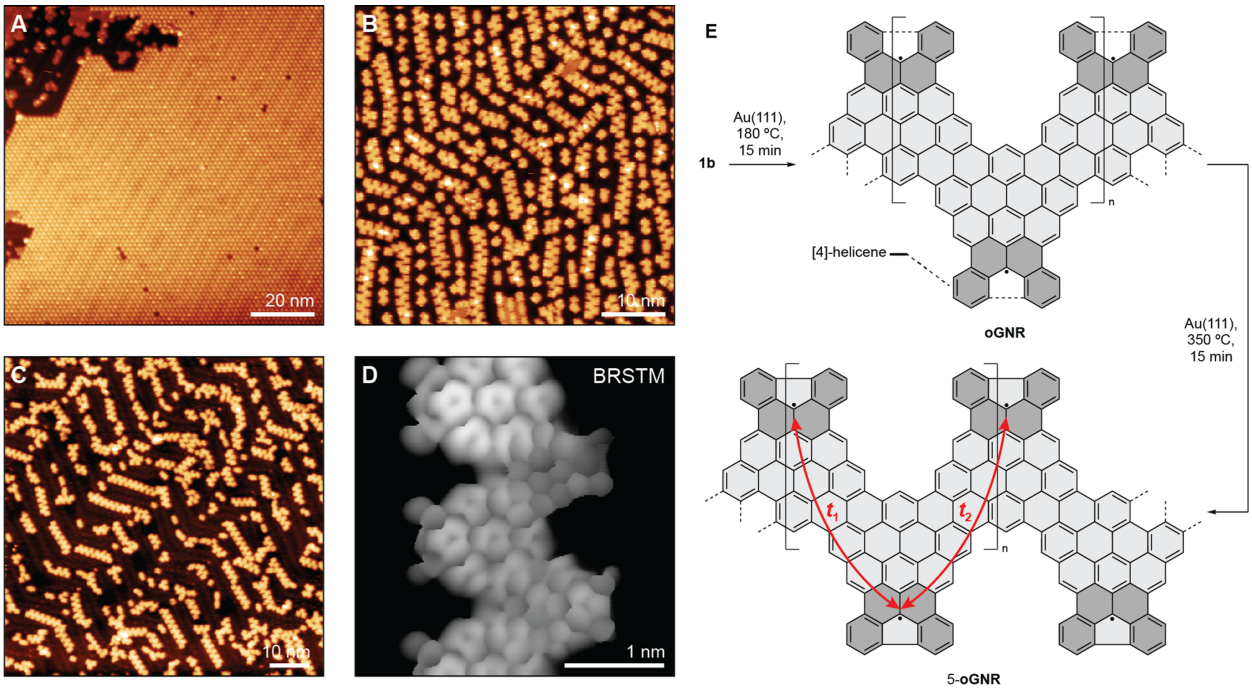

Figure 5.2: Bottom-up synthesis of 5-oGNRs. (A) STM topographic image of a self-assembled island of molecular precursor 1b on Au(111) ($V_s = 0.05V$, $I_t = 20pA$). (B) STM topographic image of a high coverage sample of 5-oGNRs following annealing to 350 °C ($V_s = 0.05V$, $I_t = 20pA$). (C) STM topographic image of a low coverage sample of 5-oGNRs following annealing to 350 °C ($V_s = 0.05V$, $I_t = 20pA$). (D) BRSTM image of a 5-oGNR segment showing the 5-membered rings resulting from the fusion of [4]helicene groups along the oGNRs edges ($V_s = 0.01V$, $I_t = 400pA$). (E) Schematic representation of the stepwise thermally induced cyclodehydrogenation that gives rise to 5-oGNRs.

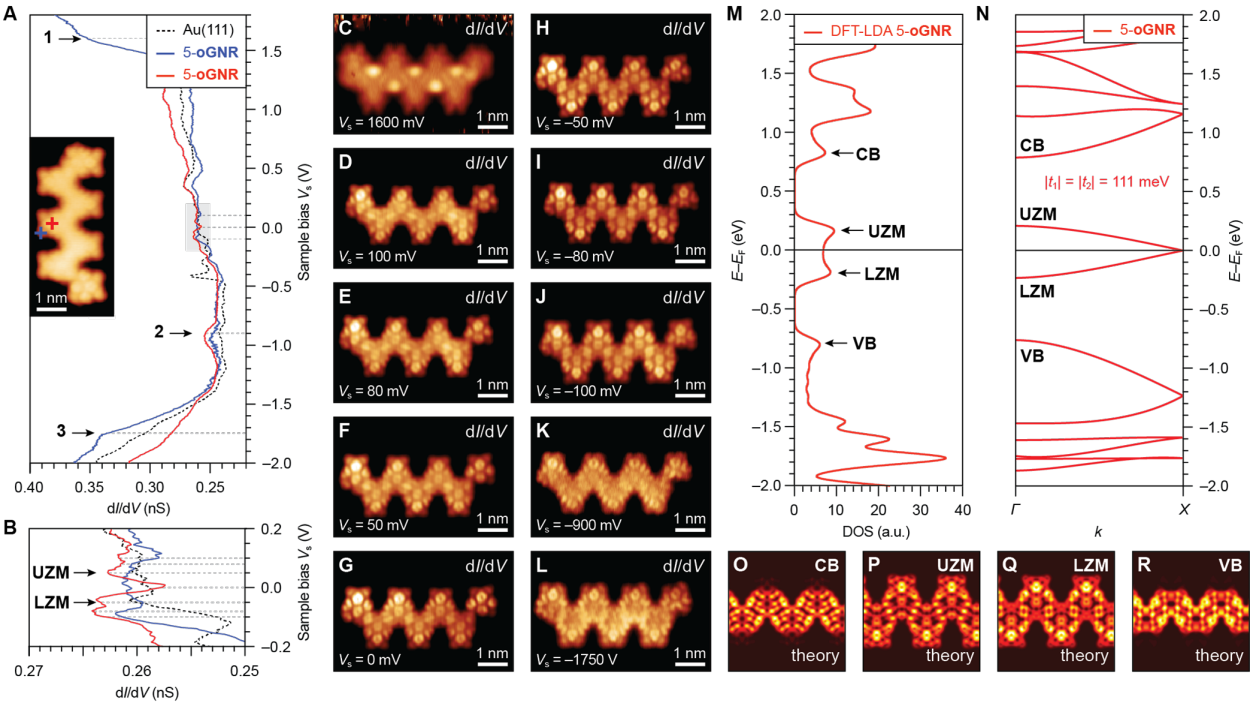

Figure 5.3: Electronic structure of 5-oGNRs. (A-B) STS dI/dV spectra recorded on a 5-oGNR at the positions marked in the inset STM topo-graphic image with a red and blue cross (spectroscopy: $V_{ac} = 11mV$, f = 455 Hz; imaging: $V_s = 50mV$, $I_t = 20pA$, CO-functionalized tip). (C-L) Constant height dI/dV maps recorded at the indicated biases (spectroscopy: $V_{ac} = 11mV$, f = 455 Hz). (M) DFT-LDA calculated DOS of 5-oGNR (spectrum broadened by 10 meV Gaussian). Features associated with the CB, UZM, LZM, and VB are indicted by arrows. (N) DFT-LDA calculated band structure of a freestanding 5-oGNRs. A tight binding fit to DFT-LDA band structure yields the hopping parameters $|t_1| = |t_2| = 111meV$. (O-R) Calculated DFT-LDA LDOS maps evaluated at the edge of the bulk conduction band, at the UZM and LZM bands, and at the edge of the bulk valence band.

5.4 Conclusion

We herein demonstrate the versatility of zero-mode engineering for introducing robust metallicity in 1D GNRs. A Cs symmetric molecular building block undergoes a regiocontrolled on-surface polymerization to yield homogenous samples of 5-oGNRs featuring a symmetric super-lattice of zero-mode states along the GNR backbone. Guided by elementary tight-binding analysis we pioneer the design of 5-oGNRs around a strong nearest-neighbor hop-ping interaction between electrons in adjacent zero-mode states giving rise to a large zero-mode bandwidth that is insensitive to Peierls and Stoner metal-insulator transitions. First-principles DFT-LDA calculations and scanning tunneling spectroscopy corroborate the emergence of metallic zero-mode bands in 5-oGNRs. The design and synthesis of robust, metallic GNRs paves the way towards the realization of energy-efficient integrated circuit

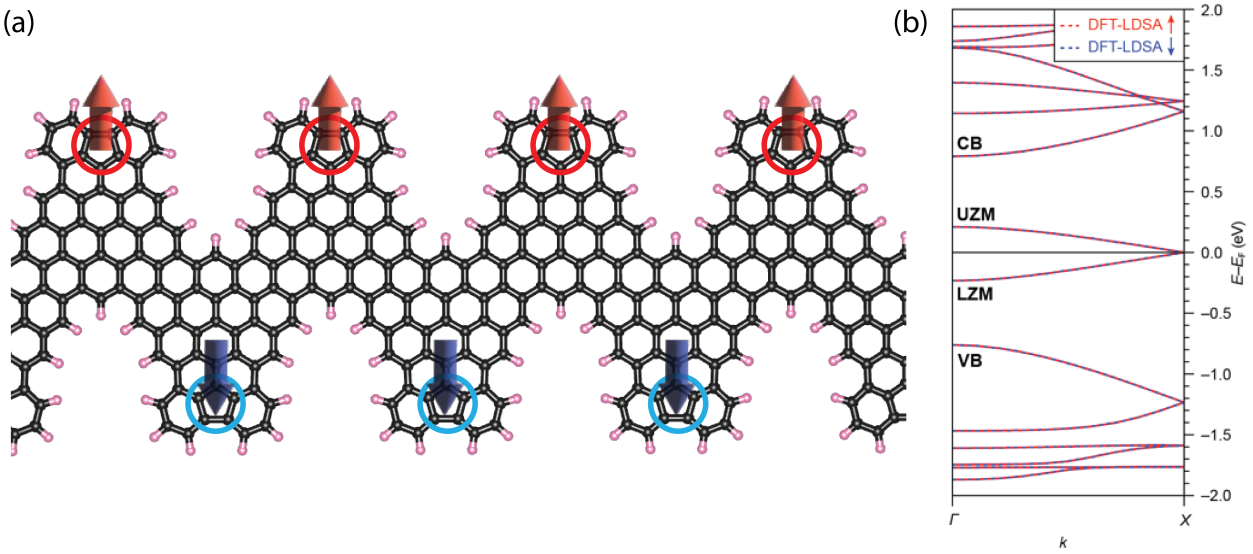

Figure 5.4: (a) The proposed anti-ferromagnetic states in the DFT-LSDA calculation, this configuration is set as the initial condition for the magnetization. (b) The converged DFT-LSDA calculated band structure for 5-oGNRs shows the same ground state as in LDA calculation. Even though Lieb's theorem does not rule out the possibility of antiferromagnetic ordering, the large overlap between adjacent zero-mode states favors a non-magnetic ground state in oGNRs. The magnetic property shown in (a) is absent after the convergence.

architectures based on low-dimensional carbon materials that are capable of high-speed electronic[104][105] and quantum information processing.[106][107]

Chapter 6

Non-Hermitian Topology Induced Unidirectional Electron Transport in Graphene Nanoribbons

We show that a 4-armchair graphene nanoribbon with cobalt (Co) adatoms (Co-4AGNR) manifests non-Hermitian topology. The non-Hermitian nature arises from the self-energy of the quasiparticle states due to many-electron interactions. Spin-orbit coupling of the Co atoms breaks symmetries that map states from k to -k, which is necessary for nontrivial topology. The complex-energy bands of the periodic system from ab initio *GW* calculations yield non-trivial Z indices – first such realization in an electronic material. The Green's function of a segment exhibits strong asymmetric behavior in real space, giving rise to novel unidirectional transport properties.

6.1 Introduction

Topological classification in non-Hermitian systems is significantly different from their Hermitian counterparts [108][109]. It has triggered much interest recently in optical systems [110] and other open systems [111][112]. A distinct phenomenon is the non-Hermitian "skin effect" (NHSE) in topological one-dimensional (1D) non-Hermitian systems where a macroscopic number of wavefunctions localize at one end of a finite segment [113][114]. However, this phenomenon has not been realized in realistic electronic condensed matter systems so far. Graphene nanoribbons (GNRs), a 1D crystalline material [35][36] that could be synthesized with atomic precision [33]-[34], have attracted many interests for their fundamental properties and potential applications. Recently, GNRs have been proven to possess nontrivial topology [37] when time-reversal and inversion symmetries are present in a unit cell commensurate with the geometry of its termination, based on Hermitian topology classification theory. The topological states in the bulk gap at the junction of two GNRs of distinct topologies have been predicted to have novel properties and promising applications[37]-[64], and many of them have been realized in experiments[4][38][7][8]. A generalization to classification theory using chiral symmetry [1] further explains the formation of asymmetric junction topological states [39][2][3] and predicts the spin physics in the GNRs.

Previous topological theories for electronic systems, such as those above for the GNRs, are basically restricted to systems in which the electronic states are assumed to be derived from a Hermitian Hamiltonian. However, in many experiments and situations such as scanning tunneling microscopy (STM), angle-resolved photoemission spectroscopy (ARPES), etc., the spectral and transport data measured correspond to quasiparticle excitations that may have a significant finite lifetime due to many-body interactions; this gives rise to an imaginary part to the quasi-particle energy. When such many-body effect is considered, the Dyson's equation for the quasiparticle states may be mapped to an effective Hamiltonian that is naturally non-Hermitian; it falls into the class of non-Hermitian 1D classification and an analysis of its topological properties may lead to discovery and deeper understanding of interesting novel phenomena. Here we perform ab initio GW calculations [22] on an armchair graphene nanoribbon (AGNR) with width of four carbon rows (4AGNR) and a cobalt atom on top in each unit cell (Fig. 6.2(a)), and find that the Co-4AGNR manifests a nontrivial non-Hermitian topology at point gaps (described below) for electronic states near the Fermi energy (E_F). We further construct a tight-binding Hamiltonian based on parameters obtained from Wannierization of the GW results, and unveil the NHSE for finite segments of the Co-4AGNR. As an important consequence, this effect makes the electronic Green's function $G(r, r', \omega)$ of the system asymmetric in real space. Many physical quantities such as transport coefficients and tunneling amplitude are proportional to the magnitude of the off-diagonal part of the real-space Green's function. The asymmetric Green's function causes the electron transport unidirectional, making the material acts as an ideal 1D "p-n" junction or diode. A key factor and a necessary condition behind this novel phenomenon is the broken symmetries (time-reversal symmetry, spatial symmetry, spin-rotational symmetry, etc.) resulted from the ferromagnetic order and spin-orbit coupling (SOC) effect induced by the cobalt atoms.

6.2 Non-Hermitian Topology Classification Theory

For a 1D electronic system with no symmetry, the non-Hermitian classification yields a Z index, rather than the trivial classification in the Hermitian case [108][109]. The distinct properties of a non-Hermitian topological 1D system can be seen from a simple example of a linear chain with one site per unit cell, known as the Hatano-Nelson model [115][116]:

$$H_{HN} = \sum_i t_1 c_{i+1}^\dagger c_i + t_2 c_{i-1}^\dagger c_i \tag{6.1}$$

Here i denotes the atomic site, $t_1 = t + g$ is the forward hopping amplitude, and $t_2 = t - g$ is the backward hopping amplitude (Fig. 6.1(a)). Both t and g are real numbers. For $g \neq 0$, the Hamiltonian is non-Hermitian. If periodic boundary condition is imposed, the spectrum can be obtained by doing a Fourier transform and solving for the eigenenergies of the system in the reciprocal (k) space. The spectrum (the complex eigenvalue as a function of wavevector k, $E(k)$) forms a closed path in the complex energy plane, as shown as the black curve in Fig. 6.1(b). However, the numerical solution for the spectrum E_i of a finite segment of this model is completely different, which are given by the red lines in Fig. 6.1(b) that form a line enclosed by the black curve. The difference between the finite segment spectrum

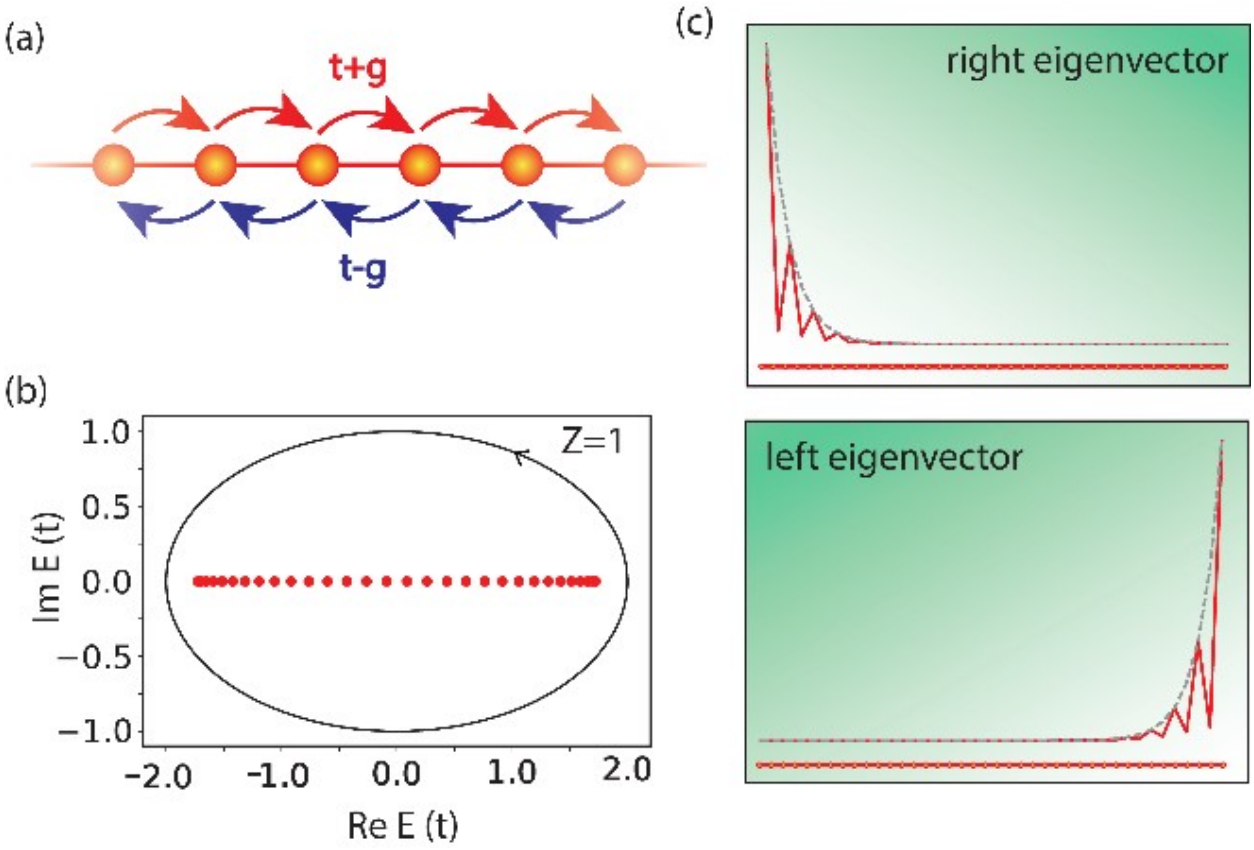

Figure 6.1: (a) Hatano-Nelson model with asymmetric hoppings between neighboring sites on a chain that make the Hamiltonian non-Hermitian. (b) Black curve: energy spectrum ($E(k)$) in the complex plane for $g/t = 0.5$ under periodic boundary conditions. E is in units of the hopping parameter t. Red dots: energy spectrum under open boundary conditions for a segment of 40 sites. (c) Example of right eigenvector and left eigenvector for the $E = -0.066t$ state of the non-Hermitian Hamiltonian in (a) of a segment of 40 sites. Both eigenvectors are localized on just one end of the finite chain.

and periodic one roots in the sensitive dependence of the quantum states on the boundary condition for a non-Hermitian system. All of the eigenvectors of a finite segment are localized on just one end of the chain, as shown in Fig. 6.1(c) for the right and left eigenvectors. The right eigenvector is defined as the wavefunction ψ_R that satisfies $H\psi_R = E\psi_R$, and the left eigenvector satisfies $\psi_L H = \psi_L E$. This phenomenon of macroscopic localization is known as the skin effect. In non-Hermitian classification theory for a 1D system with no symmetry, the Z index for a point gap is defined as a topological invariant for a chosen point E in the complex energy plane given by [117]-[118]:

$$Z = \int_{-\pi}^{\pi} \partial_k ln(det(H(k) - E)) \frac{dk}{2\pi i} \tag{6.2}$$

The physical meaning of the Z index is the winding number of the periodic spectrum,

as k goes across the 1D Brillouin zone (BZ) (e.g., from X to Γ and then from Γ to X) around a chosen energy E in the complex plane. Whenever the winding number is non-zero, the NHSE arises [119]. To have a nontrivial non-Hermitian topology like the one in the Hatano-Nelson model, we first would like to have an asymmetric bandstructure in DFT so that the real part of the energy is asymmetric. To achieve this, we have to break any symmetry that relates states at k to $-k$, such that the spectrum $E(k)$ for a given energy band goes along a different path in the complex energy plane as k goes from X to Γ, compared to the path as k goes from Γ to X in the BZ.To fulfill this requirement, we start with a 4-AGNR as a backbone, and add a cobalt atom in each unit cell as an adatom as shown in Fig. 6.2(a). Because GNRs can be synthesized with atomic precision, for example via the bottom-up molecular precursor method [72], this proposed material has the potential to be realized in the experiment. The cobalt atoms bring strong spin-orbit coupling (SOC) as well as ferromagnetism into the system, which breaks time-reversal symmetry, spatial symmetries, and collinear spin time-reversal symmetry defined as TS, where T is the time-reversal operator and S is the spin-flip operator. The symmetry breaking is a necessary but not sufficient condition to have an asymmetric bands, we searched for a variety of materials satisfying this requirement and found that this particular structure manifests an asymmetric bands under DFT, as shown in the following section.

6.3 Full Frequency GW Calculation

We first perform ab initio density functional theory (DFT) calculation on Co-4AGNR using the $QuantumESPRESSO$ package [17]. As was shown in Chapter 1, the Hamiltonian in DFT can be written as

$$H = T + V_{ion} + V_H + V_{xc}([n(r), \nabla n(r)]) \tag{6.3}$$

Here the exchange-correlation potential V_{xc} is given by the PBE approximation. We solved the Hamiltonian self-consistently to obtain the band structure, as shown in Fig. 6.2(b). The collinear LSDA result shows a ferromagnetic ground state, whereas noncollinear calculation with SOC already shows an asymmetric band structure at the DFT level (see band 1 and band 2 in Fig. 6.2(b)).

To include quasiparticle self-energy effects on top of the DFT energy bands, we perform a full frequency G_0W_0 calculation using the $BerkeleyGW$ package [22][23][23][24]. The quasiparticle Hamiltonian used in G_0W_0 calculation reads

$$H_GW(E) = T + V_{ion} + V_H + \Sigma(E) = H_{DFT} + (\Sigma(E) - V_{xc}) \tag{6.4}$$

Here $\Sigma(E)$ is the electron self-energy within the GW approximation, and the complex spectrum $E(k)$ is obtained by solving Dyson's equation:

$$H_{GW}(E)\psi = E\psi \tag{6.5}$$

Since the full frequency self-energy operator is non-Hermitian, the energies obtained from Eq. 6.5 have both real and imaginary parts. $Re(E(k))$ corresponds to the quasiparticle excitation energy, and $Im(E(k))$ is related to the lifetime of the quasiparticle excitation with

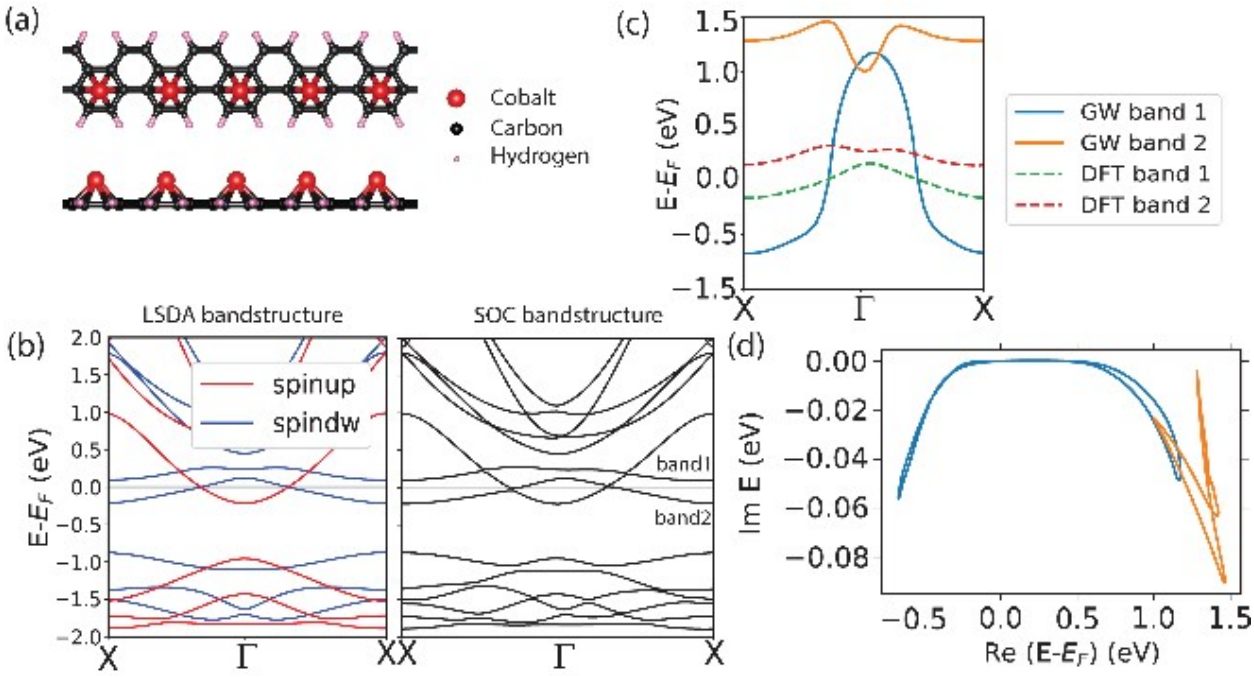

Figure 6.2: (a) Atomic structure of Co-4AGNR. The cobalt atoms are adsorbed at the center of the lower benzene rings. (b) DFT band structure in the local spin density approximation (left), and full-spinor DFT band structure including spin-orbit coupling (right). The SOC effect perturbs band 1 and band 2 and makes them asymmetric in k-space as shown on the right panel. (c) DFT bands (dashed lines) and real part of the full frequency GW bands (solid lines) of the two asymmetric bands near E_F shown in (b). (d) Complex spectrum of the full-frequency GW calculations of the two asymmetric bands in (c). The existence of some areas enclosed by the energy spectrum under periodic boundary conditions is indicative of nontrivial topology.

wavevector k in the BZ. Since performing a full frequency GW calculation for a 1D metallic system with full spinor wavefunctions is computationally challenging, we use wavefunctions from the collinear calculation instead and treat SOC as a perturbation. Fig. 6.2(c) shows the GW band structure (solid lines), i.e., the real part of $E(k)$ vs. k, as compared to the DFT band structure (dashed lines) for the two asymmetric bands identified in Fig. 6.2(b). Fig. 6.2(d) shows the complex spectrum of the two corresponding bands. Given that we have already broken all the symmetries to achieve asymmetry in the real component of energies, it is to be expected that the imaginary part of energies will also exhibit asymmetry. It is clear that the two bands have nontrivial non-Hermitian topology as they enclose some areas in the complex energy plane. From Eq. 6.2, we obtained $Z = -1$ and $Z = 1$ for any complex E inside the spectral loop of band 1 and band 2, respectively.

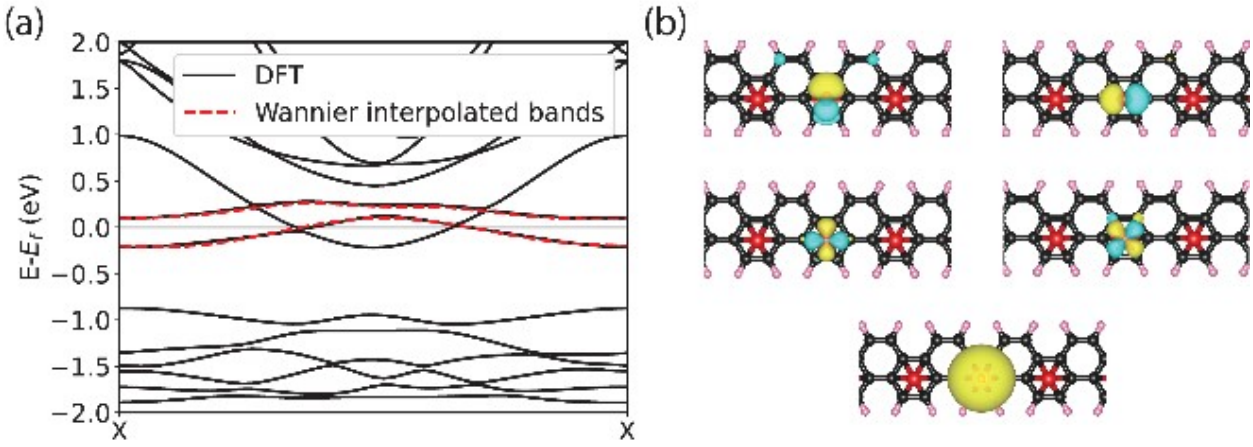

Figure 6.3: (a) Wannier interpolation of the two asymmetric bands of Co-4AGNR within DFT. Dashed lines are the Wannier interpolated bands and solid lines are the original DFT calculated bands, showing excellent agreement. (b) Isovalue plots (at value of 5%) of the five dominated Wannier functions (center around the cobalt atoms) for interpolating the two bands.

6.4 Finite Segment Spectrum

To explicitly show the properties of a large finite chain of Co-4AGNR, we first perform a Wannier interpolation [120] of the DFT band structure for the periodic system (Fig. 6.3(a)) and obtain its maximally-localized Wannier functions (Fig. 6.3(b)). We then use these Wannier functions as basis functions to construct a non-Hermitian tight-binding model Hamiltonian that fits our complex energy GW band structure using regression with $L2$ loss function:

$$L = \sum_{nk} |E_{nk}^{TB} - E_{nk}^{GW}|^2 \tag{6.6}$$

Here E_{nk}^{TB} is the eigenenergy obtained from the non-Hermitian tight-binding model, E_{nk}^{GW} is the complex eigenenergy from our ab initio GW calculation. After obtaining the tight-binding parameters, we apply the non-Hermitian tight-binding model to solve for the properties of the finite segments. The finite segment spectrum for a Co-4AGNR composed of 200 unit cells is shown in Fig. 6.4 (a). The dashed lines denote the eigenenergies of the finite segment and they are enclosed by the periodic spectrum (dark blue and orange lines). As a result of nontrivial non-Hermitian topology, the wavefunction of all the eigenmodes localizes on just one of the ends of the finite segment. (See Fig. 6.4(c)). With the solutions to Eq. 6.5, we may evaluate the single-particle Green's function for the electron that is given by:

$$G(r, r'; \omega) = \Sigma_i \frac{\psi_R^i(r)\psi_L^{i,*}(r')}{\omega - E_i} \tag{6.7}$$

$\psi_R^i(r)$ and$\psi_L^i(r)$ are the right and left eigenvector for the ith eigenenergy, respectively and E_i is the complex eigenenergy of the finite segment. The macroscopic localization of the wavefunctions of the finite segment leads to a distinct Green's function $G(l,m)$ matrix in real space, where l,m denote the unit cell index. As shown in Fig. 6.4 (b) for $\omega = 0.83eV$, since $Z = -1$, $\psi_R(r)$ localizes on the right end and $\psi_L(r)$ localizes on the left end. This makes $|G(\omega = 0.83eV, 200, 0)|^2$ several orders of magnitude bigger than $|G(\omega = 0.83eV, 0, 200)|^2$, as opposed to that of a Hermitian system in which the Green's functions are symmetric.

Transport of electrons, within a single-particle picture, at a given energy is in general proportional to the magnitude of the off-diagonal elements of the Green's function. According to the Buttiker formula[121], the transmission probability from the left lead to the right lead connected to a 1D segment is given by $T_{L\to R} = Tr[\Gamma(l_L)G(l_L, l_R)\Gamma(l_R)G^\dagger(l_R, l_L)]$ where l_L and l_R are unit-cell index of the left and right end of the finite segment, respectively, and Tr stands for tracing over a matrix. $\Gamma(l_{L/R})$ is the coupling matrix between the Co-4AGNR segment and the left/right leads, defined as $i(\Sigma(l_{L/R}) - \Sigma^\dagger(l_{L/R}))$. Here $\Sigma(l_{L/R}) = T_{L/R}g_{L/R}T_{L/R}$ is the self-energy of the lead, where $T_{L/R}$ is the hopping matrix between the lead and left/right end of the Co-4AGNR segment, and $g_{L/R}$ is the Green's function for the semi-infinite leads. The net transimission at energy E is proportional to $T_{L\to R}f_L(E) - T_{R\to L}f_R(E)$ where $f_{L/R}(E)$ is the Fermi distribution of the left/right leads. Since $|G(l_R, l_L)|^2$ is much larger than $|G(l_L, l_R)|^2$, the net current under positive bias ($f_L < f_R$) is much larger than that under negative bias ($f_R < f_L$). If Z changes from -1 to $+1$, the right eigenvectors would now localize on the left end of the finite segment and the preferred current direction would also be reversed. Thus, a finite segment Co-4AGNR manifests asymmetric conducting behavior, just like a p-n junction, despite the fact that the system has apparent mirror symmetry. The key here is that SOC (along with a ferromagnetic ground state) implicitly breaks this symmetry; this combining with the many-electron self-energy gives rise to the non-trivial non-Hermitian topology in this 1D material.

6.5 Conclusion

We propose a non-trivial non-Hermitian 1D system based on a graphene nanoribbon – a Co-4AGNR that possesses $Z = \pm 1$ winding numbers in the complex energy plane for energies near the Fermi level. In the finite segment form, its energy spectrum and eigenfunctions become vastly different from that of the periodic system. We explicitly show these findings by performing ab initio GW calculations including SOC and self-energy effects. The full-frequency GW calculation shows a non-trivial winding character for the Fermi-level bands of the periodic system, which leads to localization of the electron wavefunctions at one of the ends of a finite segment. A striking phenomenon predicted from our ab initio calculations is a large asymmetric electron transmission through the segment due to a distinct character of its electron Green's function matrix, leading to novel unidirectional transport properties. This work demonstrates that nontrivial non-Hermitian topology and NHSE may be achieved in practical electronic material systems, and paves a new way for the design of unidirectional transport properties in 1D materials at the nanoscale.

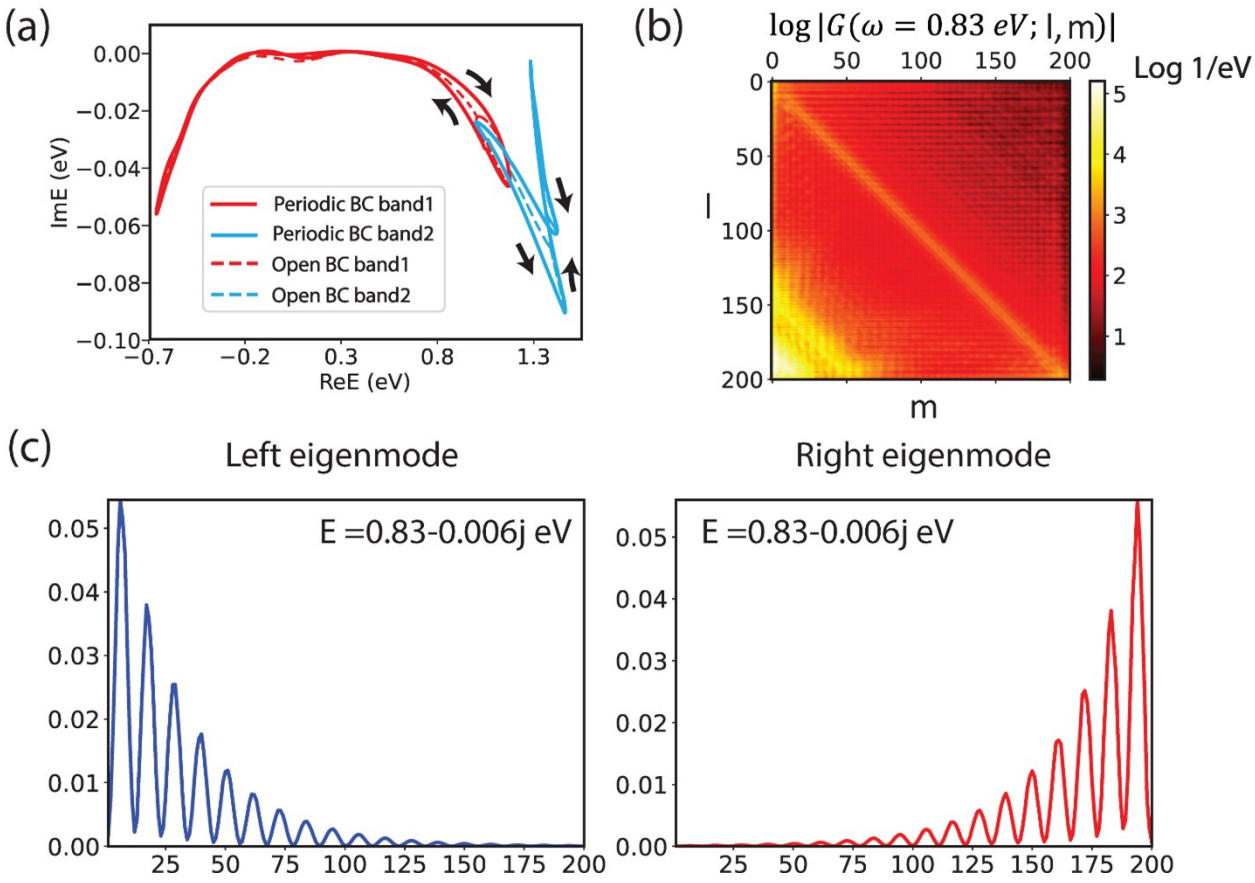

Figure 6.4: (a) Dark blue and orange lines are Wannier interpolated GW complex bands of Co-4AGNR with periodic boundary conditions for the two asymmetric bands in Fig. 6.2(d). The dashed red and light blue lines are the finite segment spectra. (b) The logarithm of the absolute amplitude of the Green's function matrix as a function of the unit-cell site positions is shown for a finite segment with 200 unit cells for energy $\omega = 0.83eV$. (c) Squared norm of the left and right eigenmodes of the non-Hermitian finite segment tight-binding Hamiltonian at eigenenergy of $0.83 - 0.006j$ eV. Since $Z = -1$ at this energy, the right eigenmode is localized at the right end of the finite segment and the left eigenmode is localized at the left end.

Chapter 7

Bottom-up Assembly of Nanoporous Graphene with Emergent Electronic States

The incorporation of nanoscale pores into a sheet of graphene allows it to switch from an impermeable semimetal to a semiconducting nano-sieve. Nanoporous graphenes are desirable for applications ranging from high-performance semiconductor device channels to atomically thin molecular sieve membranes, and their performance is highly dependent on the periodicity and reproducibility of pores at the atomic level. Achieving precise nanopore topologies in graphene using top-down approaches has proven to be challenging due to poor structural control at the atomic level. Alternatively, atomically precise nanometer-sized pores can be fabricated via lateral fusion of bottom-up synthesized graphene nanoribbons. Here we utilize the bottom-up approach to synthesize novel nanoporous graphene. We find emergent interface-localized electronic states within the bulk band gap of the graphene nanoribbon that hybridizes to yield a dispersive two-dimensional low-energy band of states. The low energy states give rise to an effective distorted super-graphene. We also show that this low-energy band can be rationalized in terms of edge states of the constituent single-strand nanoribbons. The localization of these 2D states around pores makes this material particularly attractive for applications requiring electronically sensitive molecular sieves.

7.1 Introduction

Nanoporous graphene (NPG) is unique in that it exhibits both electronic functionality as a tunable semiconductor and mechanical functionality as a tunable molecular filter membrane. Combining these properties into a single atomically-thin and robust platform makes NPG an excellent candidate for electronically active nanosieve applications such as sequencing, sensing, ion transport, gas separation, and water purification.[122]-[123] The utility of this material, however, hinges on the ability to induce periodic, atomically-precise nanopores and to tailor their precise dimensions and electronic properties. Top-down methods have so far been limited in this regard because they typically produce random, imprecise pores within a material that remains semimetallic.[122][124][125] By contrast, bottom-up

approaches offer atomic precision in NPG synthesis through rational design of molecular precursors.[126][127] This has been demonstrated recently through cross-dehydrogenative coupling of bottom-up synthesized graphene nanoribbons (GNRs) featuring periodic bay regions along the edges.[126][128]-[129] A disadvantage of the few reported bottom-up synthesized NPGs fabricated in this way is that the constituent nanoribbons are wide gap semiconductors. Electronic coupling upon lateral extension results in, at most, a modest decrease in the overall band gap compared to that of the constituent one-dimensional (1D) ribbons. In addition, the linkages between ribbons up to now are unable to host low-energy frontier states around the pores as required for possible electronic sieving applications.

Here we present a surface-mediated approach to creating NPG by utilizing a novel crosslinking handle that yields a fully conjugated linkage between constituent nanoribbons and results in a new low-energy band of extended states but with much of their wavefunctions localized along the periphery of the pores. We have designed two molecular precursors (1 and 2 in Scheme 1) functionalized with thermally labile methyl and methylene groups that serve as crosslinking handles. The respective C–H bond dissociation energies (BDE) are similar to that of the C_{aryl}–H bond cleaved during the thermally induced cyclodehydrogenation of the GNR backbone.[130] The geometry of these chevron-type precursors defines the pore shape and size whereas the reactivity of the crosslinking handles allows for the formation of benzene-fused linkages and facilitates two-dimensional extension of the structure. Our approach is high-yielding and selectively produces rubicene-type interfaces (highlighted in red in Scheme 1) by laterally fusing benzene rings through 5-membered rings along either side of an extended acene. The resulting NPG features interface-localized frontier electronic states that emerge upon formation of these interfaces. The emergence of these states can be understood as linear combinations of molecular orbitals localized on the 5-membered rings lining the edges of fluorene-chevron GNRs that couple into a two-dimensional (2D) superlattice geometry. We have experimentally characterized these electronic features using STS for both the final fused 2D nanopore states as well as isolated 5-membered-ring localized states in 1D fluorene-chevron GNRs. The novel crosslinking handle utilized here represents progress toward creating electronically useful NPG, thus opening the door to exploring its potential in nanosieving and semiconductor device applications.

7.2 Experimental Result Summary

To resolve the atomic structure of this C-NPG, we performed bond-resolved scanning tunneling microscopy (BRSTM) using a carbon monoxide-passivated tip.[79][131][132] Fig. 7.2(D) shows the BRSTM image of three interconnected ribbons over a 4 nm × 4 nm area. The ribbons are fused by rubicene-type linkages giving rise to a nanoporous structure containing parallelogram-shaped pores that are $\sim$ 0.5 nm wide in the short direction and $\sim$1 nm wide in the long direction. The orientation of the pores shown in Fig. 7.2(D) alternates, resulting in a herringbone pattern with a unit cell that has screw symmetry in the ribbon axis. In the following discussion this lateral fusion pattern will be referred to as anti. An alternative coupling yielding aligned pores with inversion symmetry points in the ribbon axis will be referred to as syn. A higher-resolution BRSTM image around one of the interfaces in the anti-configuration provides an unambiguous assignment of the covalent bond

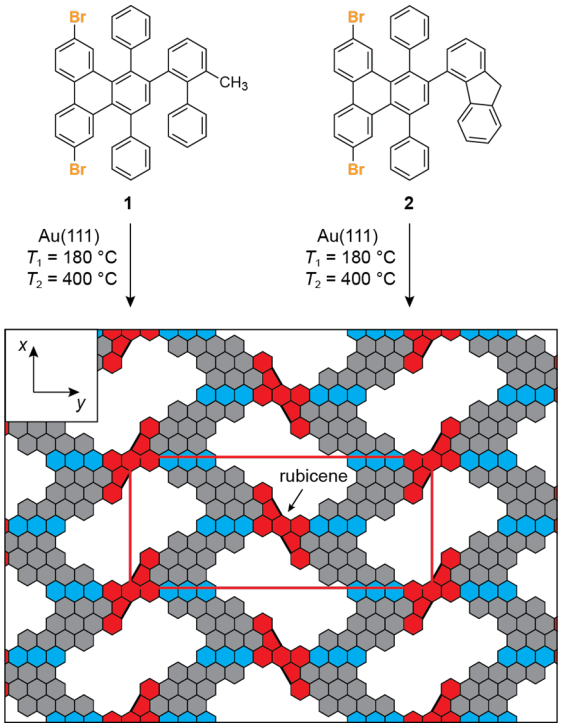

Figure 7.1: The structures of molecular precursors 1 and 2 functionalized, respectively. Deposition of precursors 1 or 2 onto a Au(111) surface held at $T_1 = 180$ °C and subsequent annealing to $T_2 = 400$ °C yields two-dimensionally extended chevron-type nanoporous graphene (C-NPG).

structure of the lateral fusion product leading to C-NPG. The interface originates from a cross-dehydrogenative coupling that leads to the formation of two new C–C bonds that define the central benzene ring of the rubicene core (highlighted in red in Fig. 7.2(F)). Another motif that emerges from the lateral fusion is a nonacene core where the newly created benzene ring represents the central ring (highlighted in blue in Fig. 7.2(F)).[133] The fusion process ensures that carbon atoms at the apices of the five-membered rings adopt a trigonal planar conformation, thus contributing a singly occupied p-orbital to the aromatic framework.

7.3 Electronic Structures of Nanoporous Graphene

Having established the chemical structure of the C-NPG, we shift our focus to its electronic structure. Since the C-NPG is laterally fused through an extended acene, the electronic coupling between neighboring nanoribbons can be expected to be large. In addition, rubicene is known to be an electron acceptor and so it is reasonable to expect C-NPG to exhibit accessible frontier states.[134] We perform DFT calculation to analyze the electronic structure and compare with the STM measurement.

Fig. 7.3(A) shows the energy-dependent local density of states (LDOS) recorded by measuring the differential conductance (dI/dV) of the STM tunnel junction while holding

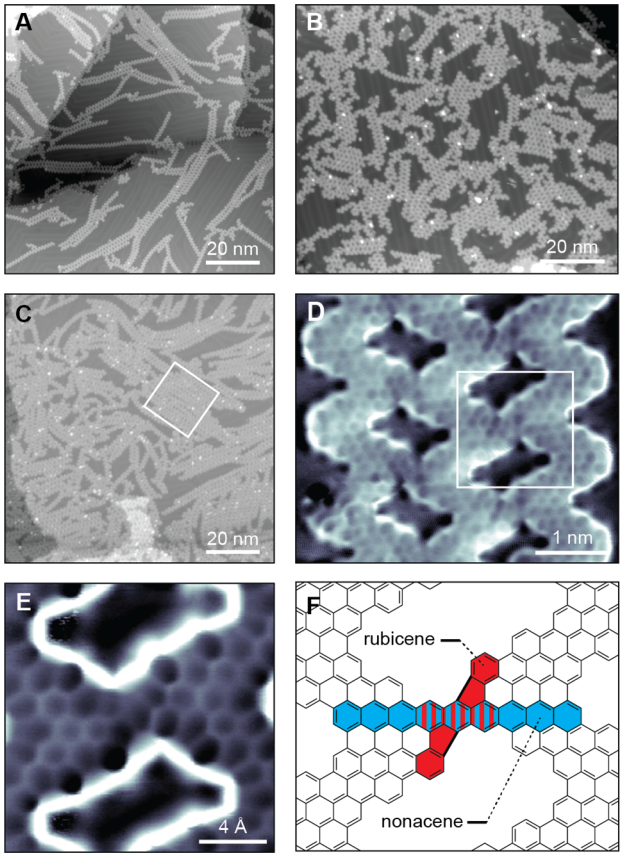

Figure 7.2: Synthesis of C-NPG. (A) STM topographic image of 0.25 monolayer coverage of C-NPG on Au(111) after deposition of 2 onto Au(111) held at $T_1 = 180°C$ and subsequent annealing to $T_2 = 400°C$ (V = 1.2 V, I = 50 pA). (B) STM topographic image of 0.75 monolayer coverage of C-NPG on Au(111) after deposition of 1 onto Au(111) held at $24°C$ and subsequent annealing to $T_2 = 400°C$ (V = –1.2 V, I = 50 pA). (C) STM topographic image of 0.75 monolayer coverage of C-NPG on Au(111) after deposition of 2 onto Au(111) held at $T_1 = 180°C$ and subsequent annealing to $T_2 = 400°C$ (V = 1.2 V, I = 50 pA). (D) Bond-resolved STM image of a region containing three fused ribbons (V = –50 mV, I = 200 pA, V_{osc} = 15 mV, f = 620 Hz). (E) High-resolution bond-resolved STM image of the region indicated in (D) (V = 20 mV, I = 250 pA, V_{osc} = 10 mV, f = 620 Hz). (F) Schematic representation of the rubicene-type interface imaged in (D,E).

the tip above the interface region of the C-NPG shown in the inset (position indicated by the red cross). Valence band (VB) and conduction band (CB) onsets are observed at –0.9 V and 1.6 V, respectively, reflecting a bulk GNR band gap of 2.7 eV (similar to previously measured values for chevron GNRs on Au(111)).[79][83][135][80] A pronounced resonance, however, is observed at 0.72 V that has a distinct shoulder at a higher bias. Because this resonance lies inside the bulk chevron GNR energy gap, we herein refer to this new feature as the in-gap band (IGB). Fig. 7.3(B) shows energy-resolved dI/dV maps corresponding to the LDOS of the CB onset, the 0.72 V resonance feature, and the VB onset (top to bottom). We observe that the electronic wavefunctions corresponding to the band onsets are delocalized over the entire structure (i.e., all interfaces and edges light up) whereas the 0.72 V feature is localized exclusively at the pore interfaces. The resonances observed in the dI/dV point spectra and the patterns observed in dI/dV mapping can be reasonably reproduced by ab initio electronic structure calculations. Fig. 7.3(D) shows the C-NPG density of states (DOS) calculated using DFT while Fig. 7.3(C) shows the calculated LDOS maps corresponding to the CB onset, the IGB, and the VB onset for three fused ribbons having the same geometry as seen experimentally. The theoretical bulk CB and VB band edge states extend throughout the C-NPG structure whereas the calculated IGB localizes at the pore interface with small wavefunction overlap with neighboring pores, in good agreement with the STM measurement. The peak shape of the IGB, including the distinct high-energy shoulder, is also accurately reproduced by the calculation. These results demonstrate that C-NPG is a new 2D electronic material with low-energy electronic states deep within the bulk band gap of the constituent GNRs that are primarily localized on the rubicene interfaces adjacent to pores. Furthermore, even though a defect is clearly present in the bottom-left corner, the electronic structure remains unaffected, with the IGB uniformly distributed over the interfaces, and in good accordance with theory.

Since the interfaces define a superlattice, it is expected that the electronic states localized on them should give rise to 2D dispersing features in the C-NPG band structure.[136]-[137][1][37][38][39] It is useful to analyze this interface behavior in more depth in order to gain insight into how to tune the electronic structure of NPG. This is not only relevant to the specific C-NPG synthesized here, but in general to other possible C-NPG varieties that may be designed through functional analogs of monomers 1 and 2. We start by considering a hypothetical isolated fluorenyl-chevron GNR exhibiting evenly spaced sp2-hybridized π-radicals at the apices of fluorenyl groups lining both edges of the ribbon (Fig. 7.4(A)). This structure was chosen as a C-NPG building block because the fluorenyl groups along the edges (highlighted in red) constitute one-half of the rubicene interface structure found in C-NPG. Furthermore, this structure represents the GNR expected to arise from precursors 1 and 2. Fig. 7.4(B) shows the DFT calculated band structure of this GNR while Fig. 7.4(C) shows the local (red) and total (black) DOS (the LDOS here is obtained by projecting band states onto the fluorenyl groups highlighted in red in Fig. 7.4(A)). The 1D GNR band structure shows bulk VB and CB band edges as well as an IGB. The projected LDOS (Fig. 7.4(C)) indicates that the IGB arises from atoms lining the convex edge of fluorenyl-chevron GNRs. A significant difference between this isolated GNR and C-NPG is that the isolated GNR is metallic due to the in-gap band straddling the Fermi level.[2]

The semiconducting band structure of 2D C-NPG (shown in Fig. 7.4(E)), by contrast, shows a higher energy IGB that lies $\sim$0.5 eV above the Fermi level. Close inspection shows

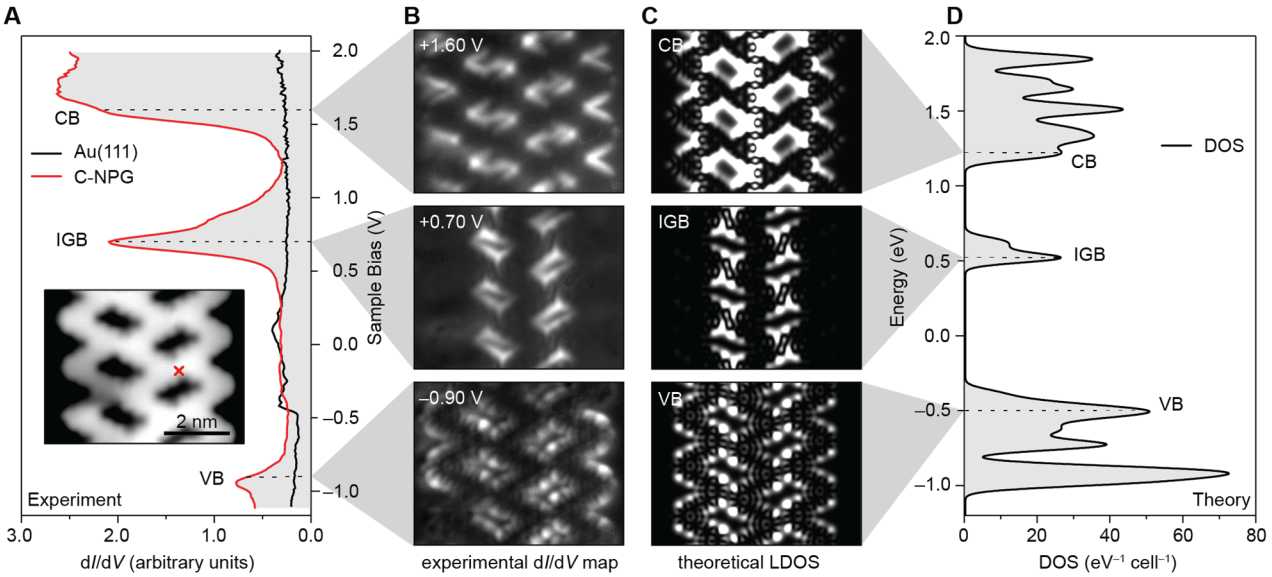

Figure 7.3: Electronic structure of the C-NPG. (A) STS dI/dV spectrum recorded on the rubicene interface of C-NPG. The inset shows a constant current STM topograph (V = 0.7 V, I = 50 pA) with the point spectroscopy location marked by a red cross (same region of C-NPG as shown in Fig. 7.2(D)). (B) Differential conductance maps of the valence band (VB) (–0.90 V), in-gap band (IGB) (0.72 V), and conduction band (CB) (1.60 V). (C) DFT simulated LDOS maps of the structure shown in the inset of (A). The maps are calculated by integration over an energy window of 10 meV from the band edge. (D) DFT simulated density of states.

another difference between the 2D C-NPG DOS (Fig. 7.4(F)) and the isolated 1D GNR DOS (Fig. 7.4(C)): the localized interface states for C-NPG appear at two energies, not just one. One band of states is the familiar in-gap band (IGB) above the Fermi energy, but the other occurs much lower in energy and appears below the VB edge. Formation of C-NPG is thus seen to cause the edge states of isolated GNRs (Fig. 7.4(B, C)) to split in order to yield two sets of C-NPG interface bands. Here, fusion of each fluorenyl pair shared between adjacent GNRs into a single rubicene moiety causes the fluorenyl orbitals to hybridize and split energetically into bonding/anti-bonding pairs. The anti-bonding states combine to form the C-NPG IGB at higher energy while the bonding states form the lower energy C-NPG band. This picture is supported by analysis of the wave functions, where the bonding (antibonding) 2D interface states can be recognized as an antisymmetric (symmetric) combination of 1D edge states (see Fig. 7.5). Edge hybridization thus causes what would otherwise be isolated 1D metallic GNRs to evolve (at least conceptually) into a semiconducting 2D nanopore mesh.

These ab initio DFT electronic structure results can be more intuitively understood using an effective tight-binding model. Here we consider the edge orbitals localized on the fluorenyl groups as effective basis states that link up to form a 1D electronic network for the isolated GNR (Fig. 7.4(A)) and a 2D electronic network for the C-NPG (as shown by the red circles in Fig. 7.4(G)). In the 1D case, the electronic dispersion can be found by assuming that

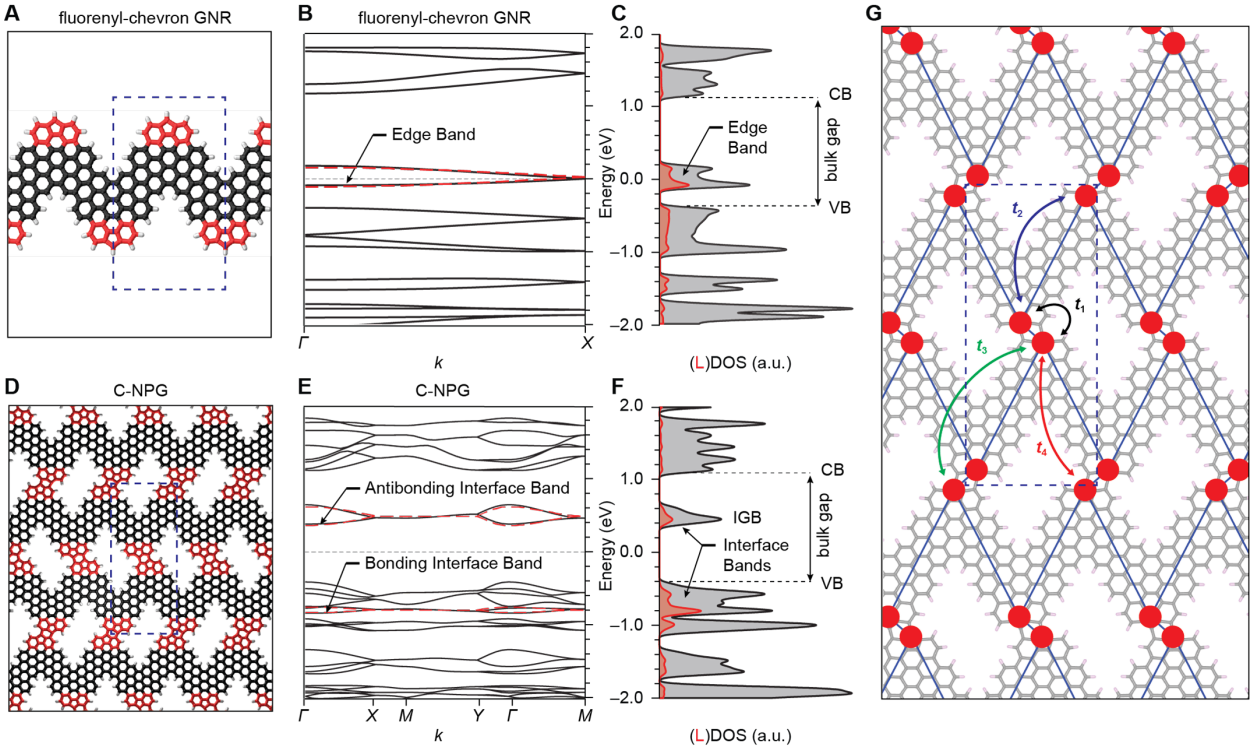

Figure 7.4: Electronic structure of the 1D chevron GNR and 2D C-NPG. (A) Structure of an isolated fluorenyl-chevron GNR with the edge fluorenyl groups highlighted in red and the quasi 1D unit cell indicated by a rectangle. (B) Electronic dispersion of fluorenyl-chevron GNR. The black bands are predicted by DFT calculations while the red, dashed bands are those of an effective tight-binding model (with parameters fit to DFT results) described in the text. (C) Local (red) and total (black) density of states of fluorenyl-chevron GNR. (The LDOS is obtained by projecting states onto the π-orbitals of the fluorenyl groups.) (D) Structure of the C-NPG anti configuration with the interface (rubicene) groups highlighted in red and the 2D unit cell indicated by a rectangle. (E) Electronic dispersion of C-NPG. The black bands are the DFT result while the red, dashed bands are those of an effective tight-binding model (with parameter fit to DFT results) described in the text. (F) Local (red) and total (black) density of states of C-NPG. (The LDOS is obtained by projection onto the π-orbitals in the pentagon region.) (G) Effective tight-binding model using basis states that represent the fluorenyl groups (red circles) coupled via nearest neighbor electronic hopping parameters t_1 (black) and t_2 (blue), and next-nearest-neighbor hopping parameters t_3 and t_4 (green and red, respectively).

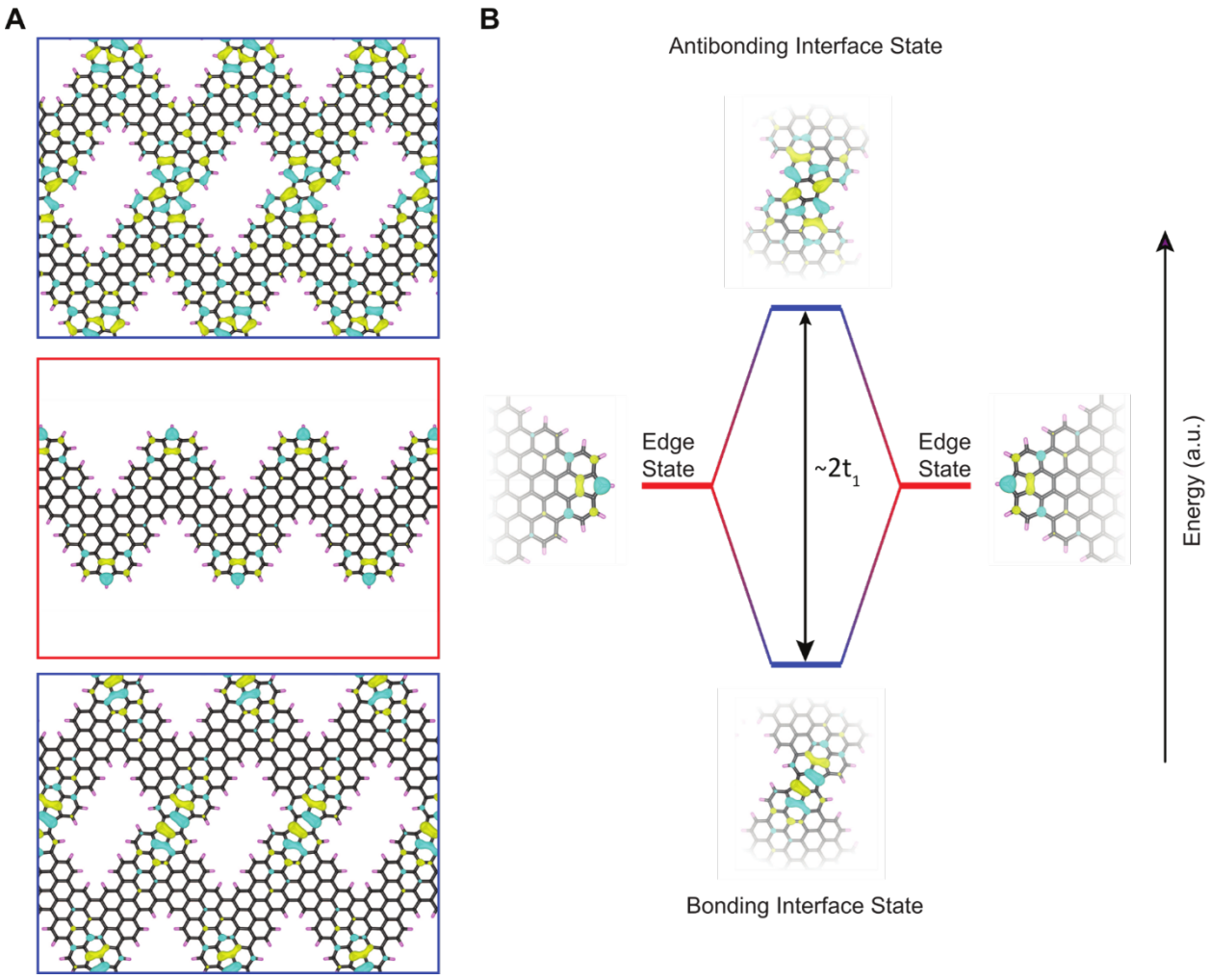

Figure 7.5: Hybridization of 1D GNR edge-states into 2D C-NPG interface states. (A) Crystal orbitals corresponding to bonding (bottom panel) and antibonding (top panel) interface states, as well as the edge state for a 1D fluorenyl-chevron GNR (middle panel). All crystal orbitals are calculated using DFT and drawn at the Γ-point. (B) Schematic process of hybridization of 1D edge band states from an initial energy (red horizontal lines) into energy-split 2D bonding and anti-bonding interface bands (blue horizontal lines). The hybridization/splitting is characterized by an effective tight-binding hopping parameter t_1.

an electron placed on one edge orbital has an amplitude t_2 to hop along the ribbon to an adjacent orbital. In the 2D case, the edge orbital network has an even stronger coupling t_1 between edge orbitals within a single rubicene moiety that is responsible for splitting them into bonding and anti-bonding interface states (weaker next-nearest-neighbor coupling is described by hopping amplitudes t_3 and t_4). The 1D GNR thus has two basis states per unit cell with one hopping parameter t_2, and so results in two bands that fit well to the GNR DFT band structure for $t_2 = –65meV$, as shown by the two dashed lines in Fig. 7.4(B). The 2D C-NPG, on the other hand, has four basis states per unit cell which result in four bands as shown by the dashed lines in Fig. 7.4(E). These bands fit well to the interface bands of the 2D C-NPG DFT band structure after optimization of the hopping amplitudes ($t_1 = 645meV$, $t_2 = –23meV$, $t_3 = –22meV$, $t_4 = –20meV$). These interface states form a distorted honeycomb lattice with distinct hopping parameters compared to a normal graphene lattice. The C-NPG bands are split into an upper pair that lies in the bulk gap and a lower pair that are resonant with the valence band complex. These are precisely the bands that arise from hybridization-induced splitting of orbitals or modes localized in the fluorenyl edge groups of the isolated GNR in Fig. 7.4(A–C). The electronic behavior of the 2D C-NPG pore states is thus encoded in the edge-states engineered for the constituent 1D building block GNRs through the rational design of the molecular precursor.

A remaining question is whether the C-NPG GNR building block, the fluorenyl-chevron GNR shown in Fig. 7.4(A), can actually exist in a laboratory rather than simply being a useful construct for understanding C-NPG electronic structure. The answer here is mixed. We do observe isolated, unlinked GNRs in lower-coverage samples, but their structure is not identical to Fig. 7.4(A). A typical example is shown in Fig. 7.6(A) which shows a BRSTM image of an isolated GNR derived from precursor 1. Close-up images of the edges of this GNR in Fig. 7.6(B) and Fig. 7.6(C) show two different edge-structures. The edge-structure shown in Fig. 7.6(B) features a hydrogen-saturated five-membered ring within a fluorene group and is by far the dominant edge structure (80% of edge segments). The edge-structure in Fig. 7.6(C) is seen much less frequently (5% percent of edge segments) but is highly reproducible. The apex of the edge-structure in Fig. 7.6(C) extends further than the edge-structure in Fig. 7.6(B) and also appears to be pulled closer to the surface (i.e., it has darker contrast in the BRSTM image).

STM spectroscopy helps us to better understand the nature of these different GNR edge-structures. 7.6(D) shows a dI/dV spectrum (blue curve) obtained with the STM tip held over the dominant edge-structure shown in 7.6(B). Valence and conduction band peaks are clearly visible and result in a bandgap of 2.4 eV, consistent with previous spectroscopy of conventional chevron GNRs lacking the five membered ring of the fluorenyl group.[79][83][135] No signs of in-gap states are seen for this edge-structure.

7.4 Conclusion

We found a novel nanoporous 2D graphene that could be synthesized with atomic precision. Bond-resolved scanning tunneling microscopy reveals that internal interfaces within this 2D pore network exhibit rubicene-type linkers that arise from the lateral fusion of partially dehydrogenated fluorene-chevron GNRs. The resulting C-NPG exhibits a novel in-gap

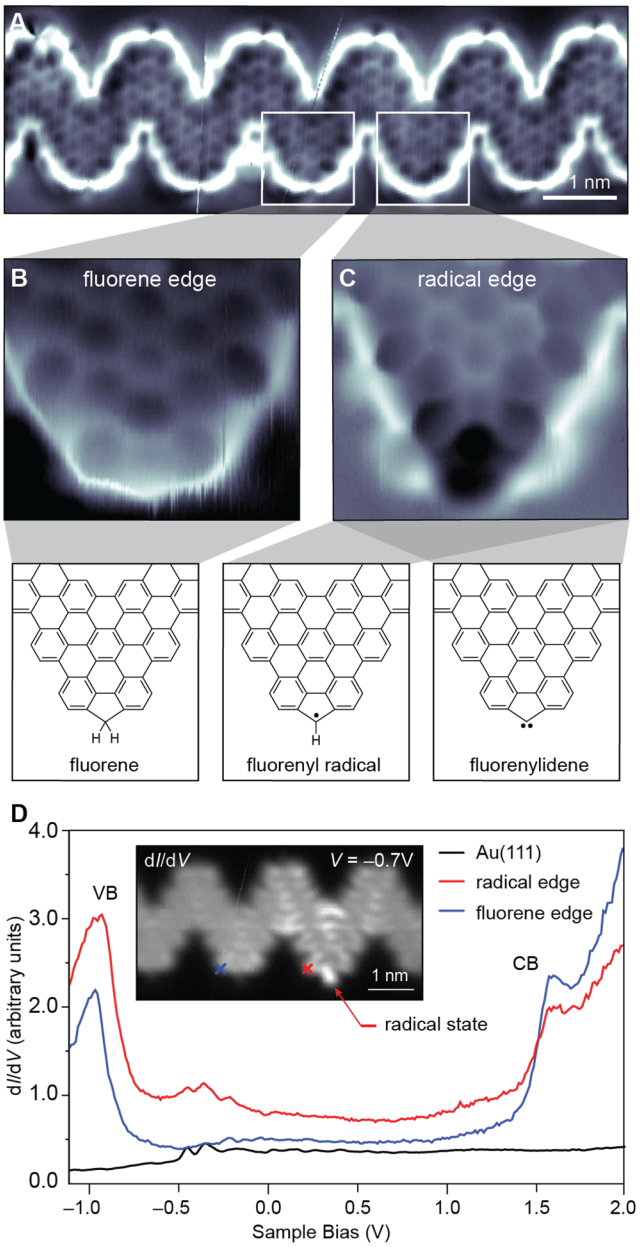

Figure 7.6: Edge electronic structure of isolated fluorene-chevron GNR. (A) Bond-resolved STM image of an isolated fluorene-chevron GNR using CO-tip (V = –50 mV, I = 180 pA, V_{osc} = 20 mV). (B) Bond-resolved STM image of the segment indicated in (A) containing a methylene edge group (V = 15 mV, I = 200 pA, V_{osc} = 10 mV). (C) Bond-resolved STM image of the neighboring segment indicated in (A) (V = 20 mV, I = 250 pA, V_{osc} = 10 mV). Possible chemical structures are depicted below. (D) Scanning tunneling spectroscopy of an isolated fluorene-chevron GNR (V_{osc} = 4 mV, f = 620 Hz). The red and blue spectra are recorded at the positions indicated in the inset (V_{osc} = 20 mV, f = 620 Hz). The inset shows a constant height dI/dV scan of the GNR obtained at V = –0.7 V for the same nanoribbon shown in panel (A). Location of the radical state is marked by an arrow (same edge element as shown in (C)).

band localized on the rubicene interfaces around the pores. These features are reproduced by both DFT and coarse-grained tight-binding calculations which show that the electronic structure of this new 2D material may be understood in terms of the edge modes of 1D GNR building blocks. The fully-linked 2D behavior is also consistent with the experimental properties of isolated GNRs where sp2-hybridized π-radicals exist due to spurious dehydrogenation of the fluorenyl groups lining the edge. This novel materials pave the way to study distorted super-graphene and electronic engineering of low-dimensional structures.

Chapter 8

Evidence for flat band induced excitonic insulator ground state in [4]triangulene Kagome lattice

Electron-hole pair excitations in semiconductors have been predicted to be able to give rise to a highly correlated many-body ground state, the excitonic insulator (EI)[138][139]. Under appropriate conditions below a critical temperature (T_c), strongly bound electron-hole pairs spontaneously form and undergo a phase transition from a normal band insulator into an exciton condensate, transforming the parent material into a novel correlated insulator. Despite recent advances in spectroscopic tools, clear direct experimental evidence for the EI state has been elusive and is often obfuscated by accompanying electronic effects[140]-[141]. Here we present the reticular bottom-up synthesis of a Kagome lattice of [4]triangulene[142], a two-dimensional (2D) covalent organic framework (COF) imbued with a deliberate excitonic instability[143] — excitons with binding energies larger than the bandgap — arising from a pair of flat bands (FBs). Theoretical analyses based on first-principles calculations and scanning tunnelling spectroscopy (STS) reveal quasiparticle spectral signatures mixing valence (VB) and conduction (CB) characteristics of the FBs along with a non-trivial semiconducting gap that can only be explained by invoking many-body theory.[144][145] Our findings spectroscopically corroborate the nature of a FB induced exciton insulator ground state and provide a robust yet highly tuneable platform for the exploration of correlated quasi-boson physics in quantum materials.

8.1 Introduction

A distinguishing characteristic of strongly correlated phases of matter is that the behavior of their constituent electronic excitations can no longer be described as a non-interacting renormalized Fermi gas. It is these correlated phases that have given rise to some of the most exciting quantum phenomena in materials. Excitonic insulators (a condensed phase of electron-hole pairs) is a correlated many-body ground state predicted in the 1960's that can arise in appropriate semimetals or narrow gap-semiconductors below a critical temperature (T_c)[138][139][143][146]. Whereas the high charge carrier density associated with the

overlapping conduction and valence band (i.e., a negative band gap (E_g)) in semimetals effectively screens the electron-hole ($e^- - h^+$) interaction depressing T_c, an intrinsic instability in the single-particle (quasiparticle) band structure of a semiconductor can induce the spontaneous condensation of excitons – the electron-hole pairs – provided the exciton binding energy (E_b) exceeds the magnitude of the gap in the conventional band insulator phase[144][146]-[147]. While the underlying principle has been understood for more than 50 years[138][139], exercising a deterministic control over subtle many-body interactions represents a veritable challenge and could imbue otherwise ordinary materials with truly exotic electronic phases[140]-[148][144][145][149]-[150]. The realization of an EI could expand the boundaries of tailor-made quantum materials, providing deeper insight into strongly correlated phenomena, e.g. the crossover between Bardeen Cooper-Schrieffer (BCS) and BEC theory[151][152][153].

8.2 Flat Bands and Excitonic Effect

Favourable conditions for the realization of an EI ground state ($E_b > E_g$) not only call for small gap semiconductors, but for an increase in the quasiparticle masses and a reduction in the screening of the Coulomb potential binding the $e^- - h^+$ pairs — thus maximizing E_b. Layer materials herein represent privileged scaffolds as the 2D confinement intrinsically lowers the screening of charge carriers when compared to a 3D crystal lattice. The correlation between e^- and h^+ can further be augmented by applying the tools of zero-mode engineering[2] to give rise to topological flat bands featuring charge carriers with huge effective masses and a greatly enhanced localization of the exciton wavefunction[154]-[155]. Our strategy for engineering a robust EI ground state follows the design of a diatomic Kagome lattice of triangulenes – nanoscale equilateral triangles of graphene cut along the a_1 and a_2 lattice vectors – proposed by Sethi et al.[143][146]. Fig. 8.1a shows a valence bond model for the open-shell S = 3/2 ground state of an isolated [4]triangulene arising from a sublattice imbalance $\Delta N = N_A - N_B = 3$, where N_A and N_B are the number of A and B sublattice sites of graphene, respectively. Nearest-neighbour analyses reveal three states (zero-modes) at the Fermi level. These three zero-modes unique to [4]triangulene are reminiscent of the orbital coordination number of a site in a diatomic Kagome lattice and when fused along the three vertices give rise to an orbital valence bond solid depicted in Fig. 8.1b (b_1 and b_2 are the lattice vectors of the diatomic Kagome lattice unit cell containing a pair of [4]triangulene superatoms). The corresponding tight-binding (TB) Hamiltonian can be expressed as

$$\hat{H} = t_1 \sum_{\langle ij\rangle,\alpha} c^\dagger_{i\alpha} c_{j\alpha} + t_2 \sum_{\langle\langle ij\rangle\rangle,\alpha} c^\dagger_{i\alpha} c_{j\alpha} + t_3 \sum_{\langle\langle\langle ij\rangle\rangle\rangle,\alpha} c^\dagger_{i\alpha} c_{j\alpha} \tag{8.1}$$

where t_1, t_2, and t_3 are the hopping amplitudes defined in Fig. 8.1b (t_2 is expected to be small due to sublattice polarization of the zero-modes). $c^\dagger_{i\alpha}$ and $c_{j\alpha}$ are the creation and annihilation operators of the zero-mode at site i and j with spin . The TB Hamiltonian gives rise to six bands, with a pair of valence (VB) and conduction (CB) FBs (blue and red bands in Fig. 8.1c, respectively) flanked on either side by pairs of comparatively dispersive bands. The large effective masses of and the overlap between e^- and h^+ wavefunctions associated with the FBs in 2D increases the E_b while a large exchange interaction raises the

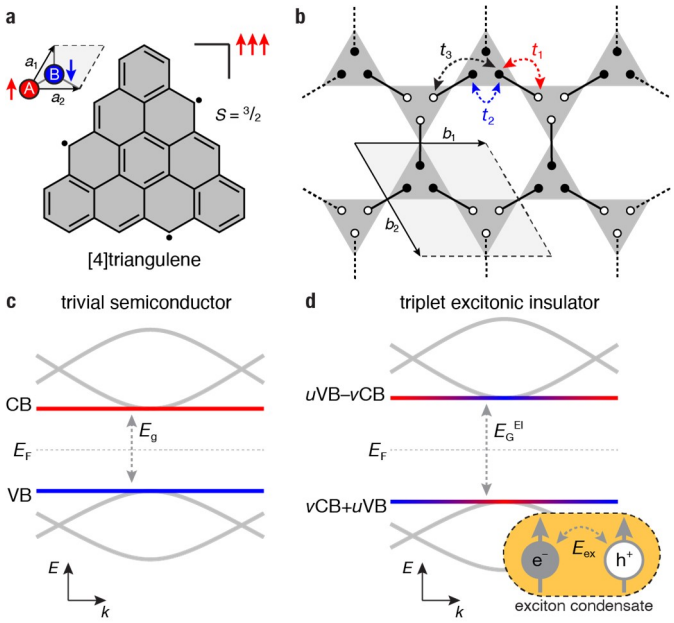

Figure 8.1: Flat-band induced triplet excitonic insulator ground state in a [4]triangulene Kagome lattice. a, Valence bond model representation of the quartet (S = 3/2) ground-state of [4]triangulene. Unit-cell and lattice vectors (a_1, a_2) of spin-polarized bipartite lattice of graphene is provided for reference. b, Diatomic Kagome lattice spanned by [4]triangulene dimers (unit-cell shaded in grey, lattice vectors b_1, b_2). Filled and open circles represent excess up or down electron spins arising from the lattice imbalance at each [4]triangulene superatom site $\Delta N = N_A - N_B$. t_1, t_2, and t_3 are tight-binding hopping amplitudes. c, Schematic representation of the band structure of a flat-band conventional semiconductor ground-state. d, Schematic representation of the band structure of a triplet excitonic insulator ground-state. E_g, E_G^{EI}, and E_{ex} are the semiconducting band gap, the new quasiparticle gap in the EI state, and the exciton energy, respectively. Colour gradient in$uVB - vCB$ and $vCB + uVB$ represents the mixing of characters of the valence (blue) and conduction (red) flat-bands (of the conventional band insulator) in the excitonic insulator quasiparticle states (u and v are the respective mixing coefficients). BEC formed by triplet excitons shaded in orange indicates the EI ground state and should not be viewed as a part of the quasiparticle band structure.

singlet-triplet splitting energy (ΔE_{ST}) favouring the formation of a robust triplet EI ground state[24][154]-[156], which are confirmed by our ab initio GW-BSE calculations[157] and in agreement with Ref. [143].

8.3 Experimental Result Summary

Guided by this idea we designed two competent molecular precursors for the reticular growth of a [4]triangulene COF ([4]TCOF), the benzo[c]naptho[2,1-p]chrysenes. The synthesis is depicted in Fig. 8.2a. The local electronic structure of isolated crystalline domains of

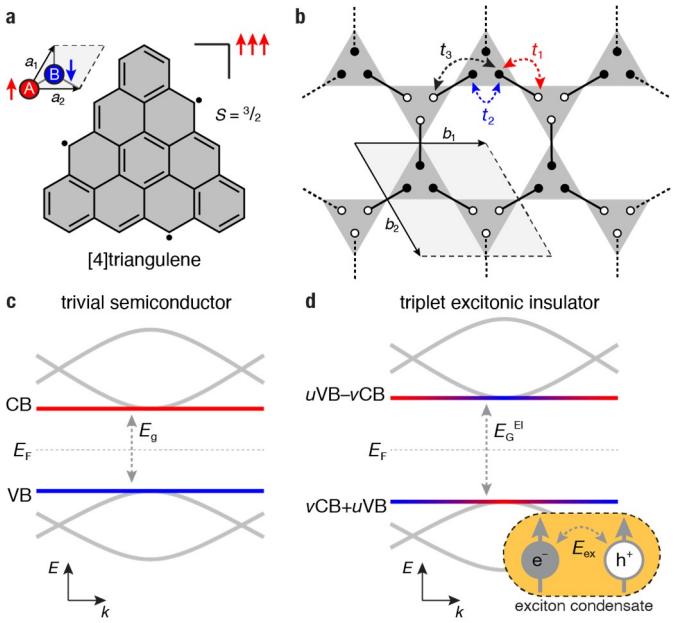

Figure 8.2: Bottom-up synthesis of [4]TCOF Kagome lattice. a, Schematic representation of the bottom-up synthesis and on-surface growth of [4]TCOFs from molecular precursors. b, STM topographic image of 2D covalent network of [4]triangulenes on Au(111) ($V_s = 200$ mV, $I_t = 20$ pA). c, STM topographic image of a segment of the Kagome lattice of [4]TCOF ($V_s = 50$ mV, $I_t = 20$ pA). d, BRSTM topographic image of fully cyclodehydrogenated [4]TCOF segment showing the C-C bonding between vertices of triangulenes along with the characteristic zigzag edges of [4]triangulene building blocks ($V_s = 10$ mV, $I_t = 400$ pA). All STM experiments performed at T = 4 K.

[4]TCOF was characterized by differential tunnelling (dI/dV) spectroscopy. A typical dI/dV point spectrum recorded at a position corresponding to the center and the zigzag edge (see BRSTM image in Fig. 8.3c) of a [4]triangulene subunit are depicted in Fig. 8.3a,b. While dI/dV point spectra recorded near the center of a triangulene are featureless, besides a characteristic signature assigned to the Au(111) surface state, dI/dV spectra recorded along the zigzag edges show eight prominent features in the range between $-2.0V < V_s < +2.0V$. Two broad peaks centered at $V_s = -1.55 \pm 0.02V$ (Peak 1) and $V_s = +1.05 \pm 0.02V$ (Peak 8) bracket E_F and can be assigned to deep-lying (i.e. energetically remote from E_F) states in the bulk VB and CB, respectively (Fig. 8.3d). Fig. 8.3b shows a magnification of the dI/dV point spectra taken over a narrower bias range of $-0.6V < V_s < +0.6V$. Spectra recorded along the zigzag edge show a distinctive pattern of five peaks (Peaks 2, 3, 4, 6, and 7) flanking a sharp dip in the differential tunnelling current centred at $V_s = 0.00 \pm 0.05V$(Feature 5). dI/dV maps collected at an imaging bias close to $V_s = 0.00V$ (Fig. 8.3g) reveal the structure of a featureless network with contrasts rising barely above the Au(111) background, punctuated only by a bright zero-mode state emanating from a local defect in the [4]TCOF lattice. Above and below the semiconducting gap ($E_{exp} \sim 0.20eV$) the dI/dV signal rises sharply towards two steps centered at $V_s = +0.10 \pm 0.05V$ (Peak 6) and $V_s = -0.10 \pm 0.05V$

(Peak 4). dI/dV imaging of the spatial distribution of the LDOS at energies close to Peak 6 ($V_s = +0.15V$ in Fig. 8.3f) reveals a highly diffuse state at the center of the [4]triangulene superimposed by dark shaded lobes along the zigzag edges. The unusually diffuse nature of the state around $V_s = +0.15V$ coincides with a characteristic peak in the Au(111) spectrum suggesting the observed LDOS is a superposition of [4]TCOF and Au states dominated by the background. dI/dV imaging at the corresponding negative bias $V_s = -0.15V$ (Peak 4, Fig. 8.3h) instead reveals a pattern of four bright lobes lining the zigzag edges of each [4]triangulene subunit. The last lobe on either side is shared between zigzag edges and, together with the last lobe of its neighbor [4]triangulene forms the junction between adjacent building blocks. Beyond these two steps the dI/dV signal continues to rise steeply and peaks at $V_s = +0.30 \pm 0.02V$ (Peak 7), and $V_s = -0.30 \pm 0.02V$(Peak 3) respectively. The unusually narrow peak shape and the large signal intensity at $V_s = \pm 0.30V$ suggest the features represent the signature of van Hove singularities in the quasiparticle density of states. Differential conductance maps recorded at the corresponding biases show clearly distinctive patterns. At $V_s = +0.30V$ (Peak 7) the LDOS is most intense at the lobes coinciding with the junction between covalently linked [4]triangulenes while the signal along the zigzag edges is only slightly weaker. At $V_s = -0.30V$ (Peak 3) the signal intensity almost uniformly distributed along the four lobes lining the zigzag edge. The last notable feature is a peak at $V_s = -0.52V$ (Peak 2). The corresponding differential conductance maps are reminiscent of the spatial LDOS distribution associated with Peak 3 and are likely associated with the same band. dI/dV point spectra recorded directly above the C-C bond linking two adjacent [4]triangulene subunits qualitatively mirror the number and position of peaks recorded along the zigzag edges.

8.4 Theoretical Analysis

To explore theoretically the electronic ground state of [4]TCOFs we evaluated two distinct models. First, we attempt to describe the electronic structure of a [4]TCOF using conventional ab initio density functional theory (DFT) in the local density approximation (LDA). In a second approach, we consider a correlated ground state of $e^- - h^+$ pairs within a BCS-like framework, thus allowing for a mixing of VB and CB wavefunction characters in the quasiparticle states of an EI. The DFT-LDA quasiparticle band structure for the six bands closest to the band gap along with the calculated density of states (DOS) of the [4]TCOF are depicted in Fig. 8.4a and 8.4b, respectively. Two narrow bands (denoted CFB and VFB) bracket E_F, enclosing a conventional semiconducting gap of $E_g \sim 200mV$. Both bands are virtually dispersionless. The two FBs and the other two dispersive band complexes can be fit by a TB model (Eq. 1) with t_1 = -0.132 eV, t_2 = -0.013 eV t_3= -0.016 eV (Fig. 8.4a, dashed lines). Above and below the conduction and valence FBs, the two pairs of dispersive bands complete the TB picture of a ying-yang Kagome superlattice. On either side of E_F, the DFT-LDA DOS shows the onset of two sharp features centred at $E - E_F = \pm 0.10eV$ that extend into a series of smaller peaks at higher and lower energy for the CB and VB complex, respectively. Fig. 8.4c,d show the square of the theoretical wavefunction amplitude maps at a distance of 4 $\AA$ above the plane of a freestanding [4]TCOF at energies corresponding to the valence and the conduction FB edges. Both LDOS maps show distinctive nodal patterns,

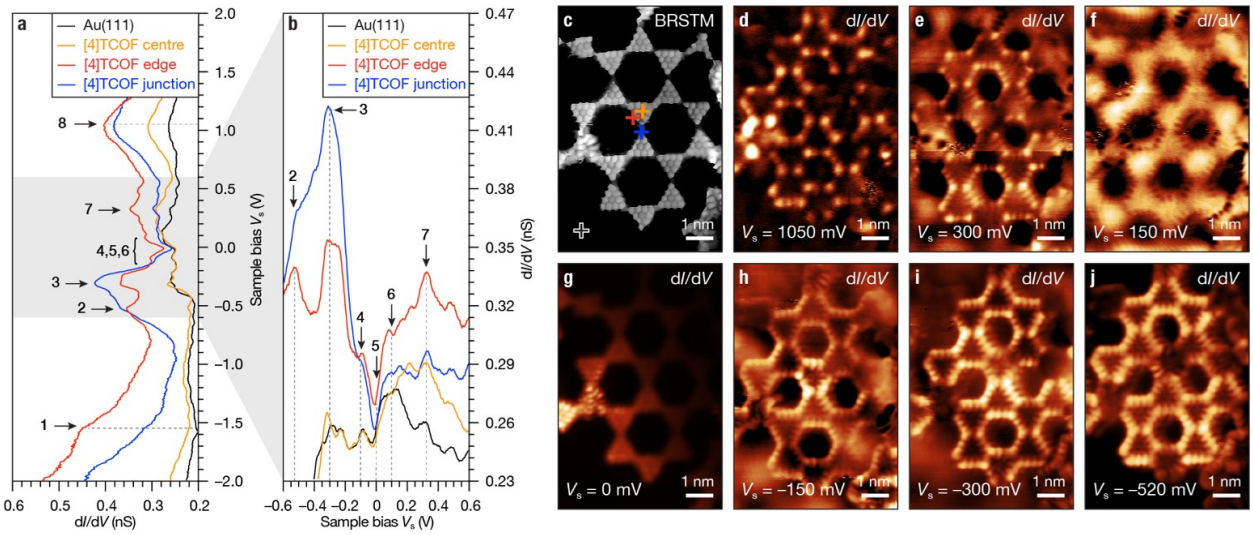

Figure 8.3: Electronic structure of [4]TCOF. a-b, dI/dV point spectra of [4]TCOF/Au(111) recorded at the position marked in (c) (Au(111) surface state, black; centre of [4]triangulene, orange; zigzag edge of [4]triangulene, red; junction between two [4]triangulene units, blue; V_{ac} = 10 mV, f = 455 Hz, CO-functionalized tip). c, Constant-height BRSTM image of [4]TCOF/Au(111) segment (V_s = 0 mV, V_{ac} = 10 mV, f = 455 Hz, CO-functionalized tip). Crosses mark the position of where dI/dV point spectra were recorded. d-j, Constant-current dI/dV maps recorded at a voltage bias of V_s = +1050 mV, V_s = +300 mV, V_s = +150 mV, V_s = +0 mV, V_s = -150 mV, V_s = -300 mV, and V_s = -520 mV (V_{ac} = 10 mV, I_t = 400 pA, f = 455 Hz, CO-functionalized tip). All STM experiments performed at T = 4 K.

two bright spots lining the zigzag edges for the CB (Fig. 8.4c) and two bright spots at the position of the junction between two [4]triangulenes for the VB (Fig. 8.4d). The corresponding experimental dI/dV maps (Fig. 8.4e,f) recorded on pristine [4]TCOF domains at $V_s = \pm 0.10V$ instead both show a uniform distribution of the wavefunction amplitude shared along the zigzag edges and the junction interface. The obvious mismatch between DFT-LDA LDOS predictions for CB and VB edge states (Fig. 8.4c,d) and the experimental STS mapping (Fig. 8.4e,f) suggests that a conventional band insulating ground state given by DFT-LDA is insufficient to describe the electronic structure of [4]TCOF.

In formal analogy to the BCS theory of superconductivity, following Kohn1, we derive a second model that describes the transition from a band insulator to an EI for the [4]TCOF ground state and arrive at a theory for the quasiparticle spectrum that is measured in STS.

Starting from the gap equation of an EI[138]

$$\Delta_{cvk} = -\sum_{cvkv'c'k'} V_{cvk,c'v'k'} \frac{\Delta_{c'v'k'}}{2E_{c'v'k'}} \tag{8.2}$$

where c, v, c', v' are the CB and VB indexes, k, k' indicate the k-points, and V is the screened Coulomb attraction potential between electron and hole in a triplet exciton state. Since the CFB and VFB have little dispersion near the EF, we can drop the c, v, k dependence of the

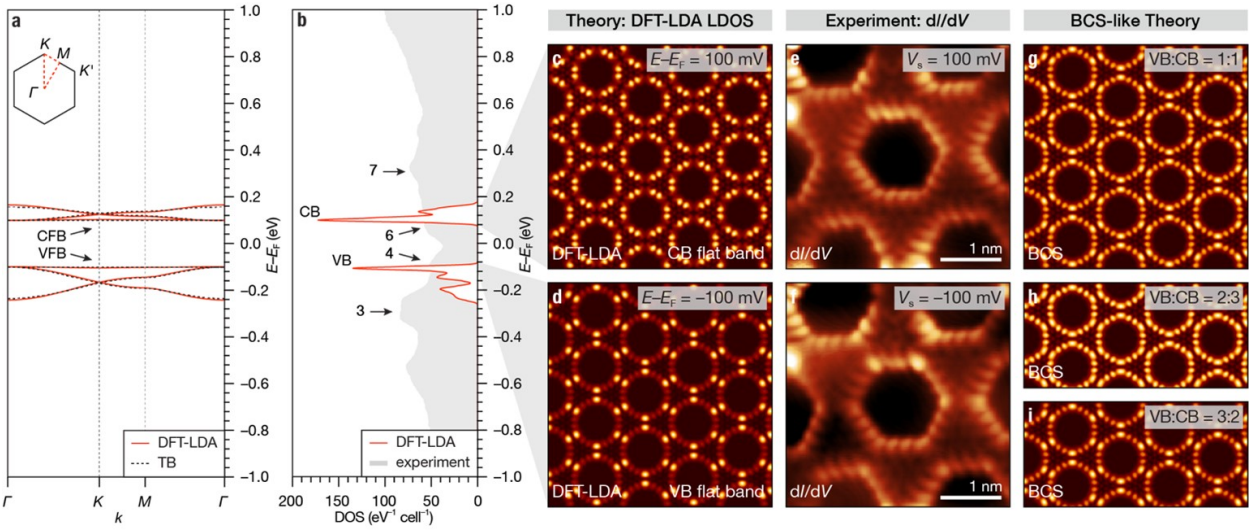

Figure 8.4: Quasiparticle states from DFT and BCS-EI calculations in [4]TCOFs. a, DFT-LDA band structure for six bands near E_F of a freestanding [4]TCOF. Valence (VB) and conduction (CB) flat-bands are indicated by arrows. b, Calculated DFT-LDA LDOS at 4 $\mathring{A}$ above a freestanding [4]TCOF (spectrum broadened by 10 meV Gaussian). The experimental dI/dV point spectrum recorded along a zigzag edge is overlaid in grey. c, Calculated DFT-LDA LDOS map evaluated at the edge of the conduction flat-band (CFB). d, Calculated DFT-LDA LDOS map evaluated at the edge of the valence flat-band (VFB). e, Experimental constant-current dI/dV maps recorded at a voltage bias of $V_s = +100mV$ ($V_{ac} = 10mV$, $I_t = 400pA$, f = 455 Hz, CO-functionalized tip). f, Experimental constant-current dI/dV maps recorded at a voltage bias of $V_s = -100mV$ ($V_{ac} = 10mV$, $I_t = 400pA$, f = 455 Hz, CO-functionalized tip). g, Calculated LDOS map resulting from a BCS-like 1:1 mixing of character of the VB and CB flat bands for quasiparticles in the EI phase. h-i, Calculated EI quasiparticle LDOS map resulting from a BCS-like 2:3 and 3:2 mixing of character of the VB and CB flat bands, respectively. All STM experiments performed at T = 4 K.

order parameter and study the averaged effect across the gap. $E_{cvk} \rightarrow E = \sqrt{\xi^2 + |\Delta^2|}$ with $\xi = 1/2(\epsilon_{CB} - \epsilon_{VB})$ where ϵ_{CB} and ϵ_{VB} are the CB and VB energies of the band insulator state, respectively. The effective quasiparticle gap E_G^{EI} in the EI state is given by $E_G^{EI} = 2E$. With $\frac{\Delta}{E_G^{EI}}$ defined as χ, we can rewrite equation 8.2 as:

$$E_G^{EI}\chi = -\sum_{cvkc'v'k'} V_{cvk,c'v'k'}\chi \tag{8.3}$$

From the Bethe-Salpeter equation (BSE)[24] for excitons from flat bands we have

$$(2\xi - E_{ex})A = -\sum_{cvkc'v'k'} V_{cvk,c'v'k'}A \tag{8.4}$$

where E_{ex} is the exciton eigenenergy. Comparing equation 8.3 and 8.4, we arrive at:

$$E_G^{EI} = (2\xi - E_{ex}) \tag{8.5}$$

This means that only if $E_{ex} < 0$, a nonzero solution for Δ is possible. During the STS experiment, the [4]TCOF Kagome lattice is adsorbed on a gold substrate. Since the exciton eigenenergy is relatively insensitive to screening by the environment, we can approximate E_{ex} from calculations on an isolated [4]TCOF Kagome lattice. GW-BSE gives an exciton eigenenergy of E_{ex} = -0.17 eV[143]. Given the experimental semiconducting gap E_{exp} determined by the peak-to-peak distance in the STS experiments, we can substitute $E_G^{EI} = E_{exp} \sim 0.20eV$. Equation 8.5 then gives an effective band gap in the band insulator phase of the [4]TCOF Kagome lattice of $2\Delta = 0.03eV$. This yields a $|\Delta| = 0.1eV$ and $|u| \sim |v|$ in the BCS ground state:

$$|G\rangle = \prod_{vck}(u + vc_{ck}^{\dagger}c_{vk})|\Phi\rangle \tag{8.6}$$

Here $|\Phi\rangle$ is the normal ground state with all VBs occupied and CBs empty, with $|u|^2 = \frac{1}{2}(1 + \frac{\xi}{E})$,$|v|^2 = \frac{1}{2}(1 - \frac{\xi}{E})$ obtained from the BCS-like theory. The quasiparticle excitation then results in an almost equal mixing of both CB and VB characters, which agrees well with our experimental findings.

Given a semiconducting gap E_{exp} 0.20 eV (derived from STS) and a triplet exciton eigenenergy $E_{ex} = -0.17eV$ (derived from GW-BSE)[143], a resulting finite order parameter $|\Delta| \sim 0.1eV$ gives rise to a EI ground state at finite temperatures $T < T_c$. The corresponding quasiparticle excitations yield in a nearly equal contribution in orbital character from both the conventional VB and CB states. Fig. 8.4g shows the calculated LDOS map arising from a 1:1 (VB:CB) mixing. The characteristic nodal pattern — four bright lobes lining the zigzag edges, the first and last lobe are shared between adjacent [4]triangulenes — is consistent with the experimental differential conductance maps recorded at $V_s = \pm 0.10V$ (Fig. 8.4e,f), corroborating the emergence of an EI ground state. Even for minor changes in the BCS order parameter $|\Delta|$, i.e. a slightly reduced contribution to the mixing of VB and CB in Fig. 8.4h (2:3) and 8.4i (3:2), the quasiparticle LDOS continue to return a better correspondence to the experimental dI/dV maps of [4]TCOF (Fig. 8.4e and 8.4f, respectively) than the band insulator results that do not account for strong $e^- - h^+$ correlations.

8.5 Conclusion

Our experimental and theoretical results thus provide strong evidence for the emergence of a flat-band induced EI ground state in a [4]TCOF Kagome lattice at T = 4 K and are based on a detailed investigation of the quasiparticle spectral features in both energy and space. Reticular bottom-up approaches not only provide a general strategy for accessing and exploring other strongly correlated phenomena, but give rise to an expanding class of engineered quantum materials that can deliver further and deeper insights into the crossover between BCS and BEC theory.

Bibliography

[1] Jingwei Jiang and Steven G Louie. "Topology classification using chiral symmetry and spin correlations in graphene nanoribbons". In: *Nano letters* 21.1 (2020), pp. 197–202.

[2] Daniel J Rizzo et al. "Inducing metallicity in graphene nanoribbons via zero-mode superlattices". In: *Science* 369.6511 (2020), pp. 1597–1603.

[3] Daniel J Rizzo et al. "Rationally designed topological quantum dots in bottom-up graphene nanoribbons". In: *ACS nano* 15.12 (2021), pp. 20633–20642.

[4] Peter H Jacobse et al. "Bottom-up assembly of nanoporous graphene with emergent electronic states". In: *Journal of the American Chemical Society* 142.31 (2020), pp. 13507–13514.

[5] Aidan Delgado et al. *Evidence for excitonic insulator ground state in triangulene Kagome lattice*. 2023. arXiv: `2301.06171 [cond-mat.str-el]`.

[6] Cong Su et al. "Tuning colour centres at a twisted hexagonal boron nitride interface". In: *Nature Materials* 21.8 (2022), pp. 896–902.

[7] Ethan Chi Ho Wen et al. "Magnetic interactions in substitutional core-doped graphene nanoribbons". In: *Journal of the American Chemical Society* 144.30 (2022), pp. 13696–13703.

[8] Peter H Jacobse et al. "Pseudo-atomic orbital behavior in graphene nanoribbons with four-membered rings". In: *Science advances* 7.52 (2021), eabl5892.

[9] W. Kohn and L. J. Sham. "Self-consistent equations including exchange and correlation effects". In: *Physical Review* 140.4A (1965), A1133–A1138.

[10] Marvin L. Cohen and Steven G. Louie. *Fundamentals of Condensed Matter Physics*. Cambridge, UK: Cambridge University Press, 2016.

[11] J. Ólyom. *Fundamentals of the Physics of Solids: Volume 1: Structure and Dynamics*. New York, NY: Springer Science & Business Media, 2007.

[12] J. C. Slater. "A simplification of the Hartree-Fock method". In: *Physical Review* 81.3 (1951), pp. 385–390.

[13] D. M. Ceperley and B. J. Alder. "Ground state of the electron gas by a stochastic method". In: *Physical Review Letters* 45.7 (1980), pp. 566–569.

[14] J. P. Perdew and A. Zunger. "Self-interaction correction to density-functional approximations for many-electron systems". In: *Physical Review B* 23.10 (1981), pp. 5048–5079.

[15] J. P. Perdew, K. Burke, and M. Ernzerhof. "Generalized gradient approximation made simple". In: *Physical Review Letters* 77.18 (1996), pp. 3865–3868.

[16] G. I. Csonka et al. "Assessing the performance of recent density functionals for bulk solids". In: *Physical Review B* 79.15 (2009), p. 155107.

[17] Paolo Giannozzi et al. "QUANTUM ESPRESSO: a modular and open-source software project for quantum simulations of materials". In: *Journal of physics: Condensed matter* 21.39 (2009), p. 395502.

[18] Paolo Giannozzi et al. "Advanced capabilities for materials modelling with Quantum ESPRESSO". In: *Journal of physics: Condensed matter* 29.46 (2017), p. 465901.

[19] Lars Hedin and Stig Lundqvist. "Effects of electron-electron and electron-phonon interactions on the one-electron states of solids". In: *Solid State Physics*. Vol. 23. Elsevier, 1970, pp. 1–181.

[20] Gerald D. Mahan. *Many-Particle Physics*. Springer Science & Business Media, 2013.

[21] Lars Hedin. "New method for calculating the one-particle Green's function with application to the electron-gas problem". In: *Physical Review* 139.3A (1965), A796–A823.

[22] Mark S. Hybertsen and Steven G. Louie. "Electron correlation in semiconductors and insulators: Band gaps and quasiparticle energies". In: *Physical Review B* 34.8 (1986), p. 5390.

[23] Jack Deslippe et al. "BerkeleyGW: A Massively Parallel Computer Package for the Calculation of the Quasiparticle and Optical Properties of Materials and Nanostructures". In: *Computer Physics Communications* 183.6 (2012), p. 1269. URL: `http://arxiv.org/abs/1111.4429`.

[24] Michael Rohlfing and Steven G. Louie. "Electron-hole excitations and optical spectra from first principles". In: *Phys. Rev. B* 62 (8 Aug. 2000), pp. 4927–4944. DOI: `10.1103/PhysRevB.62.4927`. URL: `https://link.aps.org/doi/10.1103/PhysRevB.62.4927`.

[25] Lorin X. Benedict, Eric L. Shirley, and Robert B. Bohn. "Optical Absorption of Insulators and the Electron-Hole Interaction: An Ab Initio Calculation". In: *Phys. Rev. Lett.* 80 (20 May 1998), pp. 4514–4517. DOI: `10.1103/PhysRevLett.80.4514`. URL: `https://link.aps.org/doi/10.1103/PhysRevLett.80.4514`.

[26] Lorin X. Benedict and Eric L. Shirley. "Ab initio calculation of $\epsilon_2(\omega)$ including the electron-hole interaction: Application to GaN and CaF_2". In: *Phys. Rev. B* 59 (8 Feb. 1999), pp. 5441–5451. DOI: `10.1103/PhysRevB.59.5441`. URL: `https://link.aps.org/doi/10.1103/PhysRevB.59.5441`.

[27] K. v. Klitzing, G. Dorda, and M. Pepper. "New Method for High-Accuracy Determination of the Fine-Structure Constant Based on Quantized Hall Resistance". In: *Phys. Rev. Lett.* 45 (6 Aug. 1980), pp. 494–497. DOI: `10.1103/PhysRevLett.45.494`. URL: `https://link.aps.org/doi/10.1103/PhysRevLett.45.494`.

[28] Yasuhiro Hatsugai. "Chern number and edge states in the integer quantum Hall effect". In: *Phys. Rev. Lett.* 71 (22 Nov. 1993), pp. 3697–3700. DOI: 10.1103/PhysRevLett.71.3697. URL: https://link.aps.org/doi/10.1103/PhysRevLett.71.3697.

[29] B. Andrei Bernevig, Taylor L. Hughes, and Shou-Cheng Zhang. "Quantum Spin Hall Effect and Topological Phase Transition in HgTe Quantum Wells". In: *Science* 314.5806 (2006), pp. 1757–1761. DOI: 10.1126/science.1133734. eprint: https://www.science.org/doi/pdf/10.1126/science.1133734. URL: https://www.science.org/doi/abs/10.1126/science.1133734.

[30] Markus König et al. "Quantum Spin Hall Insulator State in HgTe Quantum Wells". In: *Science* 318.5851 (2007), pp. 766–770. DOI: 10.1126/science.1148047. eprint: https://www.science.org/doi/pdf/10.1126/science.1148047. URL: https://www.science.org/doi/abs/10.1126/science.1148047.

[31] Xiao-Liang Qi and Shou-Cheng Zhang. "Topological insulators and superconductors". In: *Rev. Mod. Phys.* 83 (4 Oct. 2011), pp. 1057–1110. DOI: 10.1103/RevModPhys.83.1057. URL: https://link.aps.org/doi/10.1103/RevModPhys.83.1057.

[32] Andreas P Schnyder et al. "Classification of topological insulators and superconductors". In: *AIP Conference Proceedings*. Vol. 1134. 1. American Institute of Physics. 2009, pp. 10–21.

[33] Yen-Chia Chen et al. "Tuning the band gap of graphene nanoribbons synthesized from molecular precursors". In: *ACS nano* 7.7 (2013), pp. 6123–6128.

[34] Leopold Talirz et al. "On-surface synthesis and characterization of 9-atom wide armchair graphene nanoribbons". In: *ACS nano* 11.2 (2017), pp. 1380–1388.

[35] Young-Woo Son, Marvin L Cohen, and Steven G Louie. "Energy gaps in graphene nanoribbons". In: *Physical review letters* 97.21 (2006), p. 216803.

[36] Li Yang et al. "Quasiparticle energies and band gaps in graphene nanoribbons". In: *Physical Review Letters* 99.18 (2007), p. 186801.

[37] Ting Cao, Fangzhou Zhao, and Steven G Louie. "Topological phases in graphene nanoribbons: junction states, spin centers, and quantum spin chains". In: *Physical review letters* 119.7 (2017), p. 076401.

[38] Daniel J Rizzo et al. "Topological band engineering of graphene nanoribbons". In: *Nature* 560.7717 (2018), pp. 204–208.

[39] Oliver Gröning et al. "Engineering of robust topological quantum phases in graphene nanoribbons". In: *Nature* 560.7717 (2018), pp. 209–213.

[40] Andreas P Schnyder et al. "Classification of topological insulators and superconductors in three spatial dimensions". In: *Physical Review B* 78.19 (2008), p. 195125.

[41] Shinsei Ryu et al. "Topological insulators and superconductors: tenfold way and dimensional hierarchy". In: *New Journal of Physics* 12.6 (2010), p. 065010.

[42] Emil Prodan and Hermann Schulz-Baldes. "Bulk and boundary invariants for complex topological insulators". In: *K* (2016).

[43] Jun-Won Rhim, Jan Behrends, and Jens H Bardarson. "Bulk-boundary correspondence from the intercellular Zak phase". In: *Physical Review B* 95.3 (2017), p. 035421.

[44] Kuan-Sen Lin and Mei-Yin Chou. "Topological properties of gapped graphene nanoribbons with spatial symmetries". In: *Nano Letters* 18.11 (2018), pp. 7254–7260.

[45] Pierre Delplace, D Ullmo, and G Montambaux. "Zak phase and the existence of edge states in graphene". In: *Physical Review B* 84.19 (2011), p. 195452.

[46] Raffaele Resta. "Macroscopic polarization in crystalline dielectrics: the geometric phase approach". In: *Reviews of modern physics* 66.3 (1994), p. 899.

[47] Elliott H Lieb. "Two theorems on the Hubbard model". In: *Physical review letters* 62.10 (1989), p. 1201.

[48] Michael Slota et al. "Magnetic edge states and coherent manipulation of graphene nanoribbons". In: *Nature* 557.7707 (2018), pp. 691–695.

[49] N David Mermin and Herbert Wagner. "Absence of ferromagnetism or antiferromagnetism in one-or two-dimensional isotropic Heisenberg models". In: *Physical Review Letters* 17.22 (1966), p. 1133.

[50] Laurent-Patrick Lévy. *Magnetism and superconductivity*. Springer Science & Business Media, 2000.

[51] Björn Trauzettel et al. "Spin qubits in graphene quantum dots". In: *Nature Physics* 3.3 (2007), pp. 192–196.

[52] V Hung Nguyen et al. "Spin-dependent transport in armchair graphene nanoribbon structures with edge roughness effects". In: *Journal of Physics: Conference Series*. Vol. 193. 1. IOP Publishing. 2009, p. 012100.

[53] Dimas G de Oteyza et al. "Substrate-independent growth of atomically precise chiral graphene nanoribbons". In: *ACS nano* 10.9 (2016), pp. 9000–9008.

[54] G.E. Moore. "Cramming More Components Onto Integrated Circuits". In: *Proceedings of the IEEE* 86.1 (1998), pp. 82–85. DOI: 10.1109/JPROC.1998.658762.

[55] Marc Bockrath et al. "Luttinger-liquid behaviour in carbon nanotubes". In: *Nature* 397.6720 (1999), pp. 598–601.

[56] J. Luttinger. *The Luttinger Model: The First 50 Years and Some New Directions*. Ed. by Vieri Mastropietro. World Scientific, 2014, pp. 3–11.

[57] Johannes Voit. "One-dimensional Fermi liquids". In: *Reports on Progress in Physics* 58.9 (1995), p. 977.

[58] AR Goni et al. "One-dimensional plasmon dispersion and dispersionless intersubband excitations in GaAs quantum wires". In: *Physical review letters* 67.23 (1991), p. 3298.

[59] M. F. Lin and Kenneth W. -K. Shung. "Plasmons and optical properties of carbon nanotubes". In: *Phys. Rev. B* 50 (23 Dec. 1994), pp. 17744–17747. DOI: 10.1103/PhysRevB.50.17744. URL: https://link.aps.org/doi/10.1103/PhysRevB.50.17744.

[60] P Monceau et al. "Electric Field Breakdown of Charge-Density-Wave—Induced Anomalies in Nb Se 3". In: *Physical Review Letters* 37.10 (1976), p. 602.

[61] G Grüner, A Zawadowski, and PM Chaikin. "Nonlinear conductivity and noise due to charge-density-wave depinning in NbSe3". In: *Physical Review Letters* 46.7 (1981), p. 511.

[62] ZK Tang et al. "Superconductivity in 4 angstrom single-walled carbon nanotubes". In: *Science* 292.5526 (2001), pp. 2462–2465.

[63] I. Takesue et al. "Superconductivity in Entirely End-Bonded Multiwalled Carbon Nanotubes". In: *Phys. Rev. Lett.* 96 (5 Feb. 2006), p. 057001. DOI: 10.1103/PhysRevLett.96.057001. URL: https://link.aps.org/doi/10.1103/PhysRevLett.96.057001.

[64] Yea-Lee Lee et al. "Topological phases in cove-edged and chevron graphene nanoribbons: Geometric structures, Z 2 invariants, and junction states". In: *Nano letters* 18.11 (2018), pp. 7247–7253.

[65] W. P. Su, J. R. Schrieffer, and A. J. Heeger. "Soliton excitations in polyacetylene". In: *Phys. Rev. B* 22 (4 Aug. 1980), pp. 2099–2111. DOI: 10.1103/PhysRevB.22.2099. URL: https://link.aps.org/doi/10.1103/PhysRevB.22.2099.

[66] Pascal Ruffieux et al. "Electronic structure of atomically precise graphene nanoribbons". In: *Acs Nano* 6.8 (2012), pp. 6930–6935.

[67] Yen-Chia Chen et al. "Molecular bandgap engineering of bottom-up synthesized graphene nanoribbon heterojunctions". In: *Nature nanotechnology* 10.2 (2015), pp. 156–160.

[68] Chuong Van Nguyen et al. "Phase Transition in Armchair Graphene Nanoribbon Due to Peierls Distortion". In: *Journal of Electronic Materials* 46 (2017), pp. 3815–3819.

[69] Edmund Clifton Stoner. "Collective Electron Ferromagnetism". In: *Proceedings of The Royal Society A: Mathematical, Physical and Engineering Sciences* 165 (1938), pp. 372–414.

[70] Edmund Clifton Stoner. "Collective electron ferromagnetism II. Energy and specific heat". In: *Proceedings of the Royal Society of London. Series A. Mathematical and Physical Sciences* 169.938 (1939), pp. 339–371.

[71] Rupali Kundu. "Tight-binding parameters for graphene". In: *Modern Physics Letters B* 25.03 (2011), pp. 163–173.

[72] Jinming Cai et al. "Atomically precise bottom-up fabrication of graphene nanoribbons". In: *Nature* 466.7305 (2010), pp. 470–473.

[73] Amina Kimouche et al. "Ultra-narrow metallic armchair graphene nanoribbons". In: *Nature communications* 6.1 (2015), p. 10177.

[74] Pascal Ruffieux et al. "On-surface synthesis of graphene nanoribbons with zigzag edge topology". In: *Nature* 531.7595 (2016), pp. 489–492.

[75] Junzhi Liu et al. "Toward cove-edged low band gap graphene nanoribbons". In: *Journal of the American Chemical Society* 137.18 (2015), pp. 6097–6103.

[76] Ryan R Cloke et al. "Site-specific substitutional boron doping of semiconducting armchair graphene nanoribbons". In: *Journal of the American Chemical Society* 137.28 (2015), pp. 8872–8875.

[77] Shigeki Kawai et al. "Atomically controlled substitutional boron-doping of graphene nanoribbons". In: *Nature Communications* 6.1 (2015), p. 8098.

[78] Rebecca A Durr et al. "Orbitally matched edge-doping in graphene nanoribbons". In: *Journal of the American Chemical Society* 140.2 (2018), pp. 807–813.

[79] Giang D Nguyen et al. "Atomically precise graphene nanoribbon heterojunctions from a single molecular precursor". In: *Nature nanotechnology* 12.11 (2017), pp. 1077–1082.

[80] Daniel J Rizzo et al. "Length-dependent evolution of type II heterojunctions in bottom-up-synthesized graphene nanoribbons". In: *Nano Letters* 19.5 (2019), pp. 3221–3228.

[81] Chuanxu Ma et al. "Seamless staircase electrical contact to semiconducting graphene nanoribbons". In: *Nano letters* 17.10 (2017), pp. 6241–6247.

[82] Tomas Marangoni et al. "Heterostructures through Divergent Edge Reconstruction in Nitrogen-Doped Segmented Graphene Nanoribbons". In: *Chemistry–A European Journal* 22.37 (2016), pp. 13037–13040.

[83] Jinming Cai et al. "Graphene nanoribbon heterojunctions". In: *Nature nanotechnology* 9.11 (2014), pp. 896–900.

[84] Qiang Sun et al. "Coupled spin states in armchair graphene nanoribbons with asymmetric zigzag edge extensions". In: *Nano letters* 20.9 (2020), pp. 6429–6436.

[85] Shiyong Wang et al. "Quantum dots in graphene nanoribbons". In: *Nano letters* 17.7 (2017), pp. 4277–4283.

[86] Zahra Pedramrazi et al. "Concentration dependence of dopant electronic structure in bottom-up graphene nanoribbons". In: *Nano letters* 18.6 (2018), pp. 3550–3556.

[87] Eduard Carbonell-Sanromà et al. "Quantum dots embedded in graphene nanoribbons by chemical substitution". In: *Nano letters* 17.1 (2017), pp. 50–56.

[88] Christopher Bronner et al. "Hierarchical on-surface synthesis of graphene nanoribbon heterojunctions". In: *ACS nano* 12.3 (2018), pp. 2193–2200.

[89] Shiyong Wang et al. "Giant edge state splitting at atomically precise graphene zigzag edges". In: *Nature communications* 7.1 (2016), p. 11507.

[90] Sri Krishna Vadlamani et al. "Tunnel-FET switching is governed by non-Lorentzian spectral line shape". In: *Proceedings of the IEEE* 108.8 (2019), pp. 1235–1244.

[91] Matthias Koch et al. "Voltage-dependent conductance of a single graphene nanoribbon". In: *Nature nanotechnology* 7.11 (2012), pp. 713–717.

[92] Boris V Senkovskiy et al. "Finding the hidden valence band of N= 7 armchair graphene nanoribbons with angle-resolved photoemission spectroscopy". In: *2D Materials* 5.3 (2018), p. 035007.

[93] Shantanu Mishra et al. "Observation of fractional edge excitations in nanographene spin chains". In: *Nature* 598.7880 (2021), pp. 287–292.

[94] Raymond E Blackwell et al. "Spin splitting of dopant edge state in magnetic zigzag graphene nanoribbons". In: *Nature* 600.7890 (2021), pp. 647–652.

[95] Wei L Wang et al. "Topological frustration in graphene nanoflakes: magnetic order and spin logic devices". In: *Physical review letters* 102.15 (2009), p. 157201.

[96] Sheng Wang et al. "Nonlinear Luttinger liquid plasmons in semiconducting single-walled carbon nanotubes". In: *Nature Materials* 19.9 (2020), pp. 986–991.

[97] Hiromichi Kataura et al. "Optical properties of single-wall carbon nanotubes". In: *Synthetic metals* 103.1-3 (1999), pp. 2555–2558.

[98] Z Fei et al. "Edge and surface plasmons in graphene nanoribbons". In: *Nano letters* 15.12 (2015), pp. 8271–8276.

[99] Serguei Brazovskii et al. "Scanning-tunneling microscope imaging of single-electron solitons in a material with incommensurate charge-density waves". In: *Physical review letters* 108.9 (2012), p. 096801.

[100] Hang Xie, Jin-Hua Gao, and Dezhuan Han. "Excited spin density waves in zigzag graphene nanoribbons". In: *New Journal of Physics* 20.1 (2018), p. 013035.

[101] WA Little. "Possibility of synthesizing an organic superconductor". In: *Physical Review* 134.6A (1964), A1416.

[102] William A. Little. "Superconductivity of organic polymers". In: *Journal of Polymer Science Part C: Polymer Symposia* 17.1 (1967), pp. 1–12.

[103] W_P Su, JR Schrieffer, and Ao J Heeger. "Solitons in polyacetylene". In: *Physical review letters* 42.25 (1979), p. 1698.

[104] Jingtian Fang et al. "Theoretical study of ballistic transport in silicon nanowire and graphene nanoribbon field-effect transistors using empirical pseudopotentials". In: *IEEE Transactions on Electron Devices* 64.6 (2017), pp. 2758–2764.

[105] Gage Hills et al. "Modern microprocessor built from complementary carbon nanotube transistors". In: *Nature* 572.7771 (2019), pp. 595–602.

[106] Xiaolong Liu and Mark C Hersam. "2D materials for quantum information science". In: *Nature Reviews Materials* 4.10 (2019), pp. 669–684.

[107] Michael R Wasielewski et al. "Exploiting chemistry and molecular systems for quantum information science". In: *Nature Reviews Chemistry* 4.9 (2020), pp. 490–504.

[108] Kohei Kawabata et al. "Symmetry and topology in non-Hermitian physics". In: *Physical Review X* 9.4 (2019), p. 041015.

[109] Zongping Gong et al. "Topological phases of non-Hermitian systems". In: *Physical Review X* 8.3 (2018), p. 031079.

[110] Xiao Li et al. "Non-Hermitian physics for optical manipulation uncovers inherent instability of large clusters". In: *Nature Communications* 12.1 (2021), p. 6597.

[111] Stefano Longhi, Davide Gatti, and Giuseppe Della Valle. "Non-Hermitian transparency and one-way transport in low-dimensional lattices by an imaginary gauge field". In: *Physical Review B* 92.9 (2015), p. 094204.

[112] Stefano Longhi. "Non-Hermitian bidirectional robust transport". In: *Physical Review B* 95.1 (2017), p. 014201.

[113] Emil J Bergholtz, Jan Carl Budich, and Flore K Kunst. "Exceptional topology of non-Hermitian systems". In: *Reviews of Modern Physics* 93.1 (2021), p. 015005.

[114] Nobuyuki Okuma et al. "Topological origin of non-Hermitian skin effects". In: *Physical review letters* 124.8 (2020), p. 086801.

[115] Naomichi Hatano and David R Nelson. "Localization transitions in non-Hermitian quantum mechanics". In: *Physical review letters* 77.3 (1996), p. 570.

[116] Naomichi Hatano and David R Nelson. "Vortex pinning and non-Hermitian quantum mechanics". In: *Physical Review B* 56.14 (1997), p. 8651.

[117] Fei Song, Shunyu Yao, and Zhong Wang. "Non-Hermitian topological invariants in real space". In: *Physical review letters* 123.24 (2019), p. 246801.

[118] Kazuki Yokomizo and Shuichi Murakami. "Non-Bloch band theory of non-Hermitian systems". In: *Physical review letters* 123.6 (2019), p. 066404.

[119] Nobuyuki Okuma et al. "Topological origin of non-Hermitian skin effects". In: *Physical review letters* 124.8 (2020), p. 086801.

[120] Giovanni Pizzi et al. "Wannier90 as a community code: new features and applications". In: *Journal of Physics: Condensed Matter* 32.16 (2020), p. 165902.

[121] Supriyo Datta. *Electronic Transport in Mesoscopic Systems*. Cambridge: Cambridge University Press, 1995. DOI: 10.1017/CBO9780511805776.

[122] Sumedh P Surwade et al. "Water desalination using nanoporous single-layer graphene". In: *Nature nanotechnology* 10.5 (2015), pp. 459–464.

[123] N. Dontschuk et al. "A graphene field-effect transistor as a molecule-specific probe of DNA nucleobases". In: *Nat. Commun.* 6.1 (2015), p. 6563.

[124] Steven P. Koenig et al. "Selective Molecular Sieving through Porous Graphene". In: *Nature Nanotechnology* 7.11 (2012), pp. 728–732. ISSN: 1748-3387. DOI: 10.1038/nnano.2012.162.

[125] Ryan C. Rollings, Aaron T. Kuan, and Jene A. Golovchenko. "Ion Selectivity of Graphene Nanopores". In: *Nature Communications* 7.1 (2016), p. 11408. ISSN: 2041-1723. DOI: 10.1038/ncomms11408.

[126] C. Moreno et al. "Bottom-up synthesis of multifunctional nanoporous graphene". In: *Science* 360.6385 (2018), pp. 199–203.

[127] M. Shekhirev, P. Zahl, and A. Sinitskii. "Phenyl functionalization of atomically precise graphene nanoribbons for engineering inter-ribbon interactions and graphene nanopores". In: *ACS Nano* 12.8 (2018), pp. 8662–8669.

[128] J. D. Teeter et al. "Dense monolayer films of atomically precise graphene nanoribbons on metallic substrates enabled by direct contact transfer of molecular precursors". In: *Nanoscale* 9.47 (2017), pp. 18835–18844.

[129] Alexander Sinitskii. "A Recipe for Nanoporous Graphene". In: *Science* 360.6385 (2018), pp. 154–155. DOI: 10.1126/science.aat9592.

[130] Marco Di Giovannantonio et al. "On-Surface Synthesis of Antiaromatic and Open-Shell Indeno[2,1-b]Fluorene Polymers and Their Lateral Fusion into Porous Ribbons". In: *Journal of the American Chemical Society* 141.31 (2019), pp. 12346–12354. DOI: 10.1021/jacs.9b04811.

[131] Leo Gross et al. "The chemical structure of a molecule resolved by atomic force microscopy". In: *Science* 325.5944 (2009), pp. 1110–1114.

[132] Ludwig Bartels, Gerhard Meyer, and Karl-Heinz Rieder. "Controlled Vertical Manipulation of Single CO Molecules with the Scanning Tunneling Microscope: A Route to Chemical Contrast". In: *Applied Physics Letters* 71.2 (1997), pp. 213–215.

[133] Rafal Zuzak et al. "Nonacene Generated by On-Surface Dehydrogenation". In: *ACS Nano* 11.9 (2017), pp. 9321–9329.

[134] Hsin-Yen Chen et al. "Diindeno[1,2-g:1',2'-s]rubicene: All-carbon non-fullerene electron acceptor for efficient bulk-heterojunction organic solar cells with high open-circuit voltage". In: *RSC Advances* 5.5 (2015), pp. 3381–3385.

[135] Shudong Wang and Jinlan Wang. "Quasiparticle energies and optical excitations in chevron-type graphene nanoribbon". In: *The Journal of Physical Chemistry C* 116.18 (2012), pp. 10193–10197.

[136] H Sevinçli, M Topsakal, and S Ciraci. "Superlattice Structures of Graphene-Based Armchair Nanoribbons". In: *Physical Review B* 78.24 (2008), p. 245402.

[137] Saeed Zamani and Rouhollah Farghadan. "Graphene nanoribbon spin-photodetector". In: *Physical Review Applied* 10.3 (2018), p. 034059.

[138] D. Jérome, T. M. Rice, and W. Kohn. "Excitonic insulator". In: *Physical Review* 158.2 (1967), pp. 462–475.

[139] W. Kohn. "Excitonic phases". In: *Physical Review Letters* 19.8 (1967), pp. 439–442.

[140] H. Cercellier et al. "Evidence for an excitonic insulator phase in 1T-TiSe2". In: *Physical Review Letters* 99.14 (2007), p. 146403.

[141] Yun Cheng et al. "Light-induced dimension crossover dictated by excitonic correlations". In: *Nature communications* 13.1 (2022), p. 963.

[142] Shantanu Mishra et al. "Synthesis and characterization of π-extended triangulene". In: *Journal of the American Chemical Society* 141.27 (2019), pp. 10621–10625.

[143] Gurjyot Sethi et al. "Flat-band-enabled triplet excitonic insulator in a diatomic kagome lattice". In: *Physical Review Letters* 126.19 (2021), p. 196403.

[144] Franz X Bronold and Holger Fehske. "Possibility of an excitonic insulator at the semiconductor-semimetal transition". In: *Physical Review B* 74.16 (2006), p. 165107.

[145] B Zenker et al. "Electron-hole pair condensation at the semimetal-semiconductor transition: A BCS-BEC crossover scenario". In: *Physical Review B* 85.12 (2012), p. 121102.

[146] Yinong Zhou et al. "Excited quantum anomalous and spin Hall effect: dissociation of flat-bands-enabled excitonic insulator state". In: *Nanotechnology* 33.41 (2022), p. 415001.

[147] BI Halperin and TM Rice. "Possible anomalies at a semimetal-semiconductor transistion". In: *Reviews of Modern Physics* 40.4 (1968), p. 755.

[148] Jie Gu et al. "Dipolar excitonic insulator in a moiré lattice". In: *Nature Physics* 18.4 (2022), pp. 395–400.

[149] K Seki et al. "Excitonic Bose-Einstein condensation in Ta 2 NiSe 5 above room temperature". In: *Physical Review B* 90.15 (2014), p. 155116.

[150] Xiaobo Ma et al. "Ta 2 NiSe 5: A candidate topological excitonic insulator with multiple band inversions". In: *Physical Review B* 105.3 (2022), p. 035138.

[151] YF Lu et al. "Zero-gap semiconductor to excitonic insulator transition in Ta2NiSe5". In: *Nature communications* 8.1 (2017), p. 14408.

[152] W Kohn and D Sherrington. "Two kinds of bosons and Bose condensates". In: *Reviews of Modern Physics* 42.1 (1970), p. 1.

[153] Van-Nham Phan, Klaus W Becker, and Holger Fehske. "Spectral signatures of the BCS-BEC crossover in the excitonic insulator phase of the extended Falicov-Kimball model". In: *Physical Review B* 81.20 (2010), p. 205117.

[154] Huaxiang Fu, Lin-Wang Wang, and Alex Zunger. "Excitonic exchange splitting in bulk semiconductors". In: *Physical Review B* 59.8 (1999), p. 5568.

[155] Andrés Granados Del Águila et al. "Effect of electron-hole overlap and exchange interaction on exciton radiative lifetimes of CdTe/CdSe heteronanocrystals". In: *ACS nano* 10.4 (2016), pp. 4102–4110.

[156] David J Norris et al. "Size dependence of exciton fine structure in CdSe quantum dots". In: *Physical Review B* 53.24 (1996), p. 16347.

[157] Manoj Nirmal et al. "Observation of the" dark exciton" in CdSe quantum dots". In: *Physical review letters* 75.20 (1995), p. 3728.